

Interplay between charging effects and
multi-particle transport in superconducting single
electron transistors with tunable junctions

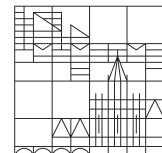
Dissertation zur Erlangung des
akademischen Grades eines Doktors der
Naturwissenschaften (Dr.rer.nat.)

vorgelegt von

Susanne Sprenger

an der

Universität
Konstanz



Mathematisch-Naturwissenschaftliche Sektion
Fachbereich Physik

Konstanz, 2019

Kurzzusammenfassung

In dieser Doktorarbeit werden Einzelektronentransistoren (SETs) in unterschiedlichen Kopplungsbereichen untersucht. Ein SET besteht aus einer metallischen Insel mit schwacher Kopplung an die Zuleitungen. Eine weitere sog. Gate-Elektrode ist kapazitiv an die Insel gekoppelt. Ist die Gesamtkapazität der Insel klein genug, können Ladungseffekte beobachtet werden. Diese führen zu einer Unterdrückung des Stromflusses bei niedrigen Transportspannungen, die sog. Coulomb-Blockade. Bleibt die Kopplung der Insel an die Zuleitungen schwach, so hat diese wohldefinierte Ladungszustände. Der Transport durch den SET wird in diesem Fall durch die Orthodoxe Theorie beschrieben.

In dieser Arbeit bestehen die SETs aus Aluminium. Einer der Kontakte zu den Zuleitungen wurde durch einen mechanisch kontrollierbaren Bruchkontakt ersetzt. Durch diesen kann die Kopplung der Insel an die entsprechende Zuleitung *in situ* verändert werden. Dies erlaubt den Einfluss der Änderung der Kopplung auf die Coulomb-Blockade zu beobachten. Zusätzlich bietet Aluminium die Möglichkeit das Zusammenspiel von Supraleitung und Coulomb-Blockade zu untersuchen.

Für den Fall schwacher Kopplungen wird der supraleitende Ladungstransport durch Cooperpaare und Quasiteilchen getragen. Die unterschiedlichen Kopplungen der beiden Kontakte ermöglichen die Beobachtung von Nicht-Gleichgewichtsphänomenen. Diese werden durch eine Erweiterung der Orthodoxen Theorie beschrieben.

Bildet der Bruchkontakt einen mesoskopischen Kontakt, können Andreev-Reflexionen und multiple Andreev-Reflexionen am Transport teilnehmen. Diese können mehrere Ladungen gleichzeitig transportieren. Das vorgestellte Design der Proben ermöglicht erstmals den Nachweis von multiplen Andreev-Reflexionen in SETs.

Im vorgestellten Probendesign können starke Kopplungen durch atomare Kontakte des Bruchkontakte realisiert werden. Für diesen Fall wird eine neue Methode für die Anpassung des Transportdiagramms vorgestellt. Dadurch wird die Bestimmung der Ladungsenergie im normal- und supraleitenden Zustand ermöglicht. In beiden Fällen wird eine Renormalisierung der Ladungsenergie für steigende Kopplung beobachtet. Für atomare Kontakte weicht die supraleitende Ladungsenergie von der normalleitenden ab.

Contents

Table of Contents	1
1 Introduction	3
2 Theoretical Background	5
2.1 Quantum Transport of Charges	5
2.2 Superconductivity	8
2.2.1 The Josephson Junction	8
2.2.2 Andreev Reflection	10
2.2.3 Multiple Andreev Reflection as Indication of Mesoscopic Superconductivity	11
2.3 The Single Electron Transistor in the Framework of Orthodox Theory	12
2.3.1 The Free Energy of the SET	13
2.3.2 The Stability Diagram	16
3 Experimental Techniques	19
3.1 Sample Preparation	19
3.1.1 General Process	19
3.1.2 The Tunnel Contact	21
3.1.3 Sample Geometry	23
3.2 The Mechanical Setup	24
3.2.1 The Cooling System	25
3.2.2 Breaking Mechanics	25
3.3 Electrical Setup	26
Reduction of External Noise Sources	27
3.3.1 Wiring and Filters	28
3.3.2 Measurement Electronics	29
3.4 Data Acquisition and Processing	30
3.4.1 Settings of the Data Acquisition	30
3.4.2 Measurement Procedure and Data Storage	31
Resistances in the SET	31
3.5 Digital Data Processing	32
3.5.1 Conversion from Time Traces to IV Characteristics	32
3.5.2 Digital Filtering and Derivation	32
4 The Superconducting Single Electron Transistor	35
4.1 State of Research	35

4.2	The SSET at Finite Bias	37
4.2.1	The Voltage Divider	37
4.2.2	Transport Diagram of the SSET	38
4.2.3	Superconducting Current Cycles	40
	The Quasiparticle Onset (e - e Onset)	41
	The JQP Cycle	41
	The 3e Cycle	42
	The AQP Cycle	42
	The 3e-A Cycle	42
	Further Andreev Cycles	43
	The MARQP Cycle	43
4.2.4	Simulations Based on Orthodox Theory	43
	The Quasiparticle Rate	44
	The Cooper Pair Rate	45
	The Andreev Reflection Rates	45
5	Experimental Results	47
5.1	Characterization of SETs in the Normal Conducting State	47
5.1.1	Calculating the Resistance of the NC SET	47
5.1.2	Determination of the Charging Energy	49
5.1.3	Renormalization of the Charging Energy	51
5.2	The SSET in the Framework of the Orthodox Theory	53
5.2.1	The JQP Cycle	54
5.2.2	Bias Anomalies of the JQP Cycle	57
	Comparison of Simulated and Experimental Data	58
	Including Non-equilibrium Effects into the Orthodox Theory	61
5.3	Mesoscopic Superconductivity in the SSET	63
5.3.1	Analysis of the Normal Conducting State	64
5.3.2	Characterization of the Superconducting State	65
5.3.3	Bias Asymmetries in the Mesoscopic SSET	70
5.4	The SSET beyond Orthodox Theory	71
5.4.1	Simulation of the Mesoscopic SSET	71
5.4.2	The SSET in the Strong Coupling Regime	73
5.4.3	Renormalization of the Charging Energy in the Superconducting State	78
6	Conclusion	81
Bibliography		85
Appendix		93

Chapter 1

Introduction

In 1985 Averin and Likharev proposed a new device being sensible to single electrons, the so called single electron transistor (SET) [Lik87]. The idea was to create a small island of low capacitance that is weakly coupled to two electrodes. In this case, a characteristic charging energy would be required to charge the island by one additional charge, since electric charges are subject to the Coulomb repulsion. Thus, for low energies the transport through the island would be blocked by the so called Coulomb blockade. By attaching a third capacitively coupled electrode to the device one would be able to modulate the Coulomb blockade using this gate electrode.

The first experimental realization of such a device was reported by Fulton and Dolan in 1987 [FD87]. Since those first experiments, SETs have been studied extensively. They have proven to be very sensitive electrometers [Sch+98b] and are discussed for quantum metrology [Pek+08]. The first tries to realize quantum bits were based on the concept of the SET [CW08].

Besides the application-oriented use of SETs, basic physical concepts have been studied both experimentally and theoretically. One focus is the influence of quantum fluctuations onto the Coulomb blockade for strong coupling [Cho+99; Joy+97; Wal02; Wal+02]. Realizations of SETs in two dimensional electron gases have shown, that the Coulomb blockade is sensitive to the microscopic properties of the junctions [Jez+16].

Another focus is the interplay of superconductivity and Coulomb blockade. In the superconducting state, electrons pair up to decrease their energy and thereby create Cooper pairs. Thus, unpaired single electrons have higher energies than paired ones. On the other hand, the Coulomb blockade is sensitive to the number of charges transported and thus prefers single charges in terms of energy. Naturally, the two effects are competing. This competition shows up in the even-odd asymmetry of superconducting SETs for zero bias voltage. The energy of the island's ground state is lower if it has an even number of electrons, whereas charge states having odd numbers are increased in energy [Joy95]. Measuring transport at finite bias voltages, the interplay of the two effects lead to new transport phenomena [Ful+89; Had+98; FPT98].

Up to now, all experimental realizations of superconducting single electron transistors are based on using oxide junctions as tunnel barriers. Using this approach the influence of the coupling to the Coulomb blockade can only be studied by comparing different samples with each other.

In this thesis we present a new design of a superconducting SET made of aluminum. One of the oxide tunnel barriers is replaced by a mechanically controlled break junction. Thus, the

coupling can be tuned *in situ*. Using aluminum as metal allows to measure in the normal conducting as well as in the superconducting state. The break junction also allows to investigate the influence of mesoscopic transport where only a few conductance channels contribute to the transport.

This new SET design allows to study a variety of new effects. In the normal conducting state, the charging energy is renormalized for strong coupling through the break junction.

The measurement in the superconducting state enables to analyze the different couplings in more detail. For low coupling and asymmetric junction resistances signatures of non-equilibrium effects arise.

If the coupling is increased and allows for mesoscopic transport, multiple Andreev reflections will contribute. Andreev reflections transport several charges at once creating new transport processes through the SET. The contribution can be tuned using the break junction. Thus, the introduced sample design is the first experimental realization allowing for multiple Andreev reflections in SETs.

For atomic contacts and thus strong coupling the Coulomb blockade is altered. In this thesis a new data evaluation is introduced which allows to calculate the charging energy in the superconducting state. For the strong coupling the charging energies in the normal and superconducting state differ. This indicates that the easy concept of capacitances defining the behavior of the SET is not sufficient anymore for strong coupling.

This thesis is organized as follows:

In Chapter 2 we present the basic principles of superconductivity and single electron transistors. The Orthodox theory describing the transport through a SET is presented. We will also put this work into context with previous research.

Measurements of single electron transport are experimentally challenging. Thus we introduce the sample preparation and the measurement setup in Chapter 3. Special focus will be laid on the measurement concept and on the data processing.

In Chapter 4 the Orthodox theory is expanded to describe the transport through a superconducting SET. We also introduce the extension covering mesoscopic transport.

After introducing the physics and the data evaluation we present the experimental results in Chapter 5. We first characterize the samples in the normal conducting state. The measurements in the superconducting state yield several new findings.

We conclude by giving a summary.

Chapter 2

Theoretical Background

2.1 Quantum Transport of Charges

In macroscopic conductors like metals electrical transport is described by Ohm's law. The conductance G is given by the material specific conductivity σ and the geometry of the contact, defined by the area A and its length L

$$G = \sigma \frac{A}{L}. \quad (2.1)$$

When measuring transport through mesoscopic conductors, one observes a variety of different phenomena not present in macroscopic conductors. But before studying them, one should define the term "mesoscopic".

To enter the mesoscopic regime we decrease the size of the sample L . It must be smaller than the phase coherence length l_ϕ . This quantity l_ϕ defines the length scale over which the phase information gets lost, predominately, by inelastic scattering. For $L < l_\phi$ the transport can be treated as an easy elastic scattering problem.

We now go over from extended conductors to small contacts. Thus the characteristic geometrical length is the contact width W instead of the conductor's length L . We assume the contact width W to be smaller than the Fermi wavelength λ_F . Thereby we enter the full quantum limit, requiring a description covering the quantum mechanical properties. A very well established description was given by Landauer in the late 1950's [Lan57] and will shortly be elaborated in the following. For more detailed presentations one may also refer to [AYvR03; Sch10b].

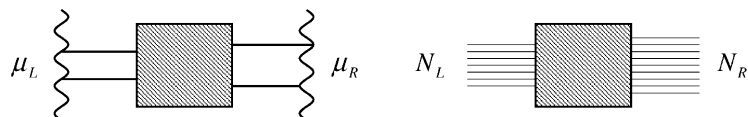


Figure 2.1: Schematic of the Landauer approach. A scattering region (gray) is connected to two electron reservoirs on the right and on the left side via several perfectly transmitting modes. The number of modes N_L and N_R connecting the scattering region to the left (right) reservoir must not necessarily be equal. The reservoirs have the chemical potential μ_R and μ_L , respectively, and inject electrons to the sample. Incoming electrons reflected at the scattering region are perfectly absorbed by the reservoirs. Taken from [AYvR03].

The main conclusion of the Landauer approach is summarized by "conductance is transmission".

The mesoscopic contact is modeled as a scattering region (gray box in Fig. 2.1), where only elastic scattering takes place. This region is connected to two macroscopic electron reservoirs on left and on the right via several perfect leads (illustrated by horizontal lines).

By setting up the Hamiltonian and solving the Schrödinger's equation for this model one can identify the current-carrying modes. Each lead connecting the scattering region to the reservoir contributes with one mode because of the small dimensions of the contact ($W \leq \lambda_F$). The electrons transported using the modes can only scatter inside the contact. This idea allows to describe the mesoscopic contact by a scattering matrix, assigning an individual transmission to each current-carrying mode. The modes having a finite transmission are called Eigenchannels or conductance channels. All modes of zero transmission are not contributing to the transport.

Summing over all contributing channels n and their individual transmission coefficients τ_n we derive the conductance of an atomic contact, the so called Landau formula:

$$G = \frac{2e^2}{h} \sum_{n=1}^N \tau_n. \quad (2.2)$$

Please note that each mode can add at maximum one conductance quantum $G_0 = 2e^2/h$ if the transmission is equal to one. This also yields an unintuitive result: For a mesoscopic contact consisting of one fully transmitting channel, the resistance does not vanish but instead is still $1/G_0 = h/2e^2 \approx 12.9\text{ k}\Omega$.

A representative example for the implications of this description is given by a point contact defined in a two-dimensional electron gas (2DEG), which also shows mesoscopic transport. This point contact can be realized by applying a voltage to a split-gate structure. The voltage defines the width of the point contact.

When measuring the conductance while varying the voltage at the split gates, we observe a

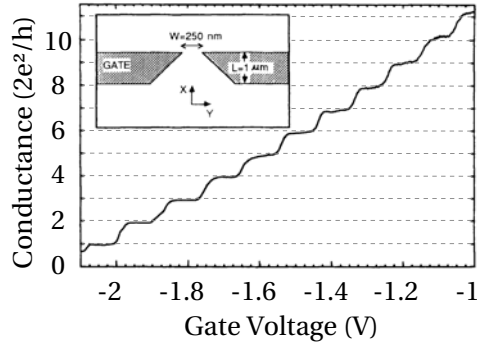


Figure 2.2: Conductance quantization in a quantum point contact. The quantum point contact is defined in a two-dimensional electron gas using electrostatic gate electrodes. When increasing the gate voltage the conductance changes stepwise. Each step has a height of the conductance quantum G_0 and is explained as the appearance of an additional perfectly transmitting mode. Taken from [vWee+88].

stepwise change in the conductance. As can be seen in Fig. 2.2, every step has a step height of one G_0 . Each step represents an additional conductance channel entering the point contact and contributing to the conductance. The channel may enter as soon the contact width is

broad enough. Each conductance channel has a transmission of 1 since it is perfectly coupled to the 2DEG. Thus no scattering takes place when passing through the contact. This step like increase of the conductance in steps of G_0 is called conductance quantization.

Now we want to introduce the properties of the afore mentioned atomic point contacts in metals. They can be obtained by mechanical stretching of a thin metallic contact. The mechanical stretching can for example be realized using a scanning tunneling microscope [ARV93; Ole+94; Pas+93a] or by a mechanically controllable break junction [Kra+95; MvRdJ92] as it will be done in this thesis.

If we measure the conductance continuously while stretching the contact, we obtain a so-

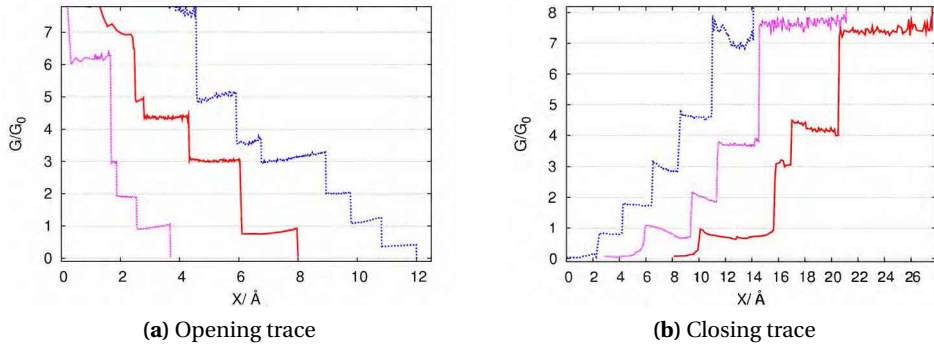


Figure 2.3: Opening and closing traces of an aluminum break junction at $T = 200\text{ mK}$. The conductance is displayed with respect to the displacement of the two electrodes. Conductance plateaus are clearly visible in the opening as well as in the closing traces. They show the tilt typically observed for aluminum. Each plateau represents a new atomic configuration. Taken from [Sch10a].

called opening trace. In a similar way we call the conductance measurement while closing the contact a closing trace. As displayed in Fig. 2.3 both traces show step like changes in conductance with distinct plateaus. At some point the conductance drops completely because the contact is fully broken (for an opening trace).

Since every opening and closing trace looks different we need a statistical evaluation of the conductance plateaus. This is done by displaying the conductance values of several traces in a histogram. Figure 2.4 shows such a histogram for aluminum. We observe distinct peaks at non-integer values of G_0 . Each peak represents a preferred atomic configuration of the break junction. The peak at roughly $0.8G_0$ corresponds to a one atom contact. Similarly, the other peaks at higher conductance values are assigned to two, three or four atom contacts.

For superconducting materials like aluminum not only the statistical analysis is of interest. Here, it is possible to experimentally determine the number of conductance channels (see Section 2.2.3) and their individual transmission [Sch+97]. It turns out that in a one atom contact of aluminum more than one channel contributes to the current even though the conductance is smaller than one G_0 . Aluminum is a sp-metal with three valence atoms and tends to form three conductance channels of intermediate transmission for a one atom contact [AYvR03; Sch+98a].

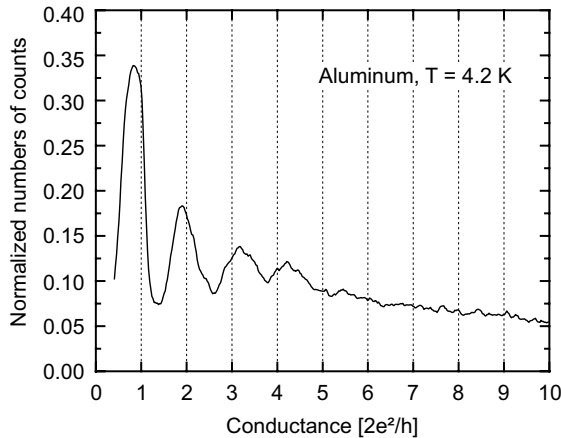


Figure 2.4: Histogram of the measured conductances of an aluminum break junction. The histogram is composed of 30000 opening traces measured at $T = 4.2\text{ K}$. The preferred conductance values accumulate in the typical peaks for aluminum at $0.8 G_0$, $1.9 G_0$, $3.1 G_0$ and $4.3 G_0$. Taken from [Yan+08].

2.2 Superconductivity

In 1911 Kamerlingh Onnes measured the resistance of mercury while cooling down to very low temperatures. He observed the resistance dropping to zero for temperatures below 4.2 K [Kam11a; Kam11b; Kam11c]. This was the discovery of superconductivity.

In 1950 Ginzburg and Landau offered a phenomenological theory describing some of the observations [LH65]. Only seven years later in 1957 Bardeen, Cooper and Schrieffer published a microscopic theory of superconductivity [BCS57]. This theory states the possibility of a new ground state of the electronic system, if there is a small attractive interaction between electrons around the Fermi level. This ground state, the superconductivity, is decreased in energy in comparison to the Fermi energy by the superconducting gap Δ . The ground state is created by the pairing of electrons to so called Cooper pairs, which follow Bose statistics. Thus, the electronic system is described by one macroscopic wave function.

It is not the aim of this work to give a full introduction to superconductivity. We will mainly focus on some properties of the superconducting transport. For a broader overview the reader may be referred to the respective textbooks such as [Tin04].

2.2.1 The Josephson Junction

A connection of two superconducting electrodes with the same superconducting gap via a weak link is called a Josephson junction. The weak link can for example be created by a thin insulating barrier or by a small distance between the two electrodes. The latter can be realized using a break junction technique. If we connect a current source to those weakly coupled superconducting electrodes, it is possible to drive a current through the weak link without a voltage difference between the electrodes. This current is called the supercurrent I_S and can be interpreted as the tunneling of Cooper pairs. The first Josephson equation relates the

supercurrent with the phase difference ϕ between the wave functions of the two electrodes and the critical current I_c :

$$I_S = I_c \sin(\phi), \quad (2.3)$$

with the critical current I_c describing the maximum current that can be carried by the superconductor. This supercurrent is a DC current. The phase difference between the electrodes can be altered as described by the second Josephson equation

$$\frac{d\Phi}{dt} = \frac{2eV}{\hbar} \quad (2.4)$$

by applying a voltage V to the Josephson contact. The second Josephson equation gives rise to an AC current of amplitude I_c and frequency $\omega_J = \frac{2eV}{\hbar}$.

Using the Josephson equations we can calculate the potential energy stored in the junction when driving a current through it. This energy is proportional to the Josephson energy

$$E_J = \frac{\hbar I_c}{2e} \quad (2.5)$$

which describes the coupling of the superconductors through the contact.

The exact value of the critical current is hereby dependent on the microscopic properties of the junction and the geometry [Tin04], as well as on the circuit used to measure it. For insulating tunnel barriers without inelastic scattering the critical current I_c and the normal state resistance R_N are connected. Ambegaokar and Baratoff derived an expression describing the temperature dependence of the $I_c R_N$ product [AB63]

$$I_c R_N = \frac{\pi \Delta}{2e} \tanh\left(\frac{\Delta}{2k_B T}\right). \quad (2.6)$$

The DC supercurrent at zero voltage is not the only possibility to drive current through a Josephson junction. Also unpaired electrons (quasiparticles) can contribute to the electrical transport, if they are excited. The excitation of the quasiparticles can either be done electrical or thermal. Thermally activated quasiparticles create a small current signal inside the superconducting gap. For electrical excitation of quasiparticles a bias voltage of $eV \geq 2\Delta$ is required to break a cooper pair.

Figure 2.5 shows current-voltage-characteristics (IV traces) for a typical Josephson junction. A clear supercurrent at zero bias voltage is observable. If the current exceeds the critial current (at I_S) a voltage of $eV = 2\Delta$ drops at the junction. We observe a jump to the normal conducting branch. For $eV \geq 2\Delta$ the current is carried by electrically excited quasiparticles. The except shape of the IV traces depends on the resistance, the capacitance and the coupling of the Josephson junction and the circuit it is embedded in. The RCSJ (Resistively and Capacitively Shunted Junction) model [McC68; Ste68] offers an accurate description.

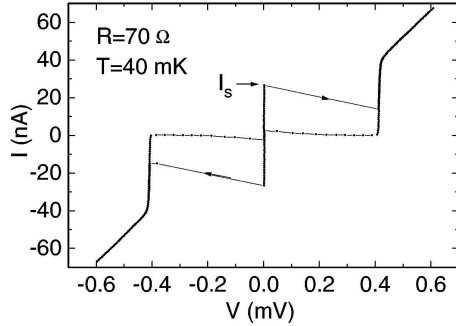


Figure 2.5: Current-voltage-characteristics of a Josephson junction. At $V = 0$ V a distinct supercurrent is measured until the signal jumps to the normal conducting branch where a voltage drops at the junction. For voltages $V \geq 2\Delta \approx 0.4$ mV the current is carried by quasiparticles. Taken from [Vio+96].

2.2.2 Andreev Reflection

As discussed in the previous section, for a well-defined tunnel barrier or Josephson contact the only current contributions are the supercurrent at zero bias and quasiparticle tunneling at $eV \geq 2\Delta$. However, for mesoscopic superconducting contacts like single-atom contacts or very transparent tunnel barriers, Andreev reflection is possible for bias voltages of $eV \geq \Delta$ by converting two quasiparticles into a Cooper pair. An easy ostensive model of the transport process uses the semiconductor representation of superconductivity and is presented in the following. We limit the description here to the properties needed later on. All other related phenomena and descriptions can be found in literature [KBT82; Tin04].

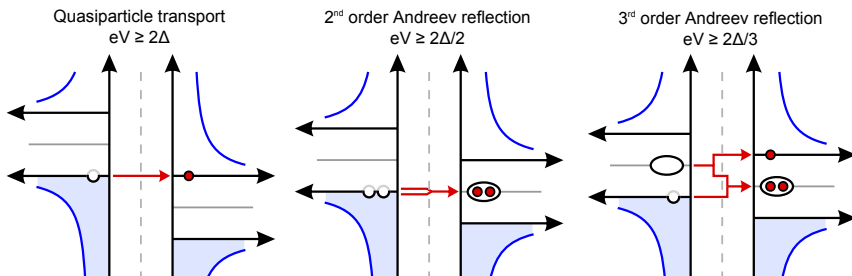


Figure 2.6: Schematic of Andreev reflection in the semiconductor representation. For voltages $\Delta < eV < 2\Delta$ Andreev reflections carry the current. An incident electronic quasiparticle gets back-reflected as a hole while a Cooper pair is formed in the right superconductor. For lower voltages multiple Andreev reflections take place exemplified for the case of the 3rd Andreev reflection. Those higher order processes involve creating and breaking Cooper pairs on both sides of the junction. Based on [Sch09]

We assume a mesoscopic S-I-S contact of two superconductors of the same gap with an applied voltage of $2\Delta > eV \geq \Delta$ (see Fig. 2.6). If a quasiparticle travels from the left superconductor (S_L) to the right superconductor (S_R) it cannot enter a free quasiparticle state. Therefore, it is back reflected into S_L as a hole, where the hole can enter a free hole state. The back reflected hole and the transmitted quasiparticle pair up to form a Cooper pair in S_R and in total two charges are transferred.

Loosely speaking an Andreev reflection transports two quasiparticles at the same time. To-

gether they gain an energy of 2Δ by tunneling. The two quasiparticles pair up to a Cooper pair in S_R .

2.2.3 Multiple Andreev Reflection as Indication of Mesoscopic Superconductivity

Multiple Andreev reflections are an iterative continuation of Andreev reflection that allow for current transport at low bias voltages $eV \leq \Delta$. The mechanism is very similar to Andreev reflection but involves the reflection of several quasiparticles. We exemplify the process by 3rd order Andreev reflection happening at voltages of $eV \geq \frac{2\Delta}{3}$.

Again a quasiparticle from S_L travels to S_R and gains the energy $eV \geq \frac{2\Delta}{3}$ (see Fig. 2.6). Since no free state is available it is back reflected as a hole. But at this low energy there is no free hole state in S_R , causing the hole to be again back reflected as a quasiparticle. This quasiparticle can then enter the free quasiparticle states in S_R .

We can summarize, that for a 3rd order Andreev reflection three quasiparticles are transported together. Each particle gains the energy $eV \geq \frac{2\Delta}{3}$, so the energy of the whole process is $eV \geq 2\Delta$ and can form a Cooper pair and an excited quasiparticle in S_R .

The higher order Andreev reflections are iterations of this process. The n^{th} order can hereby enter the transport at bias voltages of $eV \geq \frac{2\Delta}{n}$ and transports n charges. In this nomenclature, the “usual” Andreev reflection discussed in the previous chapter represents the 2nd order.

Although higher order multiple Andreev reflections transport more charges, the absolute current carried by them is in general smaller than for the lower orders. The probability P for a multiple Andreev reflection to occur is roughly proportional to the transmission of the conductance channel τ and the power of the order n , $P \approx \tau^n$. Therefore, the contributions of the higher orders are strongly decreased (unless $\tau \approx 1$).

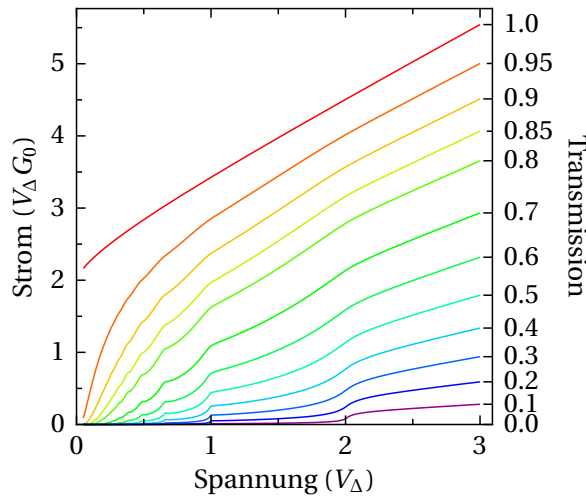


Figure 2.7: Normalized IV traces of multiple Andreev reflection for various transmissions τ_i . The threshold of an additional order at voltages $V = \frac{2\Delta}{n}$ is marked by a discontinuity of the curvature of the IV traces. Taken from [Sch09] using [Sch09].

Nonetheless, multiple Andreev reflection is a clear signature of mesoscopic superconductivity. Figure 2.7 shows the IV characteristics calculated for a single conductance channel for varying transmission [CB03]. In all traces, the contributions of the different orders of multiple Andreev reflections can be identified by a discontinuous change of the slope of the IV curve. Each of this changes is located at $eV = \frac{2\Delta}{n}$.

In addition, it is clearly visible that the contribution of the different orders of MARs with respect to the channel transmission is strongly non-linear. This opens the possibility to use the curvature of the IVs to identify the number of contributing channels and their transmission τ_i , as it has been done in [Sch+97]. Figure 2.8 shows an opening trace of an aluminum break junction. The contributing channels and their transmission for each contact configuration are added. Even if the overall transmission changes only slightly a clear change of the channels is observable.

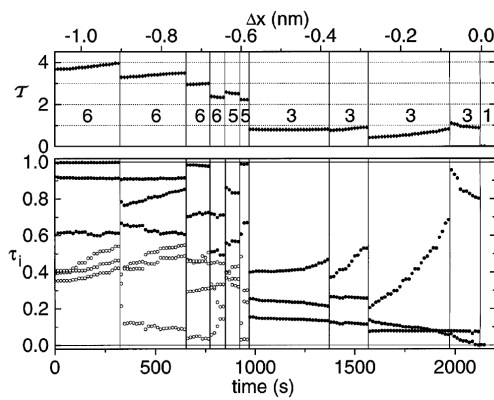


Figure 2.8: Opening trace of an aluminum break junction and calculation of the transmission of the contributing conductance channels. The upper panel shows the opening trace. The conductance is represented by the overall transmission $T = \sum \tau_i$ in G_0 . The lower panel displays the individual transmission τ_i of the contributing conductance channels. For single atom contacts ($T \approx 1$) mainly three conductance channels contribute to the conductance. Taken from [Sch09].

2.3 The Single Electron Transistor in the Framework of Orthodox Theory

Small tunnel contacts can be characterized by their resistance R and their capacitance C . If one electron tunnels through a contact it charges the capacitance. Thus, a charging energy $E_C = \frac{e^2}{2C}$ is required. If the energy available for tunneling is lower than the charging energy the transport is suppressed. This phenomenon is known as Coulomb blockade (CB).

If we now set two small tunnel contacts very close to each other in series, they incorporate a small piece of metal. We will name this piece of metal an island.

Capacitively coupled to a gate electrode, this island forms a single electron transistor (SET). Again, the main energy defining the SET is the charging energy E_C required to charge the

island by one additional charge

$$E_C = \frac{e^2}{2C_\Sigma} \quad (2.7)$$

with C_Σ being the capacitance of the island with respect to the whole surrounding. The gate electrode can be used to modulate the Coulomb blockade and therefore “switch” between conductive and non-conductive state as known from classical transistors.

To describe the Coulomb blockade within the Orthodox theory the charge levels of the island need to be well defined. This leads to the demand for low temperatures. The thermal fluctuations must be smaller than the charging energy, $k_B T \leq E_C$. Commercially available dilution refrigerators offer temperatures down to 25 mK or even lower, which allows to observe charging energies in the range of 5 μ eV.

Furthermore, the capacitance of the island must be small to achieve reasonable high charging energies.

The third condition regards the coupling of the island to its leads. The tunneled electron must be well localized on the island to be covered by the Orthodox theory. Using the energy-time uncertainty relation and assuming a tunneling time of $\delta t = RC_\Sigma$ we derive the condition [FD87]

$$R \geq \frac{\hbar}{e^2}. \quad (2.8)$$

This is always fulfilled if R exceeds the quantum resistance R_K ,

$$R \geq R_K = \frac{\hbar}{e^2} \approx 25.8 \text{ k}\Omega \quad (2.9)$$

as it has been presented in later publications [GD92; Sch98].

All these conditions define the parameter space in which it is possible to describe the Coulomb blockade using the Orthodox theory. After defining the preconditions of the Orthodox theory in this section we discuss the requirements to observe a current flowing through the SET in terms of the SET’s free energy. The Orthodox theory describes the current as sequential tunneling of charges through the two junctions.

We want to point out, that the following sections describing the SET present the Orthodox theory and its consequences. Every time we discuss any result in terms of the Orthodox theory, we refer to the preconditions defined in this section and the descriptions given in the following sections. The model of the Orthodox theory may also be used to simulate the current flowing through a SET (see Section 4.2.4).

2.3.1 The Free Energy of the SET

For a closer look onto the behavior of the SET we need to calculate the system’s free energy. Figure 2.9 shows an equivalent circuit diagram. It basically represents a capacitive voltage divider. We will stick to the voltages and capacitances defined there. In the following we will

only present a short summary of the derivation of the system's free energy. For a more detailed elaboration please refer to [Her95; FD87; Gra+91].

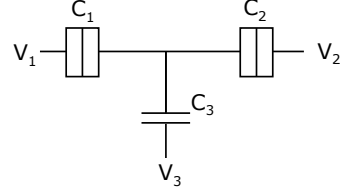


Figure 2.9: Equivalent circuit diagram of a SET. An island is enclosed between two contacts of capacitance C_1 and C_2 . The voltages V_1 and V_2 are applied to the tunnel contacts. A third voltage V_3 is coupled to the island via the capacitance C_3 .

Because of the quantized nature of electrons the total number of electrons on the island is always discrete. We define the number of charges in thermal and electrostatic equilibrium as the $n = 0$ state, with n being the number of excess charges on the island.

Using the definitions in Fig. 2.9 we calculate the electrostatic potential of the island ϕ to be

$$\phi = \frac{1}{C_{\Sigma}} \left(\sum_{i=1}^3 C_i V_i - e n \right), \quad (2.10)$$

with the total capacitance of the island $C_{\Sigma} = \sum C_i$. By summing over the electrostatic energies of all three capacitances we derive the electrostatic energy U_{el} of the system

$$U_{el} = \frac{1}{2} \sum_{i=1}^3 C_i (V_i - \phi)^2 \propto \frac{(-en)^2}{2C_{\Sigma}}. \quad (2.11)$$

Since we are only interested in changes of the electrostatic energy due to changes in the charge states of the island we will from now on only consider the last term and ignore the constant terms of the electrostatic energy.

To calculate the free energy we need to take into account the electrostatic energy and the work done by the voltage sources when an electron tunnels. For an electron tunneling through junction j the work is given by

$$W_j = e \sum_{i=1}^3 (V_i - V_j) \frac{C_i}{C_{\Sigma}}. \quad (2.12)$$

The easiest case is to assume a symmetric voltage bias, meaning $V_1 = V_B/2$, $V_2 = -V_B/2$, $V_3 = V_G$. Using these definitions equation 2.12 gives

$$W_1 = \frac{e}{C_{\Sigma}} \left(C_G V_G - \left(C_2 + \frac{C_G}{2} \right) V_B \right) \quad W_2 = \frac{e}{C_{\Sigma}} \left(C_G V_G - \left(C_1 + \frac{C_G}{2} \right) V_B \right). \quad (2.13)$$

We suppose that n_1 (n_2) electrons have tunneled through contact 1 (2). Therefore n is related to n_1 and n_2 via $n = n_1 - n_2$.

The systems free energy is given by

$$\begin{aligned} F(n, n_1, n_2) &= U_{el}(n) + n_1 W_1 - n_2 W_2 \\ &\propto \frac{(Q - en)^2}{2C_{\Sigma}} - \left[n_1 + n_2 + n \frac{C_1 - C_2}{C_{\Sigma}} \right] \frac{eV_B}{2}. \end{aligned} \quad (2.14)$$

Again we ignore all constants independent from n, n_1 and n_2 .

The term not depending on the bias voltage is the charging energy $E_Q(n)$ of the island including the gate induced charge $Q = C_G V_G$. The gate induced charge can be continuously varied by the gate potential. This also continuously changes the effective charge of the island. Furthermore, the expression shows that as soon as the induced gate charge Q is an integer multiple of e , this is equivalent to a new charge state n' of the island. Thus, the behavior of the SET is e periodic in Q and we can limit all further discussions to $-\frac{e}{2} \leq Q \leq \frac{e}{2}$.

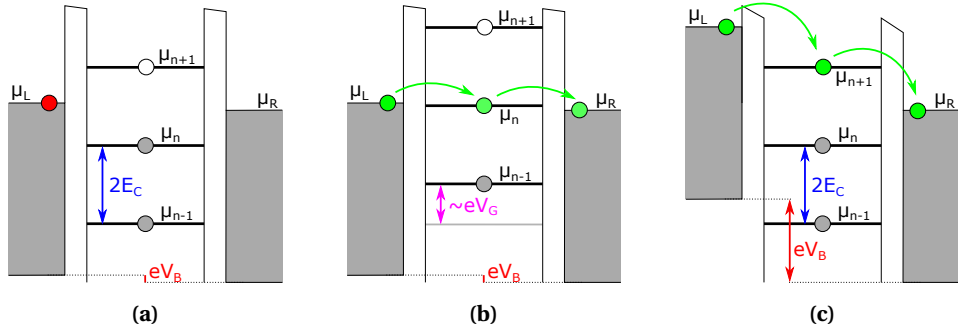


Figure 2.10: Band diagram of the chemical potential of a SET for various bias and gate voltages. The chemical potential of the island depends on the number of electrons n . The charge states of the island have a spacing of $\Delta\mu = 2E_C$.

(a) For small bias voltages V_B the chemical potential of the electrodes, μ_L and μ_R , is in between the empty and the filled states of the island. The current through the SET is suppressed by Coulomb blockade since no elastic tunneling is possible. (b) The gate voltage V_G moves the chemical potential of the island. If one charge state is in resonance with the leads, elastic tunneling is possible for small bias voltages V_B . The current is transported by sequential tunneling from the left electrode to the island and then further to the right electrode. (c) High bias voltages V_B allow to overcome the Coulomb blockade. For voltages $eV_B > 2E_C$ the chemical potential of a charge state of the island μ_{n+1} is always in between the chemical potentials of the electrodes. Sequential charging and discharging of the island by elastic tunneling enables the current through the SET.

Taken from [Lor18].

For $T = 0$ K tunneling is only allowed if it decreases the free energy, i.e. $\delta F < 0$. This defines a parameter space where no transport is allowed, the Coulomb blockade (see Fig. 2.10a). In this region the number of charges on the island is stable. In a graphical representation, the condition $\delta F = 0$ defines a family of lines that surround diamond shaped areas along the V_G axis, the so called Coulomb diamonds. Because of the fixed number of electrons, the conductance is suppressed inside these diamonds. At the crossings of the diamonds on the V_G axis the levels of the island are aligned to the chemical potential of the leads (c.f. Fig. 2.10b) and transport is possible. Thus, the conductance is enhanced. Sweeping the gate voltage for zero bias and measuring the conductance we thereby observe the so-called Coulomb oscillations.

If we leave the $n = 0$ diamond by setting $V_B \neq 0$, it is allowed to change the island charge to $n = \pm 1$ through one of the tunnel contacts. The exact value of V_B depends on the gate induced charge Q . This $n = \pm 1$ state is not stable because tunneling through the other contact is also allowed. Therefore the island returns to the $n = 0$ state and the cycle can start again (please also see Fig. 2.10c).

2.3.2 The Stability Diagram

It is also possible to use an equivalent description by considering tunnel processes through only one junction without regarding the tunnel events through the other one. After calculating the conditions for both contacts independently we will employ the system's free energy to compose the allowed current cycles. This approach is especially helpful when treating superconducting SETs as has been presented by [LSS18; Lor18; Poh99]. We will follow the arguments presented in literature.

First of all we need to find the energy conservation for each tunnel contact. The energy available for tunneling must cover the change in the charging energy of the system, namely

$$\kappa_i e V_B = E_Q(\text{final}) - E_Q(\text{initial}) \quad (2.15)$$

with $\kappa_i e V$ representing the portion of the total bias energy available across junction i . κ_i is given by the voltage divider defined by the capacitances of the SET. We will discuss in chapter Section 4.2.1 how this is calculated for the SET sample presented in this theses.

Assuming tunneling of m electrons charging the island from $n \rightarrow n + m$ Eq. (2.15) reads as

$$\begin{aligned} \kappa_i e V_B &= E_Q(n + m) - E_Q(n) \\ &= \frac{1}{2C_\Sigma} [(Q - e(n + m))^2 - (Q - en)^2] \\ &= 2mE_C \left[-\frac{Q}{2} + n + \frac{m}{2} \right]. \end{aligned} \quad (2.16)$$

Equation (2.16) is a representation of the aforementioned lines surrounding the Coulomb diamonds. Lines of the same slope represent transport over the same contact. All lines can be labeled with the initial and the final charge state (e.g. $0 \rightarrow 1$) as it is depicted in Fig. 2.11.

We take the $n = 0$ diamond as an example. Inside the diamond the $n = 0$ state is stable. It is framed by the lines depicting the condition to change the charge state. Hence, they are labeled with $0 \rightarrow \pm 1$. Please note that by changing the polarity of the bias voltage we also change the direction of the current. Therefore, for one bias polarity we charge the island via contact i whereas for the other polarity the island is discharged over the same contact. Hence, the label changes from $n \rightarrow n \pm 1$ to $n \pm 1 \rightarrow n$ by changing the bias polarity.

To measure a current through the SET using the $n = 0$ state we need to design a closed cycle of charge states, e.g. $0 \rightarrow 1 \rightarrow 0$. We can calculate the minimal required bias energy by calculating the conditions for the two tunnel processes and adding them up. For contact 1 we derive

$$\begin{aligned} \kappa_1 e V_B &= E_Q(n + 1) - E_Q(n) \\ &= 2E_C \left[n - \frac{Q}{e} + \frac{1}{2} \right] \\ &\stackrel{n=0}{=} 2E_C \left[-\frac{Q}{e} + \frac{1}{2} \right], \end{aligned} \quad (2.17)$$

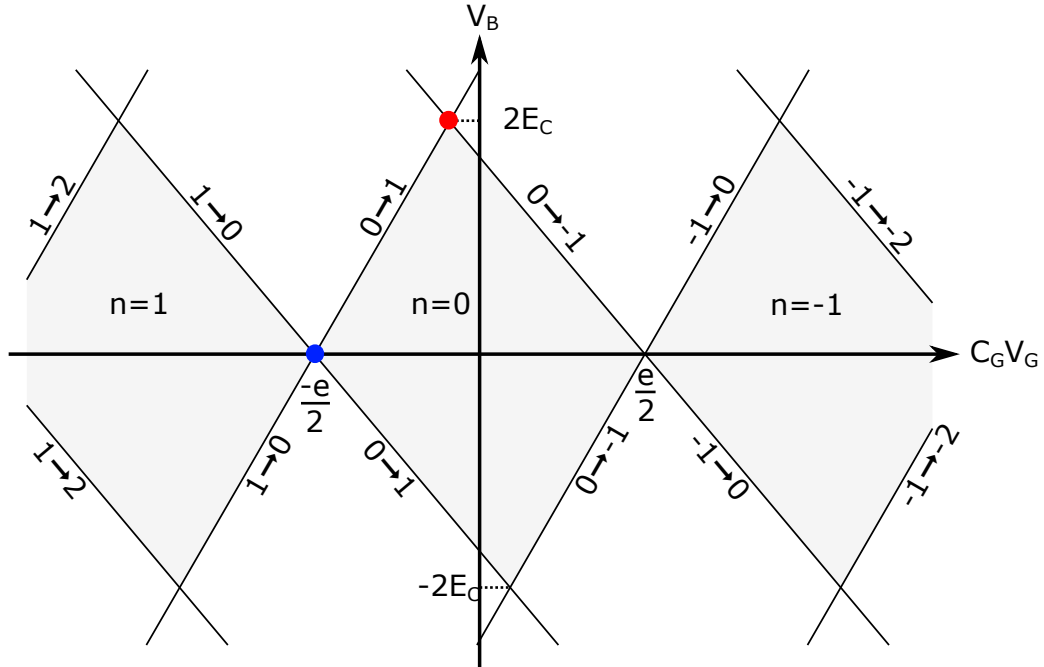


Figure 2.11: Stability diagram of a normal conducting SET. We have plotted the lines representing Eq. (2.16) for both junctions. The lines are e periodic along the gate axis. All lines are labeled with the number of excess charges on the island before and after the tunnel process across one of the junctions. Please note that by changing the bias polarity the label of the lines changes as well. Lines of the same slope represent tunnel process across the same junction.

Inside the gray areas the number of electrons on the island n is constant and no current can flow. This is the Coulomb blockade. If the gate voltage V_G is adjusted to an intersection of Coulomb diamonds (blue dot) the blockade is lifted. For high enough bias voltages $eV_B > 2E_C$ transport through the SET is always possible by elastic tunneling. This diagram is another representation of the explanations shown in Fig. 2.10. This representation shown here includes continuous changes of the gate charge Q and the bias voltages, while Fig. 2.10 only displays three different combinations of the bias and the gate voltage.

whereas for junction 2 the condition is given by

$$\begin{aligned} \kappa_2 eV_B &= E_Q(n) - E_Q(n+1) \\ &= 2E_C \left[-n + \frac{Q}{e} - \frac{1}{2} \right] \\ &\stackrel{n=0}{=} 2E_C \left[\frac{Q}{e} - \frac{1}{2} \right]. \end{aligned} \quad (2.18)$$

If we add up both of the equations the result is in agreement with the explanation above, namely

$$(\kappa_1 + \kappa_2) eV_B = 0. \quad (2.19)$$

Since all bias voltage needs to drop at the two junctions, the equation $\kappa_1 + \kappa_2 = 1$ holds and thus $(\kappa_1 + \kappa_2)eV_B = eV_B$.

This point where the conditions for the two junctions (Eq. (2.17) and Eq. (2.18)) are fulfilled is labeled in blue in Fig. 2.11. It lies on the V_G axis, therefore the charge states of the island are in

resonance to the leads (see Fig. 2.10a) and marks the starting point for this process to happen. The process gets poisoned (meaning superimposed by another process) as soon as it is possible to reach two different charge states, e.g. at the crossing of the lines labeled with $0 \rightarrow 1$ and $0 \rightarrow -1$ (marked in red in Fig. 2.11). Here, two different current cycles are possible: The $0 \rightarrow 1 \rightarrow 0$ and the $0 \rightarrow -1 \rightarrow 0$ cycle. By calculating the conditions for both lines and adding those up we derive under the assumption of $V_B > 0$

$$eV_B = 2E_C. \quad (2.20)$$

This is the Coulomb blockade threshold. For bias voltages higher than $eV_B \geq 2E_C$ there will always be a current flowing through the SET. This method only calculates the condition for the required bias value which is independent from the gate charge.

Chapter 3

Experimental Techniques

In this thesis we present transport measurements on superconducting single electron transistors. This chapter introduces the sample preparation and the measurement techniques.

3.1 Sample Preparation

The investigated SET samples consist of a square island made of aluminum. The island is contacted by an Al-AlO_x-Al tunnel barrier and a mechanically controlled break junction (MCBJ).

The samples are fabricated by electron beam lithography and thin film deposition. To derive a free standing constriction in the MCBJ a reactive ion etching process is necessary. The procedure is well documented in [Lor18; Spr16] so we will only give a short overview in this thesis and then focus on the most important steps.

3.1.1 General Process

The different steps of the sample preparation are depicted in Fig. 3.1. The substrate of the sample is a 18 mm × 3 mm (later on we have used a 22 mm × 3 mm) polished piece of phosphorus bronze (Fig. 3.1a). The used type of bronze is elastic down to very low temperatures so it provides enough restoring force to open and close the MCBJ repeatedly at low temperatures. Besides, it is nonmagnetic.

A layer of polyimide is spun on top of the bronze to provide electrical isolation of substrate and sample and to smooth the surface (Fig. 3.1b). It is also used as a sacrificial layer to obtain the free standing constriction after the etching step. It should be noted, that albeit the electrical isolation provided by the polyimide the metallic substrate will add an additional capacitance to the SET.

For the electron beam lithography, a double layer resist is required. This is formed by a MMA-MAA copolymer and a thinner PMMA layer (see Fig. 3.1c).

To pattern the sample we use electron beam lithography at 10 keV with an area dose of 90 – 150 $\frac{\mu\text{As}}{\text{cm}^2}$ (Fig. 3.1d). The lithography does not only expose the PMMA layer but it also creates a broadened structure in the copolymer by backscattered electrons.

The development of the exposed resist is done in a 1 : 3 MIBK:isopropanol solution for 20 – 25 s

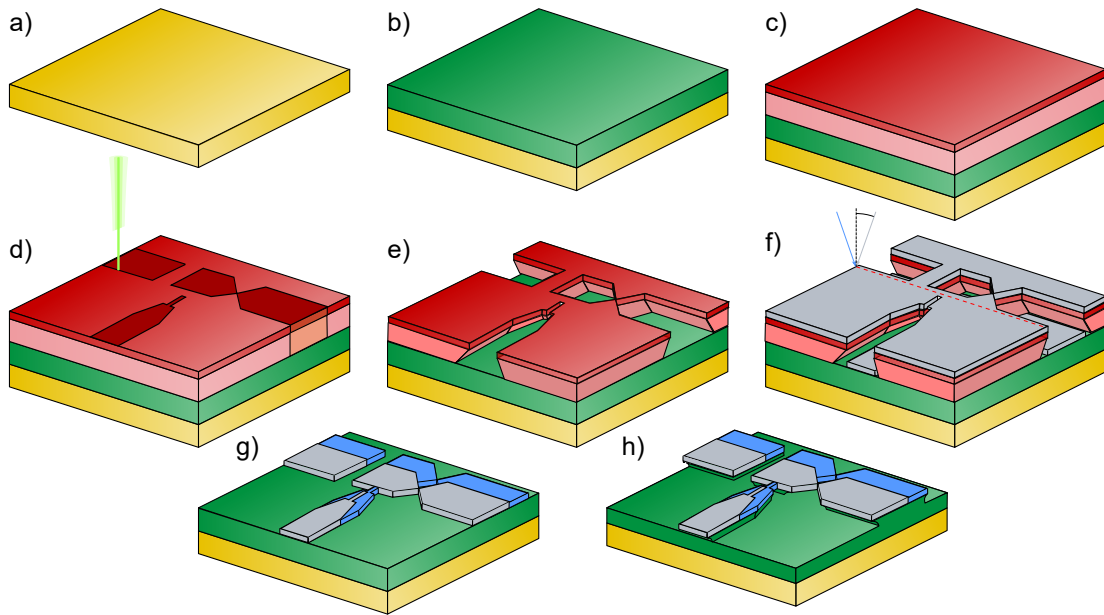


Figure 3.1: Schematic of the sample preparation. a) We use a polished piece of bronze as substrate. b) The substrate is covered with an electrically isolating layer of polyimide. c) On top of the sacrificial layer we spin a double layer of MMA-MAA and PMMA. d) The sample is patterned by electron-beam lithography. e) After the development the mask is free standing because of the double layer system. f) A shadow evaporation with an oxidation step in between is performed. g) After the lift-off only the sample structure remains. h) The sacrificial layer is partly removed by reactive ion etching. The constriction of the break junction is freestanding.

followed by bathing the sample for 4 – 5 min in isopropanol.

The structured PMMA layer now forms the mask needed for the evaporation whereas the copolymer is washed out in a broader area. This creates an undercut (Fig. 3.1e) that is necessary for the shadow evaporation and eases the lift-off later on.

A shadow evaporation creates the Al-Al_xO_x-Al tunnel barrier (Fig. 3.1f). We mount the sample in an ultra-high vacuum evaporator under an angle of –10° and cover it with 40 – 45 nm of aluminum. Without exposing the sample to air, this layer is thermally oxidized. Afterwards the sample is tilted to 20° and another 60 nm of aluminum is evaporated. The rotation axis of the sample is given by the axis orthogonal to the oxide contact (indicated by a red dashed line in Fig. 3.1f). All angles are measured between the direction of the evaporation and the perpendicular of the sample surface (as presented in Fig. 3.1f). Especially the oxidation defines the quality of the tunnel barrier and is discussed in more detail in Section 3.1.2.

By evaporating initially at a negative angle we evaporate the island, oxidize it and then cover it with a finger-shaped electrode to create the tunnel contact. The chosen angles determine the overlap area of the finger and the island.

A lift-off process is acetone removes the non-exposed resist and the aluminum film on top of it. After this step only the structure defined by the e-beam lithography remains (Fig. 3.1g).

A dry etching step finalizes the sample preparation. This is done by reactive ion etching using 50 volume fractions of O₂ and one volume fraction of SF₆ at a pressure of 1 mbar and a power

of 45 W. The etching process removes 500 nm of the sacrificial PMMA layer suspending the constriction (Fig. 3.1h).

3.1.2 The Tunnel Contact

There are a few requirements the tunnel barrier needs to provide. On one hand we would like to obtain high enough resistance R to fulfill the conditions of the Orthodox theory. Therefore R should be much higher than 25 k Ω . On the other hand, the resistance must be low enough that we can still resolve the changes of the break junction resistance. In the experiment we are only able to measure the break junction resistance in series to the tunnel barrier. Taking all of this into account we are aiming for resistances in the range of 30 k Ω – 200 k Ω .

Besides the resistance, the quality of the oxide layer is of interest. The oxide should act as an insulator allowing only quasiparticle and Cooper pair tunneling. Therefore, it must be homogeneous in its microscopic properties. Pinholes inside the oxide may give rise to conductance channels of intermediate transmission [Gre+11], which leads to transport via Andreev reflections.

Additionally, oxide barriers are known to host two-level systems [Gra+12; Lis+15; Pou+14]. They can act as an additional and fluctuating gate offset charge and thereby change the electrochemical potential of the island with respect to time. Thus, long-time measurements become challenging. The influence of the TLS becomes more important in the samples presented in this thesis since TLS are sensitive to mechanic strain [Gra+12].

The quality of the oxide can only be judged once the sample is cooled down and we have access to the microscopic transport properties.

The general fabrication process is described in detail in [Spr16]. The basic idea is to tune the thickness of the oxide by changing the oxidation pressure [Cai+11a; Cai+11b]. Since Briechle and Limbach [Bri04; Lim98] report an increasing amount of pinholes when using pure oxygen gas we use an Ar : O₂ 9 : 1 mixture for oxidizing the aluminum. Sprenger [Spr16] showed that this method results in nicely tuneable resistances of the tunnel barrier. The smaller the oxidation pressure (between 0.005 mbar and 1 mbar of absolute pressure) has been chosen the smaller was the obtained resistance. The resistances were reported to be between 20 k Ω and 160 k Ω but had a relatively large variation.

We assume that this variation is due to the surface roughness of the aluminum film. Conzelmann [Con16] investigated the film roughness and focused on the influence of the evaporation rate on the surface roughness. He determined that evaporation rates of 6 $\frac{\text{Å}}{\text{s}}$ result in the smoothest surface. Less surface roughness tends to result in smaller resistances but the variation of the obtained resistances did not decrease noteworthy.

Using the optimized evaporation rates and tuning the resistance by the oxidation pressure, we obtained a yield of minimum 2 out of 10 fabricated samples. The other samples were either short cut or had resistances above 10 M Ω . The majority of the non-working samples showed too high resistances.

In summer 2016 the above described and established fabrication process suddenly stopped working reliably and we were hardly able to produce any working sample at all. We did not change any of the external parameters deliberately such as the wafer, the evaporation machine, the metal or the gas mixture. The yield dropped to one sample featuring resistances above $25\text{ k}\Omega$ out of 20 fabricated ones. This sample showed pinholes and Andreev reflections at low temperatures. The non-working samples were mostly short-cut, whereas before summer 2016 the main error source had been too high resistances. Thus, we concluded the growth of the oxide layer to be in some way disturbed. We exchanged the metal as well as the gas for oxidation and used a new wafer but this did not change the sample yield noteworthy.

We tried to improve the oxide growth in several ways. First we started to use pure oxygen instead of the Ar : O₂ mixture again. We also oxidized the sample at much higher pressures up to 10 mbar to obtain a thicker oxide layer. Still the majority of the samples were short-cut.

Most of the literature focuses on Al/AlO_x fabricated SiO_x substrates, that are not covered with polyimide and are therefore not directly comparable. Pop [Pop+12] reported that left-overs of the electron sensitive resist can be implemented into the oxide and can give rise to pinholes. They suggested plasma etching with oxygen of the evaporation mask for cleaning the substrate. Since we do not have a cathode sputtering able to handle oxygen in our evaporator, we were not able to try this idea. Besides, this process would also affect our polyimide substrate and thereby roughen it. Instead, we tried intensive rinsing of the sample using isopropanol for up to 5 minutes. This improved the yield and the quality of the oxide, but we did not reach the values obtained before.

Holmqvist [HMP08] proposed a double oxidation scheme to improve the quality of the oxide layer. They use the oxidation process as described above as a first step and then cover the oxide with a very thin layer of aluminum. This thin layer is fully oxidized in a second oxidation process.

The sample we fabricated this way had a resistance of $195\text{ k}\Omega$ at room temperature. However, while cooling it down, the resistance increased to $2\text{ M}\Omega$. Furthermore, it did not show a linear IV-trace, as we observed for the other tunnel junctions. Instead the observed IV-curve was mostly linear but heavily disturbed in terms of additional random variations of the conductance. We suspect that there are still aluminum grains in the oxide which are the reason for the observed variations. Using thinner aluminum layers for the second oxidation might improve the result but we valued the risk for remaining aluminum grains to be too high. Thus, we did not pursue this method further.

Instead we tried another approach of oxidizing the aluminum in an oxygen plasma. This experiments have been conducted in collaboration with P. Haiber [Hai18].

To fabricate the sample, the first layer of aluminum was evaporated as usual. For the oxidation, the samples were transferred to a reactive ion etching machine (RIE). It was not possible to do the transfer in vacuum. Afterwards the sample is transferred back into the evaporator and the oxide is covered with a second layer of aluminum. He tried to keep the sample in a nitrogen atmosphere while transporting it, but the only available box was a self-built nitrile bubble filled with nitrogen at room pressure. Nitrile is not completely leak tight so it might be possible,

that the sample was in contact with air while it has been transferred from one machine to the other.

First oxidation tests with 0.01 mbar of O₂ and 35W of plasma power resulted in resistances of 1 – 100 GΩ. The longer the sample was exposed to the plasma, the higher was the resistance. To decrease the resistance, a new recipe using an Ar : O₂ mixture at a partial oxygen pressure of 0.001 mbar and 35W of plasma power was tested. All fabricated tunnel junctions were destroyed by static electric charge, so we are not able to characterize the new recipe in terms of junctions resistance.

The resistance obtained at 0.01 mbar of O₂ is quite surprising since oxidizing the sample at those pressures in the evaporator mainly gave short-cut samples. The main difference of the two methods is of course the plasma and the fact that in the evaporator we can only use static pressures, whereas in the RIE we use a gas flow. Hence, we tested if there is a difference between oxidizing in a static pressure or in a gas flow by transferring the sample to the RIE and setting the pressure to 0.01 mbar and the flow to 50 sccm without igniting the plasma. This sample had a resistance of around 7 MΩ, which is still very different from the result obtained in the evaporator.

To qualify the influence of ambient air on the oxide growth we exposed one sample to ambient conditions for one minute. The resulting resistance was in the range of a few 100 kΩ. Since the partial pressure of oxygen in room air is about 200 mbar and we were aiming for resistances in a range slightly below, we went over to oxidizing the samples again in the evaporator at absolute pressures of 2 – 100 mbar. This resulted in resistances of about 200 kΩ, that did not show any dependence of the used pressure.

With this new scheme, the yield increased again to 2 out of 10 samples. However, it is still not known what has been the cause for the temporary decrease in the yield. It is also unclear why now pressures 10 – 100 times higher than before July 2016 are required to obtain similar resistances.

3.1.3 Sample Geometry

The layout of our sample is different from the one commonly found in literature [FPT98; Ful+89; HTT94; LHT98]. Usually one aims for island having a small surface area to decrease the capacitance of the island with respect to the surrounding. Figure 3.2a shows the evaporation mask of the sample. It consists of a 2 μm × 2 μm squared island with a break junction (BJ) attached to the left. The electrode on the right side of the sample (GE) serves as gate electrode. The Al-AlO_x-Al tunnel barrier (TB) is placed orthogonal to the axis of the BJ. Figure 3.2b shows the fully processed sample. The double BJ is a result of the shadow evaporation.

We need to make a few remarks on why we choose this geometry. The island is rather large compared to other SET designs. In general, small islands are preferred to decrease the capacitance resulting in high charging energies. Our decision is owed to the fact that the island needs to withstand the mechanical force required to break the BJ. In the sample preparation process, we remove part of the sacrificial layer to obtain a free standing constriction of the BJ. This also

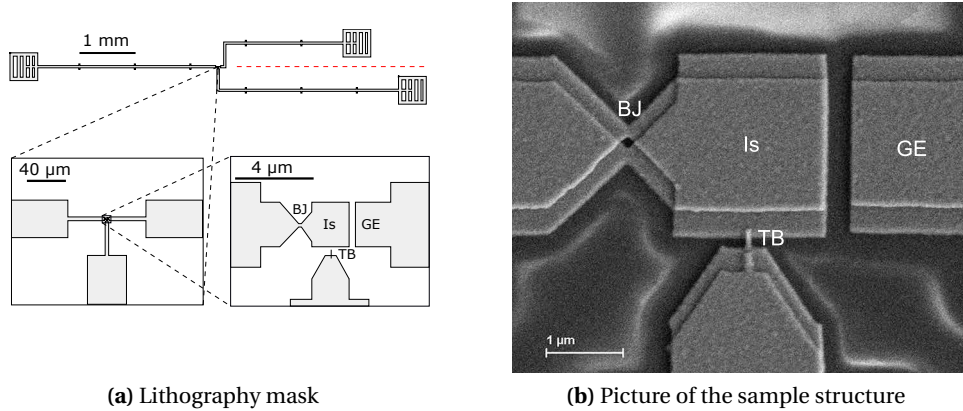


Figure 3.2: Lithography mask and electron microscope picture of the SET samples (a) Schematic of the evaporation mask. The top picture shows the leads and the contact pads. The red dotted line is parallel to the rotation axis used for the shadow evaporation (see Section 3.1.1). The picture (down left) shows the smaller leads that are connected to the inner structure. Magnifying the down left picture the inner structure featuring the island (Is), the gate electrode (GE) and the constriction of the break junction (BJ) become visible. In the evaporation mask the tunnel barrier (TB) has no physical connection to the island. This connection is created by shadow evaporation. (b) Electron microscope picture of the SET sample with the island (Is) in the center. The gate electrode (GE) is placed left of the island and opposite the break junction (BJ). A small metal finger lying on top of the oxidized surface of the island forms the tunnel barrier (TB). The doubling of the structure with a slight shift is caused by the shadow evaporation.

removes a part of the sacrificial layer under the island reducing the area available to carry the force.

Nonetheless since we use the thick polyimide layer to electrically isolate the island from the substrate, the capacitance from the island to the metallic substrate is not dominating. Thus, the size of the island may be chosen larger in comparison to other reported designs. Besides, we also need to consider the influence of mechanical stress to the oxide barrier. It has been reported that two-level systems incorporated in the oxide do react to mechanical stress [Gra+12; Lis+15; Lor18]. Since those two-level systems can influence the electrostatic potential of the island [Pou+14] reducing the mechanical stress to them is helpful. Thus we designed the tunnel barrier to be orthogonal to the bending of the sample.

There is no distinct reason besides of practical handling to place the gate electrode to the right of the island. We have not observed any change in the gate capacitance due to bending. The influence of the double BJ caused by the shadow evaporation is discussed in detail in [Lor18].

3.2 The Mechanical Setup

For the measurements presented in this thesis very low temperatures are required. Aluminum as a superconductor has a critical temperature of $T_c = 1.2\text{K}$. We aim to describe the superconductivity within the zero-temperature limit of the BCS theory, so temperatures way below T_c

are inevitable.

The charging effects require low temperatures as well. The SETs presented in this work have charging energies around $100\mu\text{eV}$ corresponding to a temperature of 1.15 K .

Additionally we need a mechanics operating at low temperatures to manipulate the BJ and form atomic contacts. In the following section we will introduce the setup used to match all requirements.

3.2.1 The Cooling System

We use the commercially available dilution refrigerator "AirLiquide MaxDil 100" for cooling the sample. The mode of operation of a dilution system is covered in several books, e.g. [Pob07]. We will focus here on the special features of our system.

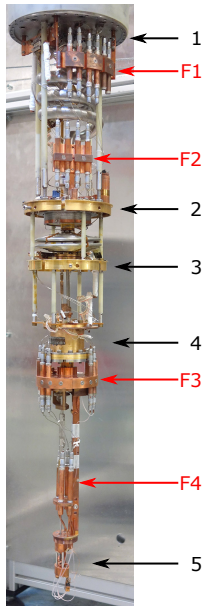


Figure 3.3: Photograph of the cooling system and the wiring in the low temperature area of the cryostat. The IVC can be mounted at the IVC plate (1). During operation the IVC will completely be immersed in liquid helium which provides a constant temperature of 4.2 K at the IVC plate. An additional heat shield made of copper is mounted at the still plate (2) during the measurements. The still is typically at temperatures of 700 mK . The cold plate (3) should form an additional temperature stage. Since in this setup the heat exchanger between mixing chamber and cold plate is missing the thermal coupling between these two parts is higher than originally intended. The mixing chamber (4) is the coldest part of the cryostat with a temperature $\leq 35\text{ mK}$. The sample chamber (5) reaches $\leq 50\text{ mK}$. The photo also shows the filters of the electrical setup (see Section 3.3.1). The RC filters (F1) are mounted at 4.2 K . We use copper powder filters at the still (F2), the mixing chamber (F3) and at the inlet of the sample chamber (F4).

Inside the cryostat we use heat shields to separate different temperature regimes. The inner vacuum chamber (IVC) rests in a liquid helium bath and thus has a temperature of 4.2 K . The still has a typical temperature of $600\text{ mK} - 800\text{ mK}$. Since we are missing the heat exchanger between the mixing chamber and the cold plate, the latter is at temperatures of 70 mK . With all necessary wiring and the mechanics mounted, we reliably reach temperatures $T \leq 35\text{ mK}$ at the mixing chamber.

3.2.2 Breaking Mechanics

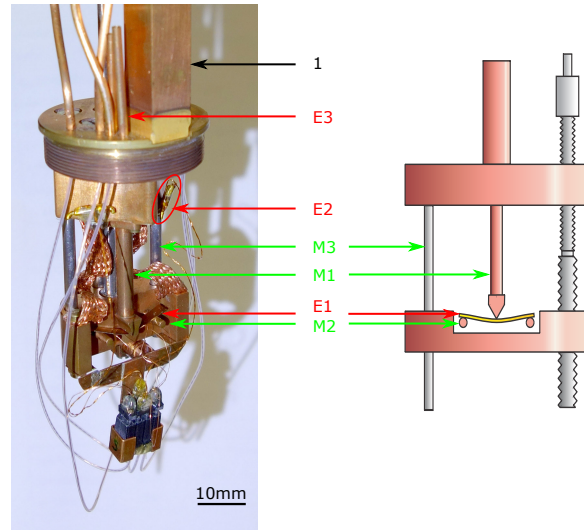
The breaking mechanics used for the measurements presented in this thesis is described in detail in [Lor18]. In this section we will only shortly summarize the properties of the mechanics. Figure 3.4 shows the sample chamber where the breaking mechanics is mounted. The mechanics consists of two counter supports (M2) on which the sample is placed. The table with the

counter support is moved against a static stamp (M1). Since the free standing bridge creates a $1 : 10^4$ gear reduction, the bending of the sample allows a very precise manipulation of the break junction.

The table holding the sample is moved using a differential rod. One turn of the rod moves the table by $100\mu\text{m}$. Two guiding rods (M3) guarantee a smooth movement.

Figure 3.4: Photograph of the sample chamber and schematic of the breaking mechanics. The thick copper bar (1) is the connection to the mixing chamber. The counter supports (M2) can be moved against the static stamp (M1) to bend the sample. The counter supports are fixed on the table that is moved by a differential screw (not visible) along the guiding rods (M3).

The electrical components (see Section 3.3) are marked in red. The sample (E1) is lying on the counter supports and electrically connected to the reference resistors (E2). The measurement cabling enters the chamber through thin capillary tubes made of copper (E3).



The breaking mechanics is connected to a step motor via several drive shafts and gearings. Since the cooling system needs a lot of space inside the cryostat, there is no line-of-sight port from the room temperature part to the sample stage. Therefore the axis of the rotation needs to be offset. The additional gearings also help to avoid unwanted friction due to non-centered guidings. The complete mechanical drive is described in detail in [Lor18], chapter 3.2.

3.3 Electrical Setup

For the work presented in this thesis the setup designed and built by Thomas Lorenz is used. He gives a detailed description in his PhD thesis [Lor18]. In the following section we will focus on the main characteristics of the setup.

The measurement needs to meet several requirements. It is necessary to resolve a broad range of resistances of the BJ (between $10\text{k}\Omega - 2\text{M}\Omega$). Furthermore, a high dynamical resolution of the current is required. Inside the superconducting gap, currents are around 10pA whereas outside the gap several 100nA are flowing. Additionally, the electronic system of the sample is sensitive to interference. Thus, we need to suppress all sources of interference like thermal noise, interference by external noise sources and thermoelectric voltages. Below, the realized measurement concept is described and schematically displayed in Fig. 3.5.

In principle we use a four-point measurement scheme. We apply a quasi-DC bias (meaning frequencies $f \leq 1\text{Hz}$, sinusoidal) that is symmetric in respect to ground. The sample is framed by two symmetrically distributed reference resistors in series. We limit ourselves to

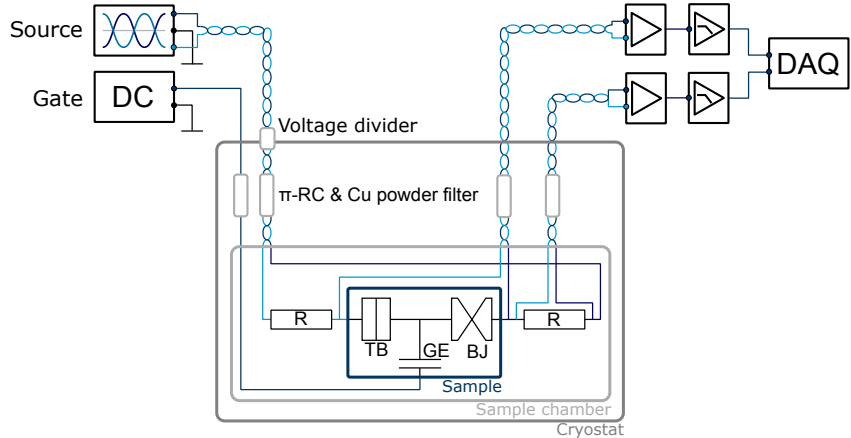


Figure 3.5: Schematic representation of the electrical setup. The sample consisting of break junction (BJ), tunnel barrier (TB) and gate electrode (GE) is connected in series to two reference resistors. The bias is applied over sample and reference resistors which preserve the symmetry of the bias. At the feedthrough from room air into the cryostat a symmetric voltage divider reduces the source voltage. All lines are filtered inside the cryostat using RC and copper powder filters. Outside the sample chamber all cables are fabricated as twisted pairs to benefit from the high common mode rejection. The gate voltage is applied with respect to the ground defined by the symmetry of the bias. The voltage dropping over sample and reference resistor, respectively, are measured differentially. Both signals are amplified by a series of two amplifiers and converted to digital signal by an analog digital converter during the digital data acquisition (DAQ).

measurements of voltage differences instead of measuring voltage and current. Therefore, we measure the voltage drop over the sample and over one of the reference resistors. This way the reference resistor is used to calculate the current. Additionally, the reference resistors limit the current when the sample has a high differential conductance.

The gate voltage is applied with respect to ground defined by the symmetry of the bias. We refrain from using a lock-in amplifier since this will influence the resolution of the DC measurement.

Reduction of External Noise Sources

We have taken several measures to reduce the influence of external noise sources.

High frequency noise in the measured signal is efficiently suppressed by the DC bias and long measurement times followed by averaging. To avoid influences on the transport properties, we need to add filters to the wiring as described below. Additionally, the cryostat with its thermal shielding acts as a Faraday cup.

Low frequency noise, and hereby especially the 50Hz line frequency, influences mainly the measurement resolution. Besides of filtering we have also taken care to avoid external influences. We have separated the protective earth of the used instruments from the measurement ground. This requires floating voltage sources for bias and gate.

Ground loops are avoided as well as possible.

We separated the phases of the mains supply. All sensitive instruments are connected to one

phase, whereas “dirty” instruments like pumps are connected to another phase. A detailed description how this was realized is given in [Lor18].

3.3.1 Wiring and Filters

The measurements requires the wiring to fulfill the following tasks: the suppression and filtering of external and internal interference, the cooling of the electronic system and a low heat input into the cryogenic system. We use a symmetric wiring to compensate thermoelectric voltages. The cables are twisted pairs to use the intrinsic common mode rejection.

Thermalizing the wires is essential to decrease the heat load brought to the cryogenic system. Copper powder filters have proven to optimize the thermalization of the wires themselves. They provide high damping of electromagnetic input for a broad frequency range above $f \geq 1\text{ GHz}$. The working principle and the characteristics of those filters are described in [Sch09; Tha+17]. To cool down the electronic system efficiently we have placed several stages of copper powder filters at the still plate and at the mixing chamber. A third set of filters is attached to the low-temperature chamber where the sample is mounted.

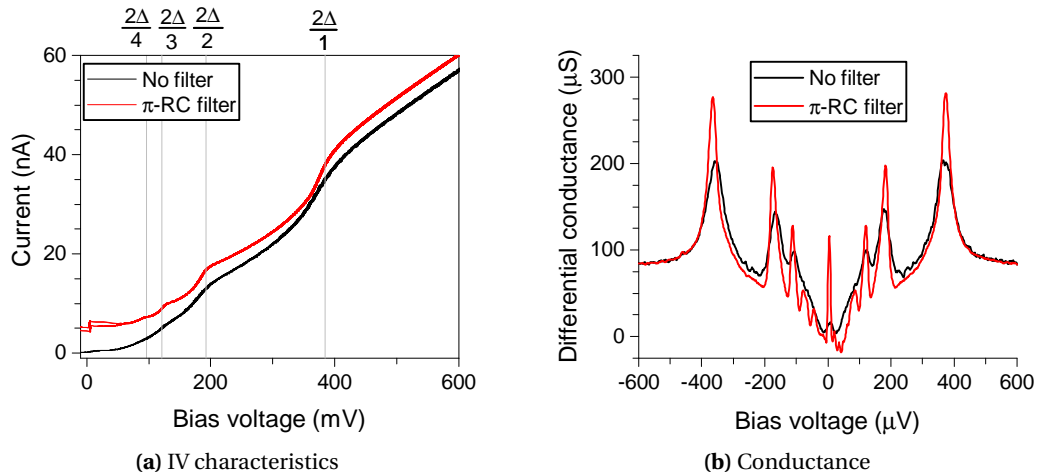


Figure 3.6: IV characteristics and numerically calculated differential conductance traces of an aluminum single-atom contact with $R = 12\text{ k}\Omega$. The comparison between the filtered and an unfiltered measurement is displayed. The filters used are π - RC filters with a cutoff frequency of 100 kHz . The traces in (a) are offset by 5 nA for clarity. The filtered measurement shows higher-order Andreev reflections as well as a supercurrent. (b) The improvement by the filtering is also noticeable in the conductance trace. The maxima caused by the Andreev reflections are higher and much sharper. Here, we present only the differential conductance of the up-sweep of the bias voltage. The observed supercurrent leads to a jump to high bias voltages as soon as the current exceeds the supercurrent. This jump stretches over approximately $70\text{ }\mu\text{V}$ covering the higher-order Andreev reflections for positive bias voltages. For negative bias voltages we observe all orders of Andreev-reflections.

A stable and low-noise bias voltage is essential to obtain high-resolution measurements. Figure 3.6 shows an IV trace and the corresponding derivative of an aluminum contact in the single-atom regime with (red line) and without (black line) an additional RC low-pass

filter (cutoff frequency $f_{co} \approx 100\text{kHz}$) in the source and the measurement line. In the filtered signal multiple Andreev reflection of 4th order are observable as well as a supercurrent. This measurement has been taken with RC filters at room temperature. Meanwhile we implemented π -shaped RC filters at the 4.2 K stage. The filter design is described in [Lor18].

Inside the IVC all cables are made of Manganin wires. The twisted-pair cables are inserted in thin capillary tubes made of stainless steel. The tubes have an inner diameter of $120\mu\text{m}$. The capillary cables provide a very efficient damping of high frequencies. We measured -20dB damping for frequencies $f > 1\text{GHz}$ and -80dB damping for frequencies $f > 10\text{GHz}$. Besides, the used materials are poor thermal conductors. This decreases the heat load brought to the cryogenic system by the wiring.

The filters and the wiring limit the bandwidth available for the measurement. The reference resistors and the sample interact with the RC filters and eventually decrease the cutoff frequency. This is especially the case when the BJ is fully opened. In this case we estimate the cutoff frequency to be around 200 Hz.

Furthermore, the twisted-pair design of the cables create a relatively high inductive and capacitive coupling. This does not affect real DC measurements but needs to be taken into account for our quasi-DC bias. The coupling will cause a phase shift between the reference and the sample signal if the frequency of the bias is chosen too high.

3.3.2 Measurement Electronics

In the following section we will introduce the measurement instruments and their specific properties required to realize the measurement concept.

We use a Stanford Research System function generator model DS360 as voltage source for the quasi-DC bias. It can create low-noise sinusoidal signals of variable frequency ($10\text{mHz} < f < 10\text{kHz}$) and amplitude ($20\mu\text{V} < V_{PP} < 40\text{V}$). The instrument offers the possibility to generate the signal symmetrically around a common-mode potential. This potential can be adjusted to measurement ground, so the signal is symmetric with respect to ground.

Before digitizing the voltage signals over the sample and the reference resistor we need to amplify them to $1\text{V} < V < 5\text{V}$. To this end, we use an amplifier chain. The preamplifier is a NF LI-75A model with a differential input and a constant gain factor of 100. We use Stanford Research Systems amplifiers (model SR560) with variable gain and adjustable filtering as the second amplifier stage.

The amplifier chain offers several benefits. The NF LI-75A amplifiers have very low differential current offsets and low-noise inputs. On the other hand the constant gain factor of 100 is not sufficient for all measurements since the sample resistance changes when the BJ is adjusted. To obtain an optimal digital resolution of the data acquisition (DAQ) we would like to match the amplified signal to the input range of the DAQ. This problem is solved by the variable gain factors of the SR560 amplifiers. Another benefit of the amplifier chain is the protection of the sample against voltage peaks occurring when switching the parameters of the SR560 amplifier.

On the other hand one needs to consider the behavior of the DC-offsets carefully, since the offsets created by the preamplifiers will be amplified later on. Therefore we always adjust the offsets with an accuracy of $100\text{ }\mu\text{V}$ before every measurement. The remaining offsets are measured while the source is turned off and subtracted later within the data processing.

The analog signal is digitalized using the National Instruments USB-6218BNC data acquisition card. The inputs of this DAQ are floating to sustain the concept of a differential and floating measurement. Each channel is sampled with 50 kHz. The input range is set to $\pm 5\text{ V}$.

The temperature is monitored by a TRMC2 temperature measurement bridge from Air Liquide. A Twickenham SMC 80-10 power supply feeds and controls the superconducting magnet in the dewar.

3.4 Data Acquisition and Processing

After introducing the measurement concept in the previous section we will now focus on the data acquisition and processing.

We apply a constant gate voltage and vary the bias in a sinusoidal manner. We always record several periods of the sinusoidal signal in high resolution for one fixed gate voltage. This process is repeated for several gate voltages. During the data processing (see Section 3.5) we calculate one IV trace for each gate voltage using all recorded periods for this gate value.

Whenever we only want to measure opening- and closing traces to create conductance histograms the sole parameter we are interested in is the overall conductance. To do so, we still use the sinusoidal bias but calculate the conductance in the normal conducting state on the fly instead of recording complete IV traces. The measurement control directly calculates the conductance using the IV traces.

3.4.1 Settings of the Data Acquisition

For measuring the transport properties of the SET samples we vary the bias at frequencies of $20\text{ mHz} \leq f \leq 250\text{ mHz}$. This frequency is a 100-times smaller than the bandwidth of the wiring (see Section 3.3.1) and the low pass filters usually set at the amplifiers ($f_{LP} = 30\text{ Hz}$). To measure conductance histograms higher frequencies $1\text{ Hz} \leq f \leq 5\text{ Hz}$ are used. The bias amplitude is always adjusted with respect to the contact resistance.

We set the data acquisition rate to 50.000 samples per second per channel. To decrease the digital and the analog noise we *in situ* sample down the data to 5 kHz by averaging over 10 data points. The data based on the 5 kHz timescale is stored as raw data.

3.4.2 Measurement Procedure and Data Storage

At the time of writing this thesis a full automatization of the measurement and the data storage is available. The software was written by Thomas Lorenz [Lor18].

The only parameters to be set manually are the bias frequency and amplitude as well as the amplifier gain and filtering. After defining the gate voltage range and its step size the measurement runs automatically.

The working principle is the following: First external parameters like amplifier settings, magnetic field, bias settings and reference resistance are stored. Then the gate voltage is set. The bias source is shorted to ground to measure the DC offset for 5 s. Afterwards the bias source is turned on and several periods of the sinusoidal signals are recorded.

According to the trigger of the bias source the recorded signal is cut into several chunks. Each chunk contains one period. The chunks are stored in a binary data format. The additional parameters like gate voltage, time stamp, temperature and the measured DC-offset are stored as well. The pre-evaluation offered by the measurement control (e.g. the DC offsets and the resistance calculation (see next section)) is added to the storage.

Afterwards a new gate voltage is set and the procedure starts again. The measurements for all gate voltages are stored in one file, so that a complete gate-bias-map is available after the measurement.

Resistances in the SET

In the SET samples it is not possible to measure the conductance of the BJ directly. The only possibility to estimate the resistance of the BJ, is to measure an IV traces of the SET sample and calculate the resistance of the complete sample. After subtracting the resistance of the tunnel barrier we can assess the resistance of the BJ.

Since the IV traces of a SET is highly non linear, extracting the resistance is not trivial. Our measurement control offers five different methods to calculate the resistance. We will shortly introduce the methods and their advantages and disadvantages.

The easiest approach is to use the peak-to-peak amplitude of the current and voltage signals. The thus calculated resistance is very sensitive to noise. Using the RMS amplitude is more robust against noise. Both methods give good results for very large amplitudes even if a Coulomb staircase still modulates the IV trace.

Another approach is to use a linear regression of the IV traces at high bias. This method reacts sensitively to remaining Coulomb staircase modulations. The approach is improved by using the shape of the sinusoidal bias. We can calculate the amplitude of the signals by a non linear regression of a sinusoidal signal. If the signal shows time shifts between current and voltage signals, a phase-corrected sinusoidal function is used. This method gives the most precise results but it is numerically challenging. If the measurement frequency is too high, the fit simply has not enough time to converge properly. In [Lor18] a detailed description is given.

3.5 Digital Data Processing

As described above, we measure a sinusoidal voltage and current with respect to time. Besides a reduction of the number of data points we do not alter the data in any way, for example by scaling. We use the raw data and apply numerical filters, scaling and conversion when analyzing the data.

The digital data processing and the graphical presentation is done by self-developed tools within the Software Origin [Lor18].

3.5.1 Conversion from Time Traces to IV Characteristics

In many cases the IV characteristic is of interest and not the time dependence of the current and voltage. For our measurement we collect data at a high sampling rate for several periods of the applied bias.

To convert this to an IV trace we use statistical data binning (see e.g. [Pie15]). Current and voltage are linked by the time. We divide the voltage axis in equally spaced bins and collect all voltage points that fit into one of the bins. To calculate the current value for this voltage point we average over all current data points that have the same time stamp as the voltage points inside the bin.

The statistical data binning reduces the amount of data points from much more than 100000 to the desired value. We benefit from this method in terms of noise reduction and data handling. The used bins represent equidistant nodes that are required for the derivation of the IV traces and the graphical representation. The binning reduces statistical noise and can suppress periodic interference. The efficiency of the suppression strongly depends on the frequency of the bias, the number of bins and the number of recorded periods.

The chosen averaging by binning requires that the same effects create the same signature in every repetition of the measurement. We sort the data with respect to the sweep direction of the bias to avoid influences by hysteretic effects.

In [Lor18] it is explained in detail how the statistical data binning may change the data.

3.5.2 Digital Filtering and Derivation

Besides the data binning additional digital filtering is needed. One can either filter the time-dependent data before the conversion or use filters after the conversion. In the first case the filters act as additional low pass filters, in the second case the filters act directly on the current. It is possible to use different filters but we will focus here on the ones we usually use. Before converting the data, we use a moving-average filter. If the window width is chosen properly, this procedure filters periodic interferences very efficiently.

A Savitzky-Golay smoothing is used after the conversion. This also offers the possibility to calculate the numerical derivative of the IV traces, to obtain the differential conductance. The

presentation of the differential conductance instead of the current allows to display features of very different current amplitude within one plot.

Chapter 4

The Superconducting Single Electron Transistor

In the superconducting SET (SSET) one can observe the interplay of superconductivity and Coulomb blockade. One the one hand, due to the superconductivity the electronic system gains energy when electrons pair up to Cooper pairs. On the other hand, the charging effects caused by Coulomb blockade make this pairing energetically non-favorable.

There are three energy scales defining the behavior of the SSET. The Josephson energy E_J describes the coupling of two superconductors through a junction. The superconducting gap Δ characterizes the superconductivity itself whereas the charging energy E_C describes the Coulomb blockade.

The best-known characteristic of a SSET is the parity effect. For $E_J i < E_C < \Delta$ the Coulomb blockade oscillations at zero bias become $2e$ periodic instead of the e periodicity observed for normal conducting SETs. The reason is the sensitivity of the island on the parity of charges. Odd numbers of charges require an unpaired quasiparticle and thus the extra energy Δ . Thus, the system's free energy for odd charge states is shifted up (c.f. Fig. 4.1a).

The experimental manifestation of the parity effect is the crossover of the periodicity of the Coulomb blockade oscillations from e to $2e$ as shown in Fig. 4.1b. The parity effect is very sensitive to interferences like increased temperatures [THL95] or finite bias voltages [Tuo+93], since those create excited quasiparticles.

In this thesis we focus on SSETs heaving a low coupling $E_J i \ll E_C$, so charging effects are observable. Additionally, we would like to study the influence of superconducting transport phenomena like the Josephson effect on the Coulomb blockade. Hence it must be easier to charge the island than to break a Cooper pair. This leads to the condition $E_C < \Delta$ implying the condition $E_J i \ll \Delta$. The condition for the Josephson energy must be fulfilled for both junctions independently. For tunnel barriers we may use Eq. (2.5) and Eq. (2.6). In this case the condition is equivalent to the requirement for high resistances in the normal conducting SET $R \gg R_K$.

4.1 State of Research

The developement of the concept of a SET in 1987 Fulton and Dolan [FD87] and Likharev [Lik87] opened a new field of research. The SET proved to be a testbed for new application

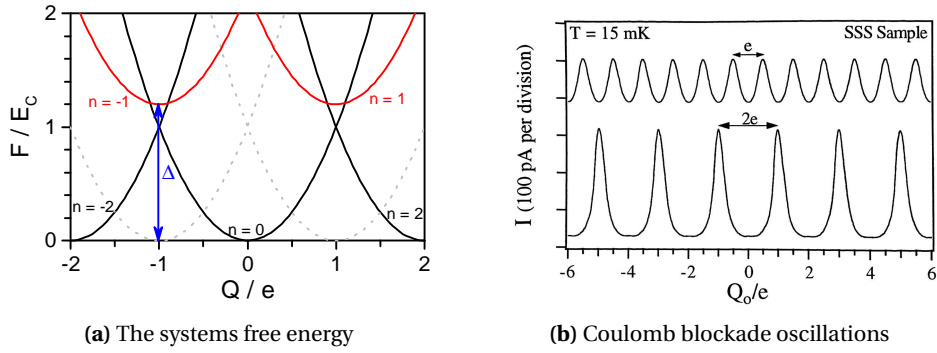


Figure 4.1: The parity effect in superconducting SETs. (a) Representation of the systems free energy with respect to the gate induced charge Q and the charge state n for zero bias voltage. All charge states featuring an odd number of particles are shifted to higher energies. In a superconductor single charges are always excited quasiparticles, having an energy of Δ . Thus, the system's free energy transforms from an e periodicity in the normal conducting state (black and gray) to a $2e$ periodicity in the superconducting state (black and red). Taken from [Lor18]. (b) Coulomb blockade oscillation of a SSET. The oscillations in the normal conducting state (top) show an e periodicity in the current modulation. In the superconducting state (bottom) the oscillation become $2e$ periodic. Taken from [Her95].

possibilities of charging effects as well as for research on basic physical questions. Especially the stability of the Coulomb blockade has been of interest.

Various parameters can influence the charging effects. Following [Wal+02] the Coulomb blockade breaks down for $E_C/k_B T \approx 1$. Already at $E_C/k_B T \lesssim 0.1$ a smearing of the Coulomb blockade is observed.

An intensively researched topic has been the question how the Coulomb blockade behaves for strong coupling $R \approx R_K$. Several publications show, that charging effects persist for low resistances [Cho+99; JED98; Joy+97; Wal02; Wal+02]. There are several theoretical models for various coupling [FM95; Göt90; GG90; KSS97].

This indicates that the resistance is not sufficient to describe the coupling. In more recent publications it has been shown that in fact the breakdown of the Coulomb blockade is linked to the transmission of individual channels [Jezz+16; Pas+93b]. Those experiments used SETs defined in two-dimensional electron gases. For metallic SETs it has been discussed as well [JED98].

Möller et al. [Möl+98] have observed a linear decrease of the charging energy with increased coupling. Several different scaling behaviors have been predicted [FSZ95; Fle93; WG96].

Already in 1989 the interplay of superconductivity and Coulomb blockade attracted the interest of Fulton [Ful+89]. Especially the parity effect in completely superconducting SETs has gained much attention [Joy95; ML97; SZ94; SS96; Tuo+92]. It has also been observed for normal conductor-superconductor-normal conductor (NSN) SETs [EDM94; EMD93; HTT94].

The parity effect as explained in the section above covers only the behavior at zero bias. For finite bias many current cycles consisting of combined Cooper pair and quasiparticle transport have been found [Ful+89; Had+98; Joy95]. Fitzgerald et al. [FPT98] discovered the contribution of Andreev reflection in all-superconducting SETs, which before had only been known for NSN

SETs [HTT94]. In 2017 Lorenz et al. [LSS18] observed current cycles due to multiple Andreev reflection in a SSET.

4.2 The SSET at Finite Bias

This thesis aims at investigating multiple-charge transport through the SSET. Thus the regime of finite bias voltage is of interest. We will use an expansion of the Orthodox theory sec:SET (see also Section 2.3) to describe the transport through the SSET in the case of $E_J \ll E_C \ll \Delta$. As in the Orthodox theory, we assume that the number of electrons on the island n is well defined before and after tunneling. This implies that the transport through the two tunnel junctions is independent of each other. A current through the SSET is only observed when it is possible to compose a closed cycle of tunneling events charging and discharging the island. [FPT98] and [Poh99] give a good introduction on how to compose current cycles of different superconducting transport processes. The different cycles can be identified in a bias-gate contour plot.

4.2.1 The Voltage Divider

The SET forms a capacitive voltage divider. In Section 2.3.2 we introduced κ_i as the parameter defining the voltage drop over junction i . We need to modify the schematic model presented in Fig. 2.9 to implement the additional capacitance to ground that results from the sample preparation (c.f. Section 3.1.3).

Figure 4.2 shows the equivalent circuit diagram of our sample.

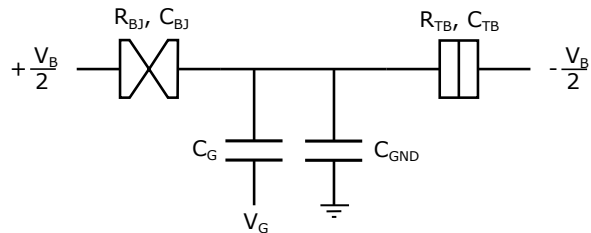


Figure 4.2: Equivalent circuit diagram of the SET sample used in this thesis. The model is similar to Fig. 2.9 but features an additional capacitance to ground caused by the metallic substrate. Taken from [Lor18].

The additional capacitance C_{GND} modifies the capacitance of the island $C_{\Sigma} = C_{\text{BJ}} + C_{\text{TB}} + C_{\text{G}} + C_{\text{GND}}$. Since the additional capacity connects to ground we can simply include it into the electrostatic energy of the SET

$$E_Q(n) = \frac{(Q - ne)^2}{2C_{\Sigma}} \quad (4.1)$$

by adding a constant offset charge Q_0 to the gate induced charge, $Q = C_{\text{G}} V_{\text{G}} + Q_0$.

With those considerations we can calculate the fraction of bias voltage available on both contacts, $V_{BJ} = \kappa_{BJ} V_B$ and $V_{TB} = \kappa_{TB} V_B$.

We use the definition

$$\delta C := C_{BJ} - C_{TB} \quad (4.2)$$

and the capacitive voltage divider to calculate κ_i :

$$\kappa_{BJ} := \frac{V_{BJ}}{V_B} = \frac{C_{TB} + \frac{C_G + C_{GND}}{2}}{C_\Sigma} = \frac{1}{2} - \frac{\delta C}{C_\Sigma}, \quad (4.3a)$$

(4.3b)

$$\kappa_{TB} := \frac{V_{TB}}{V_B} = \frac{C_{BJ} + \frac{C_G + C_{GND}}{2}}{C_\Sigma} = \frac{1}{2} + \frac{\delta C}{C_\Sigma}. \quad (4.3c)$$

Thus, the capacitance of junction i defines the fraction of bias voltage available for transport over junction j .

4.2.2 Transport Diagram of the SSET

We expand the concept of the stability diagram (c.f. Section 2.3.2) to a superconducting transport diagram. Therefore, we need to count the number q of quasiparticles that each superconducting transport creates and the number m of electrons transferred. We focus on positive bias first ($V_B > 0$), assuming charging the island through the tunnel barrier and discharging it through the break junction. Considering those preconditions Eq. (2.16) transforms to

$$\begin{aligned} meV_{TB} &= me\kappa_{TB}V_B = E_Q(n+m) - E_Q(n) + q\Delta \\ &= 2mE_C \left(\frac{C_G V_G + Q_0}{e} + n + \frac{m}{2} \right) + q\Delta \end{aligned} \quad (4.4a)$$

$$\begin{aligned} meV_{BJ} &= me\kappa_{BJ}V_B = E_Q(n-m) - E_Q(n) + q\Delta \\ &= 2mE_C \left(-\frac{C_G V_G + Q_0}{e} - n + \frac{m}{2} \right) + q\Delta. \end{aligned} \quad (4.4b)$$

For negative bias voltages ($V_B < 0$) we need to change the sign of the electrical work and take into account that transport through the BJ now charges whereas transport through the TB discharges the island.

$$-mek_{BJ}V_B = 2mE_C \left(\frac{C_G V_G + Q_0}{e} + n + \frac{m}{2} \right) + q\Delta \quad (4.5a)$$

$$-mek_{TB}V_B = 2mE_C \left(-\frac{C_G V_G + Q_0}{e} - n + \frac{m}{2} \right) + q\Delta \quad (4.5b)$$

We will now consider the different possibilities for superconducting transport.

Quasiparticle (QP or e) transport charges the island by one electron ($m = 1$) and creates two

quasiparticles ($q = 2$).

Multiple Andreev reflection is another possibility for superconducting transport. We limit ourselves to the next two orders. A second order Andreev reflection (AR) transports two charges ($m = 2$), whereas three charges ($m = 3$) are transferred by multiple Andreev reflection. Both processes create two quasiparticles ($q = 2$).

In this picture, the supercurrent caused by the Josephson effect is the transport of single Cooper pairs. In this case two charges are transferred ($m = 2$) and no quasiparticles are created ($q = 0$). We will use the abbreviation J for this process.

Of course we should also consider the transport of excited quasiparticles. Here one electron is transferred ($m = 1$) but no additional quasiparticle is generated ($q = 0$). In the following we call this process singularity matching (SM), since it is most prominent if the energies of the singularities of the superconducting density of states match.

Plotting Eq. (4.4)-Eq. (4.5) in the gate-bias-plane for all processes described above and various island charges n creates a family of lines called transport diagram (see Fig. 4.3). We want to

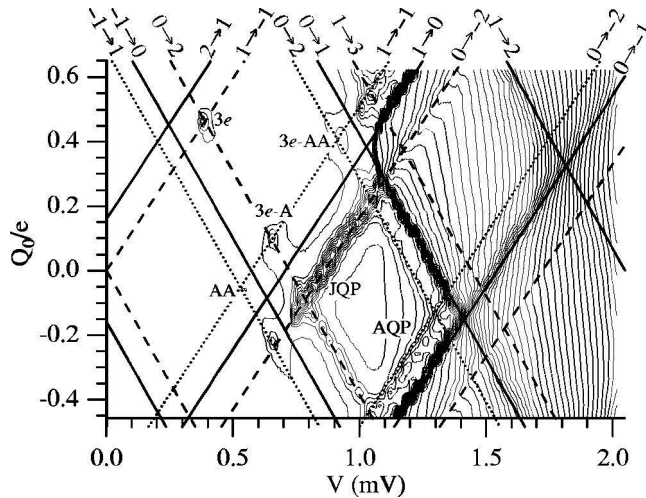


Figure 4.3: Transport diagram of a superconducting single electron transistor. The diagram overlays a contour plot of the current with respect to the bias voltage V and the gate charge Q_0 . Solid lines represent quasiparticle transport, dotted lines are Andreev reflections ($m = 2$) and dashed lines are the Cooper pair resonances. All lines are labeled with the initial and final charge states. Taken from [FPT98].

point out that the lines represent the *minimal energy* required for the transport. Thereby they show the *threshold* for the corresponding transport. The only exception concerns the transport of Cooper pairs. The Cooper pair line represents the *resonance condition* of the n and $n \pm 2$ state, therefore this transport is only possible along the line.

Please note, that only five parameters are required to draw the complete transport diagram. We usually use the charging energy E_C (respectively C_Σ), the superconducting gap Δ , the gate capacitance C_G , the offset charge Q_0 and the difference of the junction capacitances δC . When adjusting the transport diagram to the experimental data we use the more discernible parameters of positive and negative slope instead of E_C and δC (c.f. Eq. (4.6) and Eq. (4.7)).

We can determine the superconducting gap independently by measuring the unbroken sample.

The other parameters must be calculated for every configuration of the break junction by adjusting the transport diagram to the contour plot of the experimental data in the bias-gate-plane.

When evaluating the data, we typically identify characteristic current cycles which we know to follow specific lines. This allows to pinpoint the transport diagram partly and calculate all parameters. After all parameters are known we can complete the transport diagram using it to identify the other unknown current cycles.

As already mentioned, when analyzing the data most of the time it is easier to determine the slope of the lines instead of using the other parameters. The transport over the break junction is described by Eq. (4.5a) and Eq. (4.4b). Both follow the same negative slope

$$\left. \frac{dV_B}{dV_G} \right|_{BJ} = -2E_C \frac{C_G}{\kappa_{BJ} e^2} = -\frac{2C_G}{2C_{TB} + C_G + C_{GND}}. \quad (4.6)$$

This is only valid if the bias voltage is applied symmetrically and floating (c.f. Fig. 4.2).

For charging or discharging the island through the tunnel barrier, the slope is defined by

$$\left. \frac{dV_B}{dV_G} \right|_{TB} = 2E_C \frac{C_G}{\kappa_{TB} e^2} = \frac{2C_G}{2C_{BJ} + C_G + C_{GND}}. \quad (4.7)$$

Please note, that the slope only depends on the gate, the ground and the junction capacitances. The slope for transport over one junction is defined by the capacitance of the other junction.

4.2.3 Superconducting Current Cycles

Current through the SSET requires transport through both junctions. Using the different superconducting transport processes we compose possible current cycles as it is presented in [FPT98]. We always assume sequential transport through both junctions. Coherent transport through both junction at the same time is excluded. A detailed instruction on how to compose the current cycles is given in [Poh99]. The method is explained for the normal conducting SETs in Section 2.3.2 and can easily be extended to the superconducting case. We will summarize the main rules that must be obeyed.

First of all the cycle must be closed. If the initial charge state of a cycle is not restored in the final step, the cycle is not allowed to start again. This leads to a breakdown of the cycle and no current is flowing.

Second, the current cycle must be energetically possible. This is only the case if all participating transport processes are. One may use Eq. (4.4) and Eq. (4.5) to calculate the required bias energies.

There is a third aspect one has to take into account. All discussed transport possibilities besides the Josephson transport are dissipative. Therefore the lines represent thresholds.

The picture changes for Josephson transport, since this is a non-dissipative process. The Cooper pair line maps the evolvement of the superposition of the two involved charge states. At finite bias this superposition is destroyed as soon as a dissipative process can take place

changing the charge state of the island. Therefore we will always consider Josephson transport in combination with a dissipative quasiparticle transport. We will use the abbreviation $J - e$ for this combination.

The resonance condition for the Cooper pair transport has consequences for the current measured. All cycles featuring Josephson transport appear as a peak in current. The peak always follows the Cooper pair line.

All other current cycles will appear as onsets in the current.

For the calculation of the energies required for the different current cycles to take place, we will limit ourselves to $V_B > 0$ until the end of this section.

The Quasiparticle Onset ($e - e$ Onset)

The easiest current cycle is the quasiparticle onset or $e - e$ cycle. It consists of quasiparticle transport through both junctions and is a $n \rightarrow n \pm 1 \rightarrow n$ cycle.

Using Eq. (4.4) we obtain

$$eV_B = (\kappa_{BJ} + \kappa_{TB}) eV_B \geq 4\Delta. \quad (4.8)$$

The procedure of calculating the threshold voltage is concordant to the calculation for the normal conducting SET (c.f Section 2.3.2). Accordingly the threshold required reads as

$$4\Delta \leq eV_B \leq 4\Delta + 2E_C. \quad (4.9)$$

The JQP Cycle

The most extensively studied cycle featuring superconducting transport is the so called JQP cycle [Ave+97; Ful+89; NCT96; NST95; PFT00]. It consists of a $J - e$ transport followed by a second quasiparticle transition to restore the initial charge state. Therefore it is also a $n \rightarrow n \pm 1 \rightarrow n$ cycle. The cycle follows the Cooper pair resonance. Calculating the required energy similarly to the method used for the $e - e$ cycle we find that the quasiparticle restoring the state n requires the highest energies. Thus the processes starts for

$$eV_B \geq 2\Delta + E_C. \quad (4.10)$$

The JQP cycle can take place as long as the island remains in the initial charge state n . As soon as an additional quasiparticle can change the charge state to $n \mp 1$ (depending on the bias polarity) the initial state for the JQP is destroyed. If there is no possibility to restore the n state the JQP cycle gets poisoned and breaks down. The quasiparticles responsible for the poisoning requires an energy of

$$eV_B \geq 2\Delta + 3E_C. \quad (4.11)$$

The poisoning only affects the JQP for $3E_C < 2\Delta$, otherwise the breakdown point would be at energies higher than the quasiparticle onset. Inside the $e - e$ onset the initial charge state can be restored by quasiparticle tunneling. In this case the JQP can proceed up to rather large

bias values. With increasing bias the modulation of the quasiparticle current by the JQP cycle becomes weaker [NCT96; NST95].

The 3e Cycle

The $3e$ cycle forms another $n \rightarrow n \pm 1 \rightarrow n$ cycle. It is a combination of two $J - e$ processes, where one Cooper pair and one quasiparticle tunnel over both of the junctions [vdBri+91; vdBSG91; Had+98]. To observe the $3e$ cycle two energy conditions must be fulfilled:

$$eV_B = 2E_C \quad (4.12)$$

as well as

$$3E_C \geq 2\Delta, \quad (4.13)$$

since by allowing Josephson transport the transport of the corresponding quasiparticle must be possible as well [Had+98].

As the $3e$ process requires Josephson transport over both junctions it is always located at crossings of Cooper pair lines. Higher orders of the $3e$ cycle have been observed in SSETs [Had+98; Joy95] for small bias voltages. Those are examples for coherent transport through the SET and follow lines of different slopes. Therefore, they are easily distinguishable.

The AQP Cycle

Analogous to the JQP cycle we can compose the AQP cycle [FPT98]. This cycle is composed of a second order Andreev reflection and two quasiparticles. In contrast to the JQP cycle the AQP only features dissipative tunnel processes and thus appears as an onset. Thus, it is a $n \rightarrow n \pm 2 \rightarrow n \pm 1 \rightarrow n$ cycle. The threshold is given by

$$eV_B \geq 2\Delta + 3E_C. \quad (4.14)$$

The 3e-A Cycle

The $3e - A$ cycle is a composition of an Andreev reflection, a $J - e$ process and the transport of a single quasiparticle. One junction features the Andreev reflection and one quasiparticle, while the Cooper pair and the second quasiparticle are transported over the other junction. Hence, it changes the island charge states by $n \rightarrow n \pm 2 \rightarrow n \pm 1 \rightarrow n$. It is located at the crossing of an Andreev line and a Cooper pair line and requires the energy

$$eV_B \geq \Delta + 2E_C. \quad (4.15)$$

Comparably to the $3e$ cycle the condition $3E_C > 2\Delta$ must be fulfilled.

Further Andreev Cycles

All further Andreev cycles feature Andreev reflections over both junctions. The sample design presented in this thesis hosts two different tunnel junctions. Andreev reflection over the tunnel barrier will be very unlikely whereas they are enhanced over the BJ. Thus, we will only shortly introduce all cycles involving Andreev reflections over both junctions.

The $A - A$ cycle features Andreev reflections over both junctions and requires $eV_B \geq 2\Delta$. The $3e - AA$ cycle is a $n \rightarrow n \pm 2 \rightarrow n \pm 1 \rightarrow n$ cycle consisting of two Andreev reflections and two quasiparticle transports. The required bias energy is given by $eV_B \geq 2\Delta + E_C$.

The MARQP Cycle

If the break junction forms an atomic contact featuring mesoscopic transport, multiple Andreev reflections (MAR) of third order ($m = 3$) can contribute to the current. Analogous to the JQP and the AQP cycle we compose the MARQP changing the charge states by $n \rightarrow n \pm 3 \rightarrow n \pm 2 \rightarrow n \pm 1 \rightarrow n$. The energy required is given by [Lor18]

$$eV_B \geq 2E_C + \frac{8\Delta}{3}. \quad (4.16)$$

To observe the cycle this threshold must be smaller than the energy required for the quasiparticle onset. This leads to the requirement $3E_C < 2\Delta$.

4.2.4 Simulations Based on Orthodox Theory

Simulating the current of an SET always uses the Orthodox theory developed by Averin and Likharev in 1991 [AL91]. By now this is a standardized technique covered intensively in literature, e.g. [Poh99; Sch98; Tin04]. It is mainly based on calculating tunnel rates for all involved processes as basis for a master equation. The current is calculated by the stationary solution of the master equation.

Essential for calculating the rates is the change in the free energy of the system. We use the same definitions as already introduced in this chapter and reformulate the free energy of the SET (c.f. Eq. (2.14)) using the number of transported charges m .

$$F(n, m) = \frac{(C_G V_G + Q_0 - ne)^2}{2C_\Sigma} - \left[m + n \frac{\delta C}{C_\Sigma} \right] \frac{eV_B}{2}. \quad (4.17)$$

Of main interest is the change of the free energy δF when m charges are transported onto or off the island. This is given by

$$\delta F = F(n \pm m, m) - F(n, 0). \quad (4.18)$$

Since the simulation code used in this thesis has been written by Thomas Lorenz and is presented in his thesis [Lor18] we will give only a short overview.

First we need to define the overall rate connecting the states $n \rightarrow n \pm m$

$$\Gamma_{n \rightarrow n \pm m} = \Gamma_{\text{BJ}, n \rightarrow n \pm m} + \Gamma_{\text{TB}, n \rightarrow n \pm m}. \quad (4.19)$$

The stationary master equation

$$\sum_{m=-3}^3 P_n \Gamma_{n \rightarrow n+m} = \sum_{m=-3}^3 P_{n+m} \Gamma_{n+m \rightarrow n} \quad (4.20)$$

uses the probability P_n to find the island in the charge state n . This represents the stationary case assuming $dP_n/dt = 0$. Using the boundary condition

$$\sum_n P_n = 1 \quad (4.21)$$

this defines a linear system of equations, that can be solved numerically to obtain P_n . Using these results, the current is calculated using

$$\begin{aligned} I &= -e \sum_n P_n \sum_{m=1}^3 (\Gamma_{\text{BJ}, n \rightarrow n+m} - \Gamma_{\text{TB}, n \rightarrow n-m}) \\ &= -e \sum_n P_n \sum_{m=1}^3 (\Gamma_{\text{TB}, n \rightarrow n-m} - \Gamma_{\text{BJ}, n \rightarrow n+m}). \end{aligned} \quad (4.22)$$

We will now introduce how to calculate the rates for the participating processes.

The Quasiparticle Rate

We assume only single charge tunneling as transport. Following [Sch98] in the case of weak coupling, we can use Fermi's golden rule to calculate the tunnel rates. The quasiparticle rate Γ_{QP} can be expressed using the energy-dependent quasiparticle current $I_S(\delta F)$

$$\Gamma_{\text{QP}} = \frac{1}{e} \frac{I_S(\delta F)}{\exp[\delta F/k_B T] - 1}. \quad (4.23)$$

Using the BCS density of states for quasiparticles

$$N(\epsilon) = \Theta(|\epsilon| - \Delta) \frac{\epsilon}{\sqrt{\epsilon^2 - \Delta^2}} N(\epsilon) \quad (4.24)$$

and by assuming a constant normal conducting density of states $N(\epsilon) = N$ one obtains

$$I_S(\delta F) = \frac{1}{eR_N} \int d\epsilon \frac{\epsilon}{\sqrt{\epsilon^2 - \Delta^2}} \frac{\epsilon - \delta F}{\sqrt{(\epsilon - \delta F)^2 - \Delta^2}} [f(\epsilon) - f(\epsilon - \delta F)], \quad (4.25)$$

where $f(\epsilon)$ is the Fermi function $f(\epsilon) = \frac{1}{1 + \exp(\epsilon/k_B T)}$. The integration limits must be chosen respecting $|\epsilon| > \Delta$ and $|\epsilon - \delta F| > \Delta$. R_N describes the resistance of the junction in the normal conducting state.

The Cooper Pair Rate

Since Cooper pair transport is non-dissipative it is only possible to calculate a rate that links a Cooper pair transport with a dissipative process. For our simulations we use a rate that combines Cooper pairs and quasiparticle transport [AA90; AA89]

$$\Gamma_{J-e} = \frac{\Gamma_{QP} E_J^2}{4\delta F^2 + (\hbar\Gamma_{QP})^2}. \quad (4.26)$$

This results assumes low coupling ($E_J \ll E_C$) and vanishing temperature ($T = 0\text{K}$). For $T = 0\text{K}$ we can use the Ambegaokar-Baratoff relation [AB63] to calculate E_J for a tunnel barrier:

$$E_J = \frac{\hbar\Delta}{8e^2 R_N}. \quad (4.27)$$

Please note that this result depends on the normal conducting resistance R_N .

Depending on the configuration of the break junction, it can not be described as a tunnel barrier but rather as a weak link. This weak link is described by the Kulik-Omelyanchuk relation (see [Tin04]). Nevertheless, we will use Eq. (4.27) for both junctions in the simulations.

It has been shown that simulations using this rate are in good qualitative and quantitative agreement with experimental results obtained on SET samples made of two oxide tunnel barriers [NCT96; PFT00]. However, we want to point out that all of those results have been obtained on SETs featuring almost equal junction resistances.

The Andreev Reflection Rates

We use the quasiparticle rate to create an Andreev rate [Sie99] by introducing an arbitrary Andreev transmission τ_{AR} which can be chosen to match the experimental data.

$$\Gamma_{AR} = \tau_{AR} \Gamma_{QP}(2e) \quad (4.28)$$

The quasiparticle rate must respect the transport of two charges in calculating δF .

We use the same approach to calculate the rate for multiple Andreev reflection transporting $m = 3$ charges.

$$\Gamma_{MAR} = \tau_{MAR} \Gamma_{QP}(3e) \quad (4.29)$$

Chapter 5

Experimental Results

In this chapter, we will present the experimental results of the transport measurements of the SET samples. First, we will characterize the samples in the normal conducting state. The second part is dedicated to the results in the superconducting state for various regimes of the break junction. We will describe how the Coulomb blockade in the superconducting state varies, when the configuration of the break junction changes. Special focus will be laid onto the influence of asymmetric junction resistances for a fully opened break junction. For configurations of the break junction allowing for mesoscopic transport we will discuss the influence of multiple Andreev reflections. The chapter finishes with the results obtained for a break junction forming an atomic contact.

5.1 Characterization of SETs in the Normal Conducting State

In this chapter, we will first discuss how the charging energy and the resistance in normal conducting SETs are characterized. Afterwards, different samples are compared using the introduced characterization methods. Lastly we present a discussion of the development of the Coulomb blockade phenomenon when closing the break junction.

5.1.1 Calculating the Resistance of the NC SET

Since SETs show highly non linear IV characteristics calculating the resistance is not trivial. Besides, it is essential for the analysis (especially in the superconducting state) because the resistance is the main parameter to determine the state of the break junction.

The easiest idea is to use a single IV trace and perform a linear fit using only the data for high positive or negative bias, respectively. This idea is valid if the SET has similar junction resistances. Otherwise one observes a Coulomb staircase up to high bias voltages [IN92], as it is the case in our measurements. Due to the Coulomb staircase, the slope of the fitted linear function depends on the gate voltage and the limits used. To circumvent the problem we follow a concept presented in [FD87; HTT94]. The main idea is to rapidly vary the gate voltage with a high amplitude while the bias voltage is swept slowly. Using this method one effectively

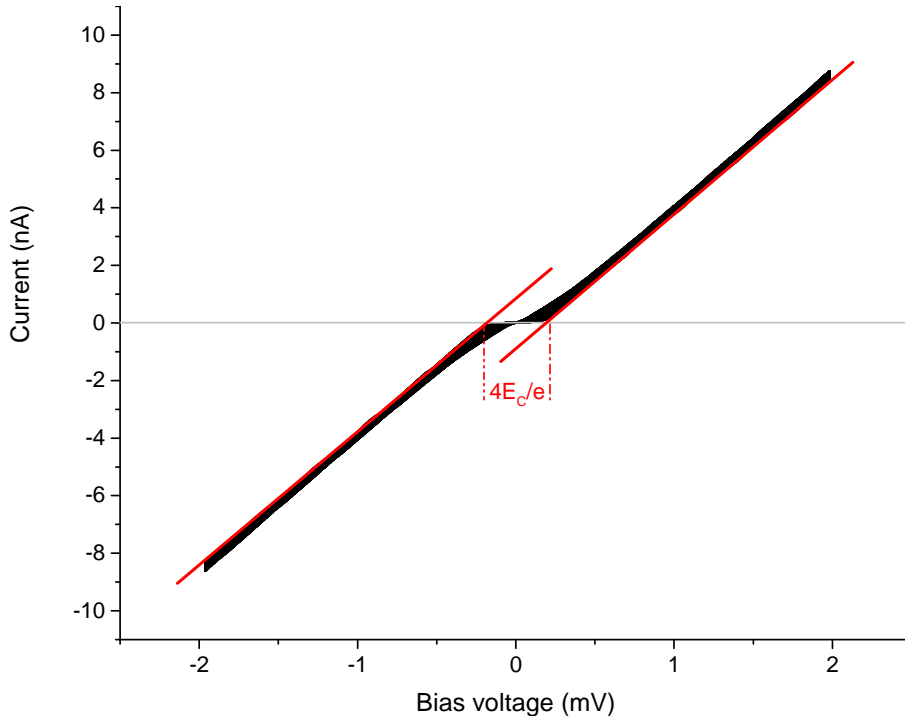


Figure 5.1: IV characteristics of a normal conducting SET. We display the IV characteristics for all gate voltages within one plot. This allows to adjust a straight line (red, solid) manually to the high bias region. Using the slope of the straights we calculate the resistance $R_\Sigma = 215\text{ k}\Omega$ of the sample. Extrapolating the straights to the zero current axis (black dash-dotted line) we calculate the charging energy. The axis intersect is equivalent to $4E_C$.

measures a complete gate-bias-map within one single IV characteristic obtaining the envelope of all possible IV characteristics.

This idea is equivalent to plotting the IV traces for all measured (constant) gate voltages within one figure as displayed in Fig. 5.1. We adjust a linear function to the envelope in the high bias regime as shown in Fig. 5.1. We want to emphasize that this is no fitting procedure, but a adjustment done by eye. Like an ohmic IV characteristic, the slope of the linear function comprises the resistance.

We use the mean value of the resistance determined for negative bias and the one for positive bias. The straights adjusted to the high bias regime contains even more information. Extrapolating to the zero current axis (black dash dotted line) the difference of the axis intersection is proportional to the charging energy.

Using the overall resistance, we calculate the resistance of the break junction by subtracting the resistance of the tunnel barrier. This requires a precise knowledge of the tunnel barrier's resistance. Before the break junction is broken, we can characterize the tunnel barrier solely. However, we observed indications for the tunnel barrier to change during the measurement. This change is most likely due to the mechanical movement of the sample.

We exemplify the change using sample 3: Measuring the unbroken sample we obtain $R_{TB} = 202\text{ k}\Omega$. After opening and closing the sample a few times, we closed the break junction completely and released all mechanical stress from the breaking mechanics. The resistance

measured now was only $R_{TB} = 194.5\text{ k}\Omega$. For a slightly higher resistance $R_\Sigma = 195\text{ k}\Omega$, we already observed charging effects yielding a charging energy of $E_C = 30\mu\text{eV}$. This resistance (R_Σ) is still lower than the initially determined resistance of the unbroken sample ($R_{TB} = 202\text{ k}\Omega$), indicating that the tunnel barrier is changed by the mechanical bending of the sample. We argue, that the aluminum film might contain intrinsic stress that is released after bending the sample for the first time.

Therefore, we take the smallest measurable resistance as a measure for the tunnel barrier resistance R_{TB} . We will use R_{TB} to calculate the break junction resistance from the measured total resistance R_Σ . Nonetheless, one should keep in mind that the break junction resistance may be prone to errors due to the aforementioned reasons.

5.1.2 Determination of the Charging Energy

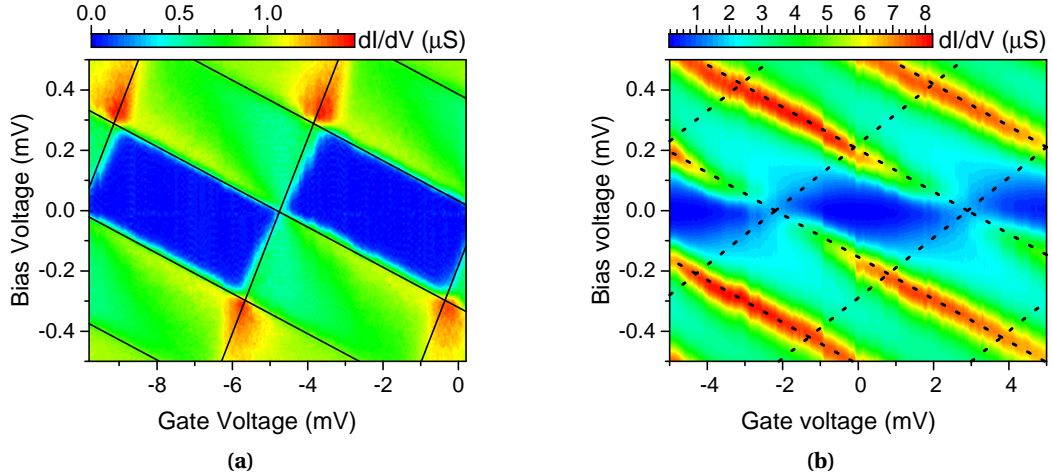


Figure 5.2: Differential conductance with respect to bias and gate voltage of a SET in the normal conducting state. Both measurements show data taken on sample 3 for various states of the break junction.

(a) The break junction is open ($R_{BJ} = 724\text{ k}\Omega$) and the resistance of the SET is $R_\Sigma = 919\text{ k}\Omega$. We observe a clear diamond structure that allows to extract the stability diagram (black lines). (b) If the break junction has a lower resistance ($R_{BJ} = 16\text{ k}\Omega$, $R_\Sigma = 211\text{ k}\Omega$) the areas where the transport is blocked are rounded. Thus, drawing the stability diagram is not obvious and the obtained parameters are less reliable. We added a dotted stability diagram as guide to the eye.

If the break junction is closed even further, the modulation of the blockade with the gate voltage vanishes. Obtaining the stability diagram becomes impossible.

As already explained, the easiest way to calculate the charging energy is the extrapolation of the high bias regime (c.f. Fig. 5.1). A second method is given by using the presentation of the current or the differential conductance in the bias-gate-plane. In Fig. 5.2 we show the differential conductance (dI/dV) of sample 3 with respect to bias and gate voltage for two different states of the BJ. If the break junction is opened and has sufficiently high resistances (Fig. 5.2a) we observe the diamond pattern of the Coulomb blockade. We can use the pattern to

draw the stability diagram (c.f. Section 2.3.2), obtaining the charging energy as one parameter. For lower resistances of the break junction (c.f. Fig. 5.2b) the diamonds at zero bias are washed out. Thus drawing the lines of the stability diagram is delicate. Nonetheless, we adjust the stability diagram to the experimental data as good as possible. Anyway, the parameters for this case are less reliable.

For the characterization of sample 3 we have used the linear fitting of the high bias regime and the stability diagram. Figure 5.3 compares the two results for all measured states of the break junction. We have extracted the stability diagram for all break junction configurations possible, i.e. for $R_\Sigma \geq 202 \text{ k}\Omega$. To calculate the uncertainty, we have evaluated the confidence interval of the bias axis intersect and the charging energy obtained from the stability diagram. We assume a uniform distribution inside the interval. Thus the statistical uncertainty σ is defined by the width of the interval b , $\sigma = b/2\sqrt{3}$.

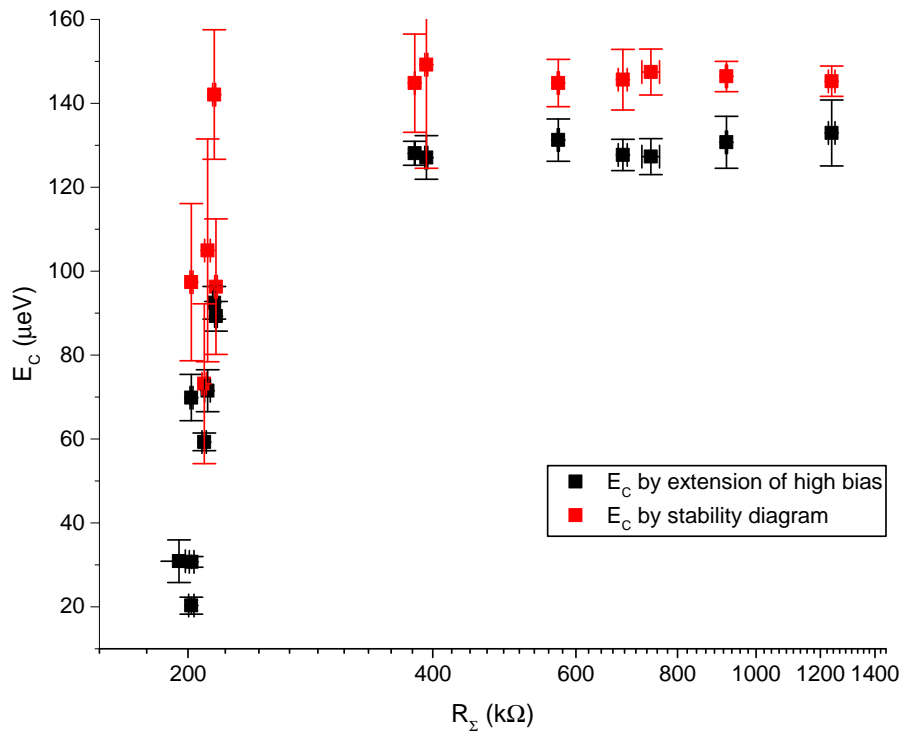


Figure 5.3: Comparison of methods for calculating the charging energy, exemplified on sample 3. The charging energy is extracted using the two methods explained in the text. The parameter extracted from the stability diagram (black) is systematically higher than the charging energy derived by the extrapolation of the high bias regime (red). The two methods yield charging energies which differ approximately $20\mu\text{eV}$.

The charging energy obtained from the stability diagram is systematically larger than the one obtained from the extrapolation of the high bias regime. The difference is around $20\mu\text{eV}$. Nonetheless we observe a decrease of the charging energy for decreasing break junction resistance for both evaluation methods. This renormalization of the charging energy is discussed in the next section.

5.1.3 Renormalization of the Charging Energy

In Fig. 5.4 we compare the charging energies of three samples with respect to the resistance of the break junction. We have used the extrapolation of the high bias regime to calculate the charging energy. This method allows to calculate the charging energy even for all resistances of the break junction.

The charging energies at high break junction resistance differ for all samples, indicating changes of the capacitances even though all samples have been produced following the same procedure. The main reason for changes in the capacitances are varying oxide thicknesses and overlap areas of the tunnel barrier. This assumption is supported by the fact that the tunnel barrier resistance was different for all samples. Sample 1 (black points) had an intermediate resistance $R_{\text{TB}} = 112 \text{ k}\Omega$, sample 2 (blue) offered a rather low resistance of $R_{\text{TB}} = 30 \text{ k}\Omega$ whereas the resistance of sample 3 (red) was the highest, $R_{\text{TB}} = 195 \text{ k}\Omega$.

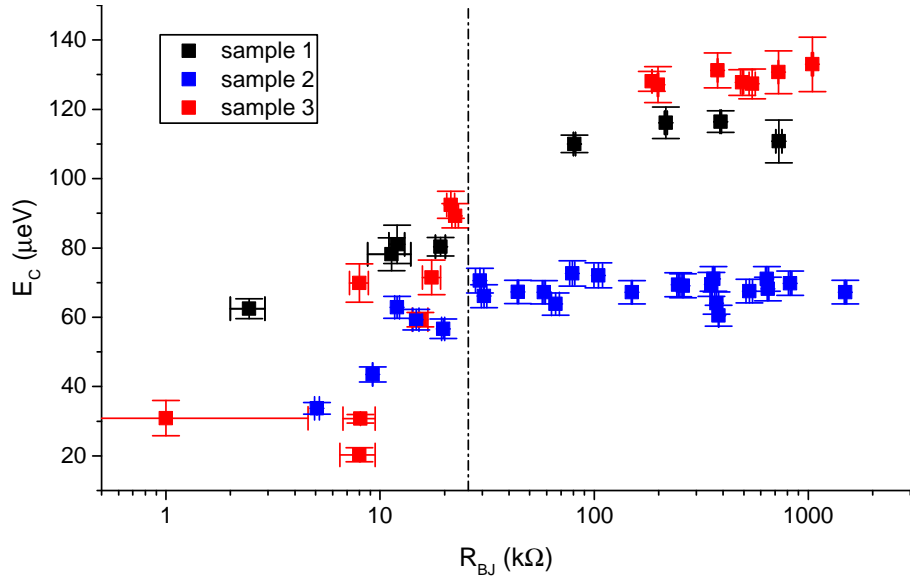


Figure 5.4: Comparison of the charging energy of three different samples. We have added a dash-dotted line at $R_K \approx 25.8 \text{ k}\Omega$ as guide to the eye. The charging energies of all samples are almost constant for high resistances of the break junction, $R_{\text{BJ}} > R_K$, although the absolute values differ. For lower resistances $R_{\text{BJ}} \leq R_K$ the charging energy decreases for decreasing break junction resistance. The resistances of the tunnel barriers are as follows: sample 1 (black) $R_{\text{TB}} = 112 \text{ k}\Omega$, sample 2 (blue) $R_{\text{TB}} = 30 \text{ k}\Omega$ and sample 3 (red) $R_{\text{TB}} = 195 \text{ k}\Omega$.

The charging energy is rather constant for all samples as long as the break junction resistance is larger than the Klitzing constant $R_{\text{BJ}} \geq R_K$. In Fig. 5.4 we have added a dash-dotted line at $R_K \approx 25.8 \text{ k}\Omega$ as guide to the eye.

For lower break junction resistances, the charging energy decreases while closing the break junction further. The decrease of the charging energy with decreasing junction resistance is called renormalization. It has been observed by Möller [Möl+98] in a SET defined in a two dimensional electron gas. In the article, the renormalization is described using the theory of Flensberg [Fle93], which we introduce in the next paragraph.

Assuming quantum fluctuations to be the reason for the renormalization, the theory predicts a scaling of the effective charging energy E_C^* depending on the number of conductance channels N connected to the island having the individual transmission τ_i . In this case one expects

$$E_C^* = E_C (1 - \tau_i)^N. \quad (5.1)$$

In our system we only vary the break junction. We are neither able to determine the number of conductance channels of the break junction nor their transmissions. Therefore, we simplify the model by assuming the break junction to have only one conductance channel ($i = 1$). For $R_B J \gg R_K$ this is well justified tunneling is usually described assuming only one channel. For single- or multi-atomic contacts $G \lesssim G_0$ often one channel dominates [Cha+07; Sch+97; Sen+18]. Thus we may easily calculate the transmission by using the conductance of the break junction (which is simply the reciprocal of the resistance) and Eq. (2.2). The scaling is then linear

$$\frac{E_C^*}{E_C} = 1 - \tau \quad (5.2)$$

In Fig. 5.5a we display the ratio E_C^*/E_C of sample 3 with respect to $(1 - \tau)$. Since we measured configurations of the break junction with resistances lower than $1/G_0 \approx 12.9 \text{ k}\Omega$ the parameter $(1 - \tau)$ may be negative.

We have added the scaling law as a red dash-dotted line. The scaling predicts $E_C^*/E_C = 0$ for $\tau = 1$, which is obviously not the case for our data. Anyway, for low resistances $0 \leq 1 - \tau \leq 0.4$ the reduced charging energy does not follow the prediction.

The magnification of the data obtained for high resistances $0.9 \leq 1 - \tau \leq 1$ is shown in Fig. 5.5b. Again we have added the scaling law in red. This time the data is scattered around the scaling showing a linear dependence.

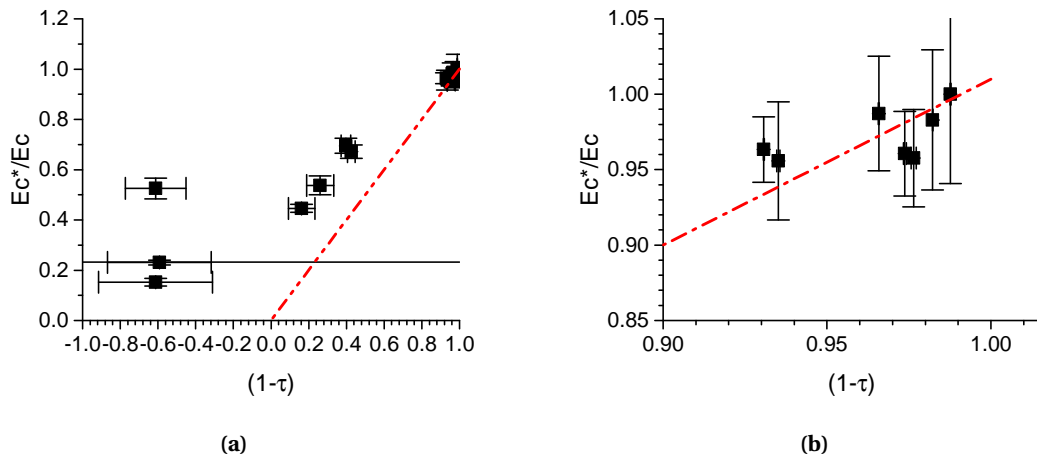


Figure 5.5: Renormalization of the charging energy of sample 3. We display the reduced parameter E_C^*/E_C (E_C^* being the effective charging energy according to Eq. (5.2)) with respect to the transmission τ of the break junction. We assume the break junction to have only one conductance channel. The charging energy decreases with increasing transmission. (a) The red line represents the linear scaling. Even though the charging energy decreases with increasing τ , the experimental data does not follow the scaling law. (b) Magnification of the data of low transmission. For low t the charging energy follows the scaling law (red).

Möller et al. report deviations from the linear scaling as well. For low resistances (and thus high transmission) ($1 - \tau \rightarrow 0$) they observed vanishing decrease of E_C^* / E_C with decreasing $(1 - \tau)$. The renormalization saturates at a value of $E_C^* / E_C \approx 0.45$. They argue that chaotic electron trajectories in the quantum dot (represented by the island) lead to a finite value of E_C^* / E_C for $\tau \rightarrow 1$ referring to a theoretical study done by Aleiner and Glazman [AG98]. However, this theory is only applicable to quantum dots having an intrinsic energy level spacing.

So far, the deviation of our experimental results from the scaling is not covered in literature. There are a few arguments one should consider:

If the break junction is completely opened, it forms a mere tunnel barrier. This barrier can be modeled as one conductance channel of very low transmission. That may be the reason why the data for high resistances follows the linear scaling (c.f. Fig. 5.5b).

As soon as the break junction forms an atomic contact the assumption of one conductance channel is not valid anymore. One-atom contacts made of aluminum are known to have three conductance channels of different transmission. Considering this, the scaling would not be linear any more.

One could also argue, that an aluminum break junction typically has one transmission channel that has the highest transmission whereas the other two channels have sufficiently lower transmissions and can therefore be excluded in an easy model. In this case the transmission we have calculated is too high since we have not subtracted the contribution of the two low transmitting channels. This overestimation of the transmission would shift all data points to the right in the representation in Fig. 5.5a. We argue, that the shifted data point would correspond better to the scaling law.

Nonetheless, the theory nicely describes the renormalization in the range of one conductance channel. We assume that the observed renormalization not covered by the linear scaling is still due to charge fluctuations. The observed deviation from the scaling law is caused by the contributions of more than one conductance channel. Similar to the experimental observation in [Möl+98] even for a transmission of 1, the charging effects do not completely vanish.

5.2 The SSET in the Framework of the Orthodox Theory

After evaluating the data obtained in the normal conducting state, we will now have a look on the behavior in the superconducting state.

In this section we will analyze the SSET using the Orthodox theory, which requires high junction resistances $R_i > R_K$. Since the resistances of the tunnel barrier is larger than $R_K \approx 25.8 \text{ k}\Omega$ for all samples presented in this thesis, mainly the configuration of the break junction determines whether this description is valid or not.

In this chapter we will focus on the transport diagrams for various samples and break junction configurations. We have always chosen those realizations, where the observed phenomenon is most prominent. Thus, we will switch between different samples. A complete characterization of sample 1 for all break junction configurations is presented in [Lor18].

In the last section we compare the charging energies in the superconducting state for sample 1 and sample 3.

In this section the parameters of the displayed stability or transport diagrams are absolute values without uncertainties. The diagrams are defined by the five parameters given and no other parameter set will lead to the very same pattern. Thus, it is not possible to give uncertainties for the diagrams. Whether the diagram matches the pattern observed in the data must be judged by eye.

5.2.1 The JQP Cycle

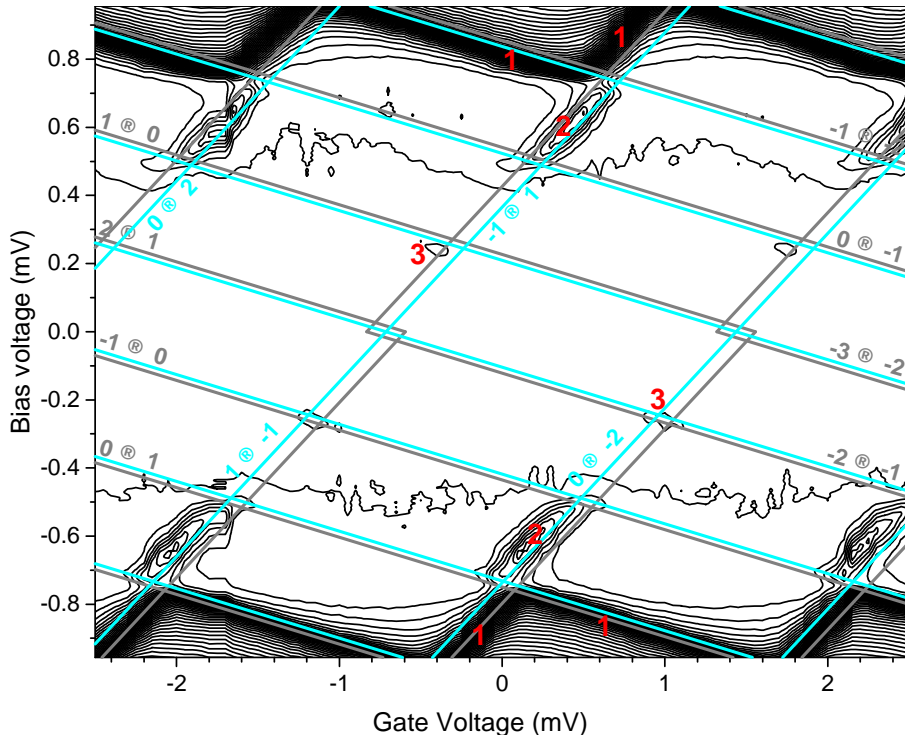


Figure 5.6: Contour plot of the current of a SSET with respect to gate and bias voltage. The contour interval is 15 pA. The break junction of sample 1 is fully opened. Thus the junction resistances are $R_{TB} = 112 \text{ k}\Omega$ and $R_{TB} = 723 \text{ k}\Omega$. We have added the transport diagram using $E_C = 122 \mu\text{eV}$, $\Delta = 190 \mu\text{eV}$, $C_G = 74.5 \text{ aF}$, $\delta C/C_\Sigma = -0.5568$ and $Q_0/e = 0.668$. The stability diagram features the lines for Josephson (cyan) and quasiparticle transport (gray). Each line is labeled by the initial and final charge state.

A fully opened break junction forms a mere tunnel barrier of high resistance. Thus the transport in this regime is determined by combinations of Cooper pair transport and quasiparticle tunneling. The most prominent cycle in this regime is the JQP cycle.

Figure 5.6 shows the typical current response of a SSET featuring Josephson transport. The break junction of sample 1 is fully open and has a resistance of $R_{BJ} = 723 \text{ k}\Omega$. We display a contour plot of the current with respect to gate and bias voltage. Additionally we have added the stability diagram using $E_C = 122 \mu\text{eV}$ and $\Delta = 190 \mu\text{eV}$. Cyan lines represent the resonance condition for Cooper pairs, while gray lines are thresholds for quasiparticle tunneling. Lines of positive slope correspond to transport over the tunnel barrier.

The quasiparticle onset (1) starts at $eV_B \geq 4\Delta$ and follows the threshold defined by the quasi-

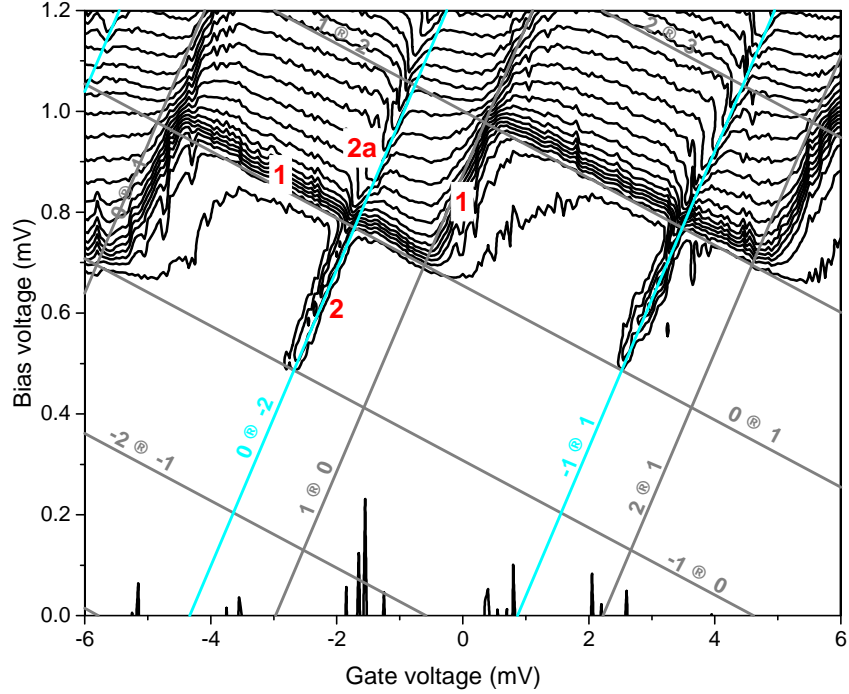


Figure 5.7: Contour plot of the current of sample 3 with respect to gate and bias voltage. Since the behavior of the SSET is symmetric with respect to the bias, we restrict ourselves to one bias polarity to obtain a better overview. The junction resistances are $R_{\text{TB}} = 195 \text{ k}\Omega$ and $R_{\text{BJ}} = 1.44 \text{ M}\Omega$. We have added the transport diagram using $E_C = 141 \mu\text{eV}$, $\Delta = 175 \mu\text{eV}$, $C_G = 30.8 \text{ aF}$, $\delta C/C_\Sigma = -0.6304$ and $Q_0/e = 0.836$. The Cooper pair line (cyan) and the quasiparticle line (gray) are labeled using their initial and final n value. The JQP cycle (2) is prolonged into the quasiparticle onset (1). The contour interval is 50 pA.

particle lines.

At $eV_B = 502 \mu\text{eV} = 2\Delta + E_C$ the JQP cycle (2) starts at the intersection of the Cooper pair line labeled by $n \rightarrow n \pm 2$ and the quasiparticle line labeled by $n \pm 1 \rightarrow n$. Since this sample fulfills the condition $3E_C < 2\Delta$, the JQP is poisoned at $eV_B = 2\Delta + 3E_C$, as explained in Section 4.2.3. This corresponds to the intersection of the aforementioned Cooper pair line with the quasiparticle line labeled by $n \rightarrow n \mp 1$. At this point the initial charge state for the JQP n is destroyed by a quasiparticle transition that changes the island's charge state to $n \mp 1$. Thus, the JQP breaks down.

Additional to the JQP cycle we observe a faint $3e$ cycle (3).

For samples offering $3E_C \geq 2\Delta$, the JQP does not break down at $eV_B = 2\Delta + 3E_C$. Here, the initial charge state n of the JQP cycle can be restored by one additional quasiparticle transition that changes the island's charge states to $n \mp 1 \rightarrow n$. This $e - e$ cycle $n \rightarrow n \mp 1 \rightarrow n$ is the quasiparticle onset.

In Fig. 5.7 we present the current response with respect to the bias and gate voltage of sample 3. Again the break junction is fully opened, $R_{\text{BJ}} = 1440 \text{ k}\Omega$. The charging energy of this sample is $E_C = 141 \mu\text{eV}$ whereas the superconducting gap is decreased to $\Delta = 175 \mu\text{eV}$. Thus, the condition for the breakdown of the JQP cycle (2) $3E_C < 2\Delta$ is not fulfilled. We observe a elongation of the JQP cycle (2a) into the quasiparticles onset (1).

Whether the JQP is observable in the quasiparticle onset does not only depend on the ratio of E_C and Δ , but also on the rates of the $e - e$ cycle and the JQP cycle.

Both cycles start at the same charge state n . Thus, the rate of the JQP must be larger than the rate of the $e - e$ cycle to observe the JQP cycle. According to the stability diagram (see Fig. 5.7), the Josephson transport takes place over the tunnel barrier. Since in both cases quasiparticles are transported over the break junction, the rates describing the transport over the tunnel barrier determine the behavior. According to Eq. (4.23) the quasiparticle rate for tunneling over the tunnel barrier scales as:

$$\Gamma_{\text{QP}} \propto \frac{1}{R_{\text{TB}}}. \quad (5.3)$$

The $J - e$ rate Eq. (4.26) behaves differently. Along the Cooper pair line the change of the free energy is zero, $\delta F = 0$. Thus, the rate scales as:

$$\Gamma_{J-e} = \frac{\Gamma_{\text{QP}} E_J^2}{(\hbar \Gamma_{\text{QP}})^2} \propto \frac{\frac{1}{R_{\text{TB}}} \left(\frac{1}{R_{\text{BJ}}} \right)^2}{\left(\frac{1}{R_{\text{TB}}} \right)^3} = \frac{1}{R_{\text{TB}}} \left(\frac{R_{\text{BJ}}}{R_{\text{TB}}} \right). \quad (5.4)$$

The rates only differ if the junction resistances are distinctly different. To observe the prolongation of the JQP cycle Γ_{J-e} must be much larger than Γ_{QP} . Since $R_{\text{BJ}} / R_{\text{TB}} \approx 7$ for this measurement, the JQP contributes to the current starting from the n state.

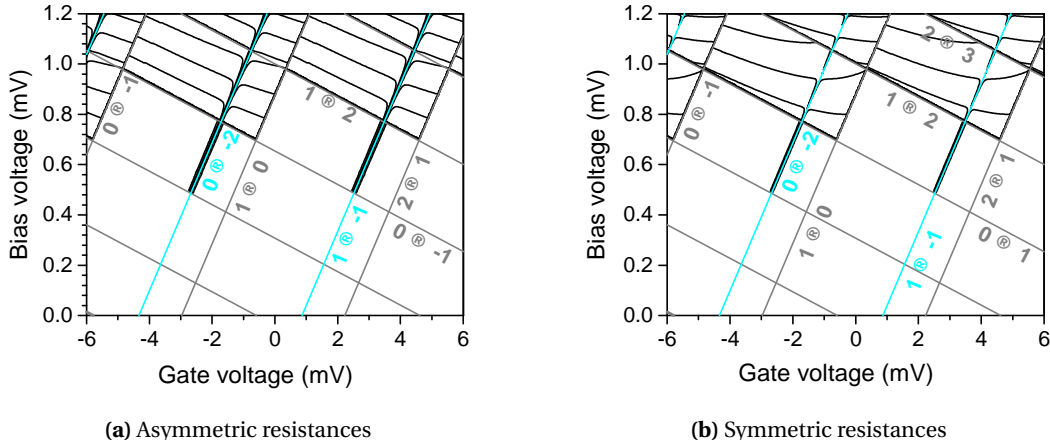


Figure 5.8: Simulations of the current of a SSET featuring asymmetric junction resistances. We have used the parameters given in Fig. 5.7. the contour interval for both simulations is 50 pA (a) The simulation uses the junction resistances as determined from the experiment ($R_{\text{TB}} = 195 \text{ k}\Omega$ and $R_{\text{BJ}} = 1.44 \text{ M}\Omega$). We observe an elongation of the JQP cycle into the quasiparticle onset. (b) If the total resistance $R_{\Sigma} = 1635 \text{ k}\Omega$ is distributed more equally ($R_{\text{TB}} = 545 \text{ k}\Omega$ and $R_{\text{BJ}} = 1.09 \text{ M}\Omega$) the elongation of the JQP fades away.

The need for distinctively different junction resistances to observe the elongation of the JQP cycle can be studied using simulated data. In Fig. 5.8 we present simulations using the parameters of the stability diagram of Fig. 5.7 and $T_{\text{sim}} = 0.3 \text{ K}$. On the left we have used the resistances as obtained from the experiment. Here, the JQP is clearly prolonged into the quasiparticle onset. On the right we show a simulation using the same overall resistance $R_{\Sigma} = 1635 \text{ k}\Omega$, but more equally distributed, i.e. $R_{\text{BJ}} = 1090 \text{ k}\Omega$ and $R_{\text{TB}} = 545 \text{ k}\Omega$. The asymmetry of

the resistance R_{BJ} / R_{TB} is reduced from 7 to 2. In this simulation the elongation of the JQP is only faint.

In the experiment the elongation of the JQP requires higher asymmetries. For $R_{BJ} / R_{TB} \approx 3.7$ ($R_{BJ} = 724\text{ k}\Omega$, $R_{TB} = 195\text{ k}\Omega$) the elongation of the JQP has almost vanished. Thus, the simulation predicts a elongation of the JQP even for lower junction asymmetries than observed in the experiment. Nonetheless, the asymmetry is vital for the elongation of the JQP cycle.

5.2.2 Bias Anomalies of the JQP Cycle

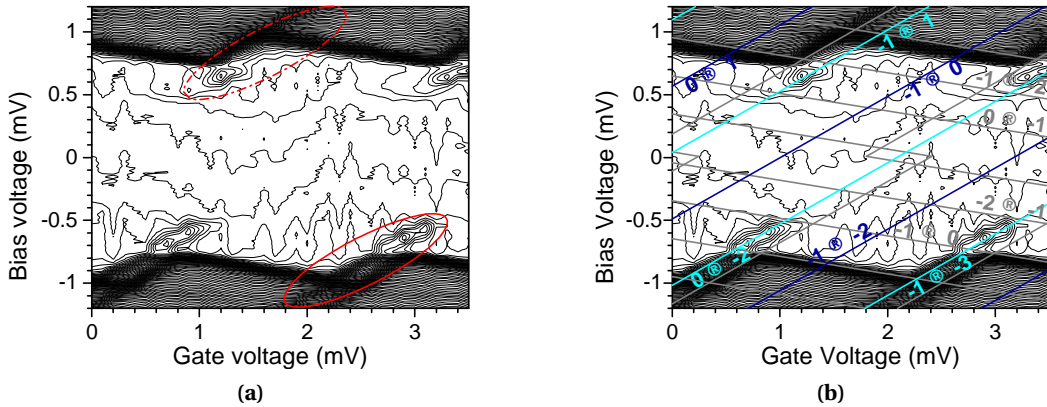


Figure 5.9: Contour plot of the current of sample 1 for very high break junction resistances $R_{BJ} = 2.4\text{ M}\Omega$. On the left hand side we display the experimental data. We observe a JQP cycle, that stops at $eV_B = 3E_C + 2\Delta \approx 740\mu\text{eV}$ for positive bias polarity (red circle). For negative bias voltages the JQP is prolonged into the quasiparticle onset (red dash-dotted circle). For clarity we display the same data with the stability diagram on the right hand side. Gray lines represent quasiparticles while the Cooper pair lines are shown in cyan. The blue lines mark the threshold for singularity matching. The stability diagram uses $\Delta = 193\mu\text{eV}$, $E_C = 118\mu\text{eV}$, $C_G = 74\text{ aF}$, $\delta C/C_\Sigma = -0.5544$ and $Q_0/e = 0.972$.

Following Orthodox theory we expect the JQP to break down at $eV_B = 3E_C + 2\Delta$ if $3E_C < 2\Delta$, as it is shown in Fig. 5.6. Nonetheless we observed a bias dependent elongation of the JQP cycle in sample 1 for high resistive configurations of the break junction.

The measurement presented in Fig. 5.9 was obtained for a high break junction resistance $R_{BJ} = 2.4\text{ M}\Omega$ while the resistance of the tunnel barrier was $R_{TB} = 112\text{ k}\Omega$. For clarity we present in the left panel (Fig. 5.9a) the current response of the sample. We have added the stability diagram in the right panel (Fig. 5.9b). Again, we have used gray for the quasiparticle lines and cyan for the Cooper pair lines while blue represents the singularity matching lines. The Josephson takes place over the tunnel barrier, while the break junction only allows for quasiparticle transport. For $V_B > 0$ and $T = 0\text{ K}$ the island is discharged ($n \rightarrow n - m$) through the break junction and charged ($n \rightarrow n + m$) through the tunnel barrier.

In the presented measurement we observe the breakdown of the JQP for the positive bias polarity (Fig. 5.9, red circle), but not for the negative bias polarity (Fig. 5.9, red dashed-dotted circle), where the JQP appears even beyond the quasiparticle onset.

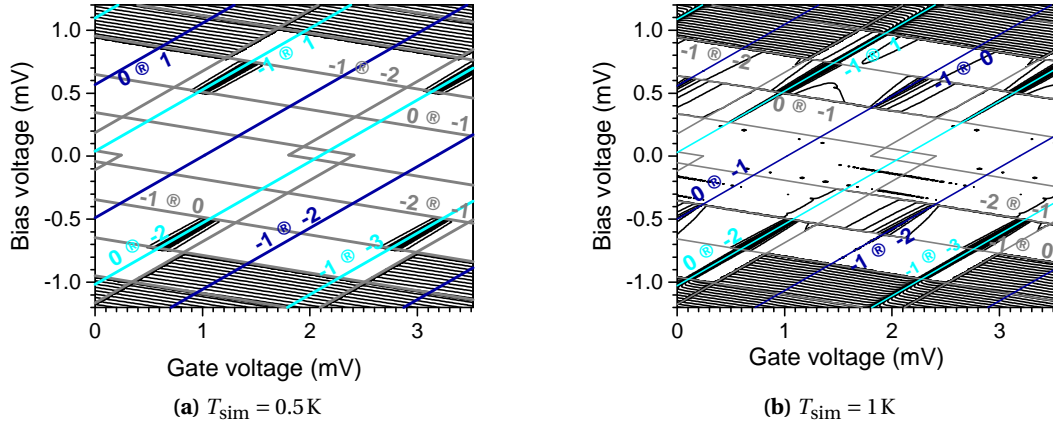


Figure 5.10: Simulated current of sample 1 using the parameters of the stability diagram displayed in Fig. 5.9 (a) Contour plot of the simulated current using $T_{\text{sim}} = 0.5 \text{ K}$. The JQP stops at $eV_B = 3E_C + 2\Delta$ and no elongation is observed. The contour interval is 10 pA. (b) Contour plot of the simulated current using $T_{\text{sim}} = 1 \text{ K}$. The enhanced temperatures create thermally excited quasiparticles, which leads to a symmetric elongation of the JQP for higher bias voltages. The contour interval is 7.8 pA.

Comparison of Simulated and Experimental Data

To clarify the origin of this behavior we used the master equation approach in the framework of the Orthodox theory for SSETs. We use the rates as explained in Section 4.2.4.

For the simulation we used the parameters extracted from the measurement (see Fig. 5.9). We only changed the break junction resistance for the simulation to $R_{\text{BJ}} = 2.2 \text{ M}\Omega$ to match the quasiparticle onset of the simulation to the experimental data. The gate capacitance is 74 aF and we calculated $\delta C/C_{\Sigma} = -0.5544$. In Fig. 5.10a we show the simulation using $T_{\text{sim}} = 0.5 \text{ K}$. Here, no elongation of the JQP is observed. Instead the JQP stops at $eV_B = 3E_C + 2\Delta$.

Figure 5.10b shows the simulated current using $T_{\text{sim}} = 1 \text{ K}$. Here the JQP is extended into the quasiparticle onset. We want to emphasize that the temperature in the simulation only affects the tunneling rates. It does not change the superconducting gap Δ , nor the Josephson energy E_J nor the charge states of the island. Only the Fermi function used for calculating the rates depends on the simulation temperature. Thus, the main effect of increasing the temperature is the creation of excited quasiparticles. To be precise the simulation temperature is also included in the Fermi function defining the probability for tunneling events for finite changes of the free energy $\delta F \leq 0$.

The only possibility to create excited quasiparticles in the simulation presented here is to use the quasiparticle rate and increase the temperature. This is the reason why we used such high temperatures in the simulation. Therefore, the simulation temperature is no measure for the electronic temperature in the experiment.

There are a few experimental parameters indicating the electronic temperature of the sample being lower than T_{sim} . Using the quasiparticle onset at $eV_B = 4\Delta = 772 \mu\text{eV}$ we find that the superconducting gap corresponds to the $T \approx 0 \text{ K}$ value. Following BCS-theory [Tin04] this limits the electronic temperature to $T \lesssim T_c/2 \lesssim 0.6 \text{ K}$. Besides we have tried to deliber-

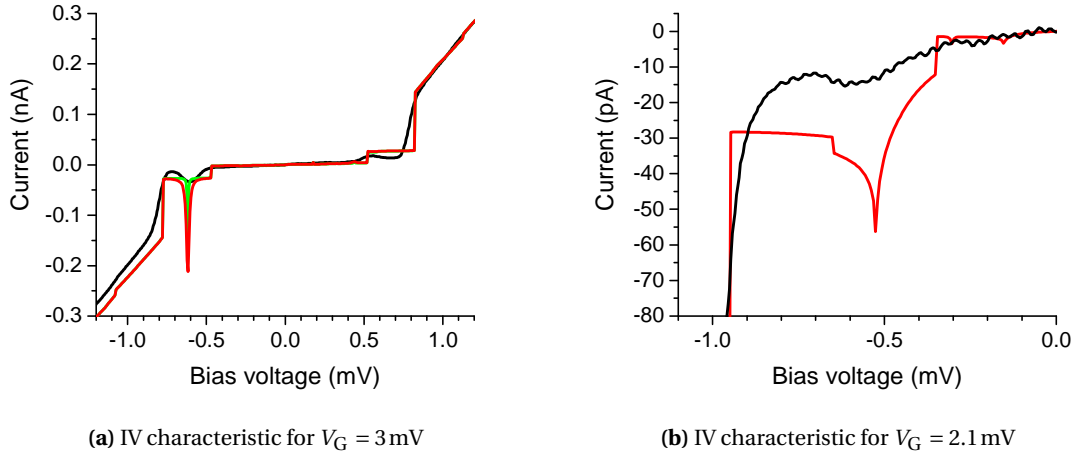


Figure 5.11: Comparison of simulated and experimental data. (a) Comparison of a single experimental IV characteristics (black) with the simulation for $V_G = 3$ mV. The JQP cycle is observable at $eV_B \approx 610\mu\text{eV}$. In red we present the simulation using the Ambegaokar-Baratoff value of the critical current $I_{c,TB} = 2.7\text{nA}$ to calculate E_J . Even though the simulation describes the overall shape of the experimental IV characteristic, the simulation overestimates the experimental observation. Using a lower critical current $I_{c,TB} = 0.65\text{nA}$ we obtain the simulation presented in green. (b) Comparison of a single experimental IV characteristics (black) with the simulation (red) for $V_G = 2.1$ mV. The current peak around $eV_B \approx 530\mu\text{eV}$ is caused by singularity matching and quasiparticle tunneling. It fits to the singularity matching line in Fig. 5.10b. The simulation resembles the IV characteristic qualitatively but overestimates the current of the singularity matching cycle.

ately create thermally excited quasiparticles by heating the dilution system. Temperatures of $T > 0.6\text{K}$ were required before additional processes were observed. Due to restrictions of the measurement setup we are not able to access the electronic temperature directly. Nonetheless, these observations indicate a sufficiently cold electronic system with $T \leq 0.6\text{K}$. Excited quasiparticles of varying or unknown origins are known to contribute to the current even for low temperatures [Cou+08; KMP12; Raj+08; Ser+18].

Before we discuss the processes leading to the elongation of the JQP cycle we would like to compare the simulated and the experimental data in more detail.

Figure 5.11a shows the comparison of a single experimental IV characteristic (black) to the simulation (red) for $V_G = 3$ mV, where a JQP for negative bias voltages is observed. The simulation overestimates the contribution of the JQP ($I_{JQP} \approx 210\text{ pA}$) in comparison to the measurement ($I_{JQP} \approx 45\text{ pA}$) by more than a factor of 4, which is in contrast to literature [NCT96; PFT00]. We assign this discrepancy to the use of the Ambegaokar-Baratoff relation [AB63] to calculate the critical current, which gives us $I_{c,TB} = 2.7\text{nA}$ for the tunnel barrier.

In our sample design we are able to measure the critical current of the tunnel barrier independently by fully closing the break junction, which leads to $I_{c,TB} = 29\text{ pA}$. The RCSJ model predicts that the measured value depends on the measurement circuit, which in our case is not optimized for measuring critical currents. Nonetheless we take this as an indication that the Ambegaokar-Baratoff value does not properly describe our junction.

Taking this reasons for possible deviations from the Ambegaokar-Baratoff relations into ac-

count, we use E_J as an adjustable parameter. Using $I_{c,TB} = 0.65 \text{ nA}$ to calculate E_J we obtain the IV characteristic drawn in green in Fig. 5.11a. Still, the simulation overestimates the current carried by the JQP cycle, $I_{\text{JQP}} \approx 100 \text{ pA}$. Additionally, the simulated JQP is much narrower than the experimentally measured one. This matches to the observation of Pohlen et al. [PFT00]. They have studied the simulation of the JQP cycle in comparison to experimental data for various samples. Even though the absolute current height of the simulated data matched the experimental values quite well, the full width at half maximum (FWHM) did not. They report a tendency of increasing $I_{\text{data}}^{\text{FWHM}} / I_{\text{sim}}^{\text{FWHM}}$ with increasing resistance R_Σ of the sample. The highest resistance evaluated was $R_\Sigma = 250 \text{ k}\Omega$ offering $I_{\text{data}}^{\text{FWHM}} / I_{\text{sim}}^{\text{FWHM}} = 2.1$. Since the resistances of the measurement presented in this section are much higher ($R_\Sigma = 2.5 \text{ M}\Omega$) we also expect a higher discrepancy of the simulated and experimentally measured width.

Using the simulations presented in Fig. 5.11a we obtain $I_{\text{data}}^{\text{FWHM}} / I_{\text{sim}}^{\text{FWHM}} = 4.9$ and $I_{\text{data}}^{\text{max}} / I_{\text{sim}}^{\text{max}} = 0.1$ by using the Ambegaokar-Baratoff value and $I_{\text{data}}^{\text{FWHM}} / I_{\text{sim}}^{\text{FWHM}} = 6$ and $I_{\text{data}}^{\text{max}} / I_{\text{sim}}^{\text{max}} = 0.3$ if we use $I_{c,TB} = 0.65 \text{ nA}$.

To match the current height of the simulated data to the experiment ($I_{\text{data}}^{\text{max}} / I_{\text{sim}}^{\text{max}} = 1$), a critical current of $I_{c,TB} = 315 \text{ pA}$ is required. On the other hand the simulated width deviates even more from the experimental value, $I_{\text{data}}^{\text{FWHM}} / I_{\text{sim}}^{\text{FWHM}} = 7.6$. Thus, using the critical current of the tunnel barrier as a fitting parameter in the simulation is not possible. Obviously the simulation does not cover all effects broadening the JQP cycle. Thus, we will use the Ambegaokar-Baratoff relation for the critical current to calculate E_J in all further simulations.

Nonetheless, the simulation presented in Fig. 5.10b allows to explain the elongation of the JQP: The JQP cycle $n \rightarrow n \pm 1 \rightarrow n$ breaks down as soon as one additional quasiparticle can tunnel through the break junction and change the charge state to $n \rightarrow n \mp 1$. If there is an excited quasiparticle available, it can tunnel through the tunnel barrier and restore the n state ($n \mp 1 \rightarrow n$). This composes a quasiparticle-singularity matching (SM-e) cycle requiring an energy of $eV_B \geq 4\Delta$. We observe this SM-e cycle (see Fig. 5.11b) in both the experimental data and the simulation.

Thus, there are two competing cycles starting from the n state along the Cooper pair line. As explained in Section 5.2.1 shown using Eq. (5.3) and Eq. (5.4), the observability of the JQP depends on the rates of the JQP cycle and the competing cycle. In the measurement presented the ratio of the resistances is $R_{BJ} / R_{TB} \approx 20$. Thus, the JQP dominates the current starting from the n state.

Similar to the previous arguments, the elongation of the JQP cycle vanishes if we simulate with the same overall resistance but more equally distributed between the two junctions. Using $T_{\text{sim}} = 1 \text{ K}$ the elongation vanishes for $R_{BJ} / R_{TB} = 3$. The lower the temperature the faster the elongation vanishes. Thus, $R_{BJ} / R_{TB} = 13$ is already enough to suppress the elongation for $T_{\text{sim}} = 0.7 \text{ K}$.

In the experiment we observe the elongation for $R_{BJ} / R_{TB} \approx 16.9$, but it is not observable for $R_{BJ} / R_{TB} \approx 6.4$. Unfortunately we were not able to measure for intermediate rates, since it is challenging to keep the break junction stable for the resistances required.

Including Non-equilibrium Effects into the Orthodox Theory

So far, the model nicely explains the origin of the elongation, but it does not cover the observed bias asymmetry. In fact, within the used model only the current direction and not the electrostatic behavior of the SSET changes with the bias polarity. This explains why the elongation is present in both bias polarities of the simulation which is in conflict with the experimental observation. Therefore we have refined the model.

The asymmetry can be explained assuming a relaxation of quasiparticles which is slower than the tunneling time for an excited quasiparticle. To implement this in the simulation we assume that a fraction of transferred quasiparticles resides on the island as excited quasiparticles, which then may be transported off the island using a singularity matching process.

We solve the Master equation to get the probability vector $\vec{P}(n)$ as done for the simulation presented before. Rather than calculating the current using $\vec{P}(n)$ and the rates of one junction, we employ the rates of both junctions to determine how many net quasiparticles are transferred onto the island. Here, the number of net quasiparticles denotes the difference of QP tunneling onto the island minus the amount of quasiparticles tunneling off the island. We do not consider over which junction the transport took place.

Multipled by an experimental parameter k this defines the creation rate

$$\Gamma_{\text{create}} = k \max \left(\sum_n \vec{P}(n) (\Gamma_{n \rightarrow n \pm 1} - \Gamma_{n \pm 1 \rightarrow n}), 0 \right) \quad (5.5)$$

of excited quasiparticles, if the number of net quasiparticle is positive. Using this approach, we expect $0 \leq k \leq 1$. For the transport of the excited quasiparticles we assume a normal conducting tunnel rate for ohmic contacts Γ_R [Sch98].

$$\Gamma_R = \frac{1}{R_{NCE} e^2} \frac{-\delta F}{1 - \exp \left(\frac{\delta F}{k_B T} \right)} \quad (5.6)$$

Included in this simplified assumption of normal conducting ohmic transport is a constant density of states (DOS) on both sides of the tunnel contact. To obtain the rate for excited quasiparticles we combine Γ_{create} with the tunnel rate for ohmic contacts using

$$\Gamma_{\text{SM}} = \left(\frac{1}{\Gamma_{\text{create}}} + \frac{1}{\Gamma_R} \right)^{-1}. \quad (5.7)$$

Adding the new rate Γ_{SM} to Γ_{QP} , we recalculate the rate for the JQP Γ_{J-e} using equation Eq. (4.26), solve the master equation again and calculate the current.

Using this approach, the simulation yields results as presented in Fig. 5.12, which reproduces our experimental data qualitatively. Neglecting the fast relaxation approach leads to bias asymmetries in the simulation. In the negative bias we note two distinct differences. On the one hand the JQP is much more pronounced (c.f. Fig. 5.12, α), on the other hand the elongation and the modulation of the quasiparticle onset can be seen only there (Fig. 5.12, β). Those observation can be explained by having a closer look onto the transport processes charging and discharging the island for both bias polarities.

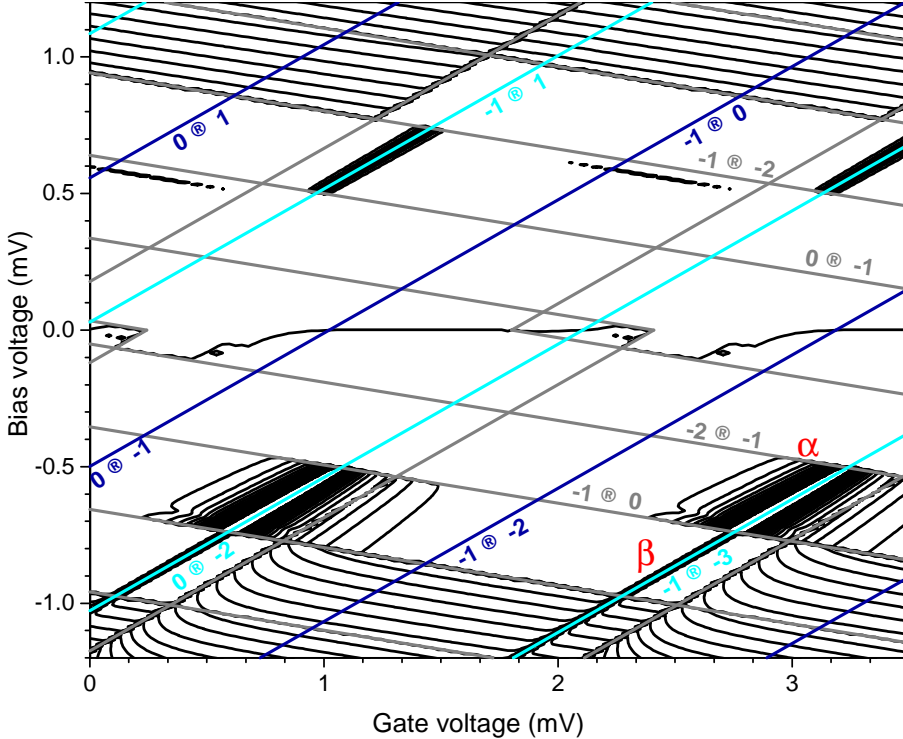


Figure 5.12: Contour plot of the simulated current versus gate and bias voltage using the approach of slow relaxation of excited quasiparticles. Again we added the lines for clarity. The simulation uses the parameters as defined before and $k = 50$. We have changed the temperature used in the simulation to $T = 0.5\text{ K}$. The new approach leads to bias asymmetries of the JQP cycle. For $V_B > 0$ the JQP cycles stops at $eV = 2\Delta + 3E_C = 740\mu\text{eV}$, whereas for $V_B < 0$ the JQP cycle is broadened (α) and extended into the quasiparticle onset (β). The broadening is due to non-physical assumptions of the simulation (as explained in the text).

For $V_B < 0$ the JQP transports quasiparticles onto the island. This increases the number of excited quasiparticles which leads to enhanced probabilities for SM-e cycles (i.e. cycles involving quasiparticle transport and singularity matching), either $n - 1 \rightarrow n - 2 \rightarrow n - 1$ or $n \rightarrow n - 1 \rightarrow n$ (c.f. labels of SM lines (dark blue) in Fig. 5.12). The increased current and broadening of the JQP in the simulation results from the addition of the regular JQP and the SM-e cycles.

We do not expect this model to completely match our experimental results, because we used a normal conducting ohmic tunnel rate to create the rate for the additional excited quasiparticles. Since the used tunnel rate implies a constant DOS for all transport voltages on both sides of the break junction, it will underestimate the contribution of the excited quasiparticles for small transport voltages. In the experiment the sample is still in the superconducting state. Thus, the contribution is largest if the singularities of the superconducting DOS are aligned, which is the case at the SM line (meaning small transport voltages). The contribution decreases with increasing transport voltages, following the curvature of the superconducting DOS. Again, this in contrast to the model used for the simulation. Here, the contribution of the excited quasiparticles increases with increasing transport voltages. We want to emphasize that the tunnel rates are the only parameters of the simulation where the superconducting DOS enters.

The discussion in the paragraph above provides an argument, why k is larger than one in the simulation presented. Choosing $k = 50$ creates an artificial increase of Γ_{SM} for small transport voltages. Additionally Γ_{create} is not recalculated after the transport of an excited quasiparticle. Easy speaking this allows one excited quasiparticle to be the source of several charges transported.

We can also explain the elongation of the JQP in the negative bias with the cycles involved. In the negative bias poisoning the JQP happens by an additional electron tunneling onto the island, thus increasing the excited quasiparticle density. This excited quasiparticle provides the possibility to change the $n + 1$ state back to n by a singularity matching as explained before. Therefore, the JQP may continue. In the positive bias the poisoning of the n state happens by a quasiparticle tunneling off the island, changing the charge state to $n - 1$. In our model this does not lead to a change of the number of excited quasiparticles on the island, thus the charge state is fixed and the JQP breaks down.

Within this model the complete lack of the elongation of the JQP in the positive bias can be explained qualitatively. We want to point out, that the simulation presented in Fig. 5.12 does use lower temperatures ($T_{\text{sim}} = 0.5 \text{ K}$ and $k = 50$) than the simulation presented in Fig. 5.10b. The new model offers an additional source of excited quasiparticles, which makes the high simulation temperatures used in Fig. 5.10b redundant. Again this gives reason to estimate the electronic temperature of our sample to be $T \leq 0.6 \text{ K}$.

5.3 Mesoscopic Superconductivity in the SSET

In the previous chapter we have examined the behavior of SSET having high break junction resistances $R_{\text{BJ}} > 700 \text{ k}\Omega$. Featuring this high resistances the coupling through the break junction is small and only quasiparticle tunneling can happen. All other transport processes like Josephson transport take place over the tunnel barrier.

By closing the break junction we increase the coupling. Thus, Josephson transport over the break junction gets stronger leading to the observation of a JQP over the break junction as well. The lower the break junction resistance gets, the more prominent the JQP becomes.

Closing the break junction even further to $50 \text{ k}\Omega \leq R_{\text{BJ}} \leq 80 \text{ k}\Omega$, we enter the mesoscopic regime of the Orthodox theory where contributions of (multiple) Andreev reflections are observed. Here, the coupling through the break junction allows for mesoscopic transport, while the Coulomb blockade is still fully observable. We may use the aforementioned extension of the Orthodox theory that incorporates Andreev reflections (Section 4.2.2, Section 4.2.4).

We want to point out, that some of the results of this section have already been presented in [LSS18; Lor18]. Nonetheless, we reiterate it here, since the results are necessary to understand the next chapter.

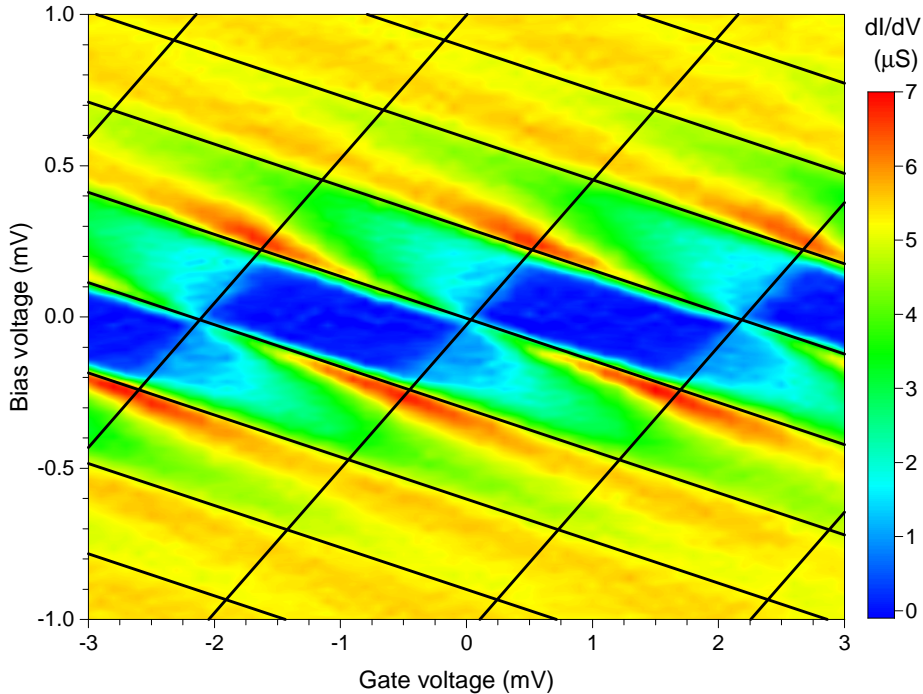


Figure 5.13: Normal conducting conductance of sample 1 for $R_{\text{TB}} = 112 \text{ k}\Omega$ and $R_{\text{BJ}} = 75 \text{ k}\Omega$. We still observe the Coulomb diamonds for small bias voltages even though the positive slope is slightly washed out. Towards higher bias voltages only the negative slope is clearly distinguishable. Thus, the Coulomb staircase is determined by tunneling through the break junction. We have adjusted the stability diagram using $E_C = 116 \mu\text{eV}$, $\delta C/C_\Sigma = -0.5484$, $C_G = 74.5 \text{ aF}$ and $Q_0/e = 0.516$.

5.3.1 Analysis of the Normal Conducting State

To proof the observability of the Coulomb blockade we will first have a look on the behavior in the normal conducting state. In Fig. 5.13 we present a measurement on sample 1 obtained for a break junction resistance of $R_{\text{BJ}} = 75 \text{ k}\Omega$. For low bias voltages the blockade of transport still follows the well-known diamond structure. For higher bias voltages we observe a Coulomb staircase, which is mainly determined by tunneling through the break junction. Thus, the negative slope of the diamonds is well identifiable. The positive slope of the Coulomb diamonds is slightly washed out in comparison to Fig. 5.2a where $R_{\text{BJ}} = 724 \text{ k}\Omega$.

Nonetheless we may still use the periodicity along the gate axis to determine the gate capacitance $C_G = 74.5 \text{ aF}$ and the offset charge $Q_0/e = 0.619$. To obtain the other parameters we have adjusted the stability diagram as good as possible. We want to point out, that we do not do any fitting procedure. Instead we try to adjust the stability diagram in such a way, that it visibly resembles the pattern of the experimental data as good as possible. We do not have an analytical parameter qualifying the agreement but rather judge by eye.

Using this procedure we obtain the stability diagram as shown in Fig. 5.13. The diagram uses $E_C = 116 \mu\text{eV}$ and $\delta C/C_\Sigma = -0.5484$. This is similar to the parameters used to draw the stability diagram for the same sample and a fully opened break junction (c.f. Fig. 5.6).

All parameters given here represent the parameters used to draw the diagram. Therefore they are accurate for this diagram and we can not define uncertainties. Since we adjust the diagram

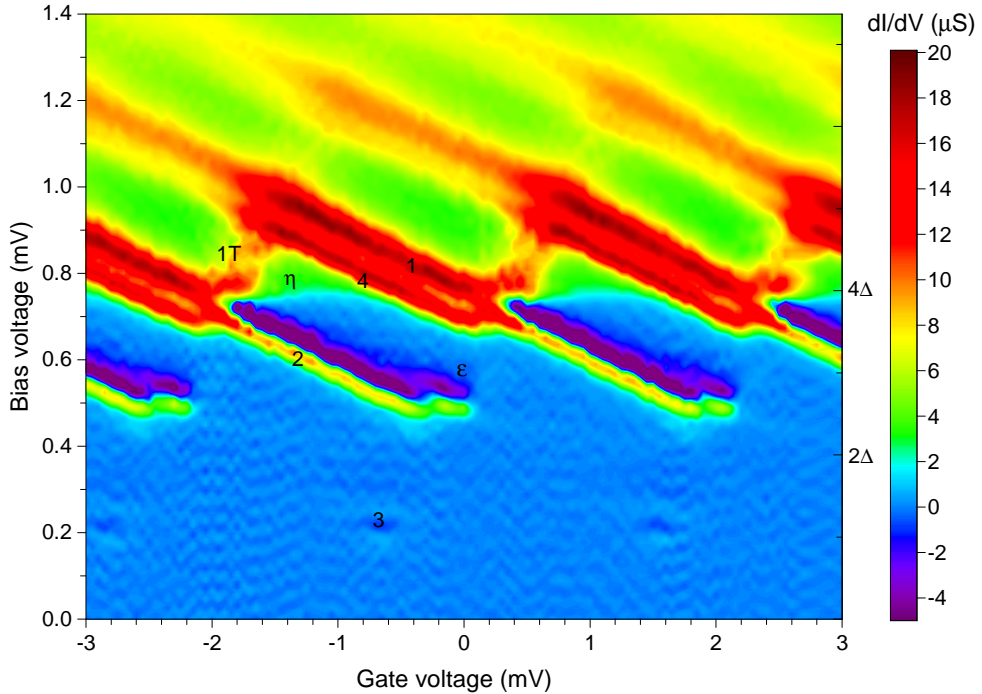


Figure 5.14: Superconducting conductance of a SSET featuring $R_{\text{TB}} = 112\text{k}\Omega$ and $R_{\text{BJ}} = 75\text{k}\Omega$. The transport over the break junction dominates the behavior of the SSET. Thus, almost all of the observed current cycles follow the negative slope. We discuss the marked cycles in the text.

by hand we can not define a statistical deviation of the parameters. From experience and considering the step width of the gate voltage (0.05 mV) we can determine the gate capacitance up to 5% accuracy.

5.3.2 Characterization of the Superconducting State

For resistances $R_{\text{TB}} = 112\text{k}\Omega$ and $R_{\text{BJ}} = 75\text{k}\Omega$, the current in the quasiparticle onset is already in the range of 5nA , while the small current cycles in the gaps are rather small ($\sim 20\text{pA}$). To resolve all cycles within one representation we will from now on display the differential conductance instead of the current with respect to the bias and gate voltages.

Thus, all peak like structures in the current will be apparent in the conductance as a combination of a local maximum followed by a local minimum of negative conductance. Onsets will show up as a single peak-like structure in the conductance. To adjust the transport diagram we will place the lines of the diagram to match either the maximum (for onsets in the current) or the area of zero conductance in between the maximum-minimum structure (for peaks in the current).

In Fig. 5.14 we display the experimental data for $V_B > 0$ obtained in the superconducting state. There are several differences in comparison to the results obtained for high break junction resistances as presented in Fig. 5.2a.

Around the quasiparticle onset over the break junction we observe two onsets next to each

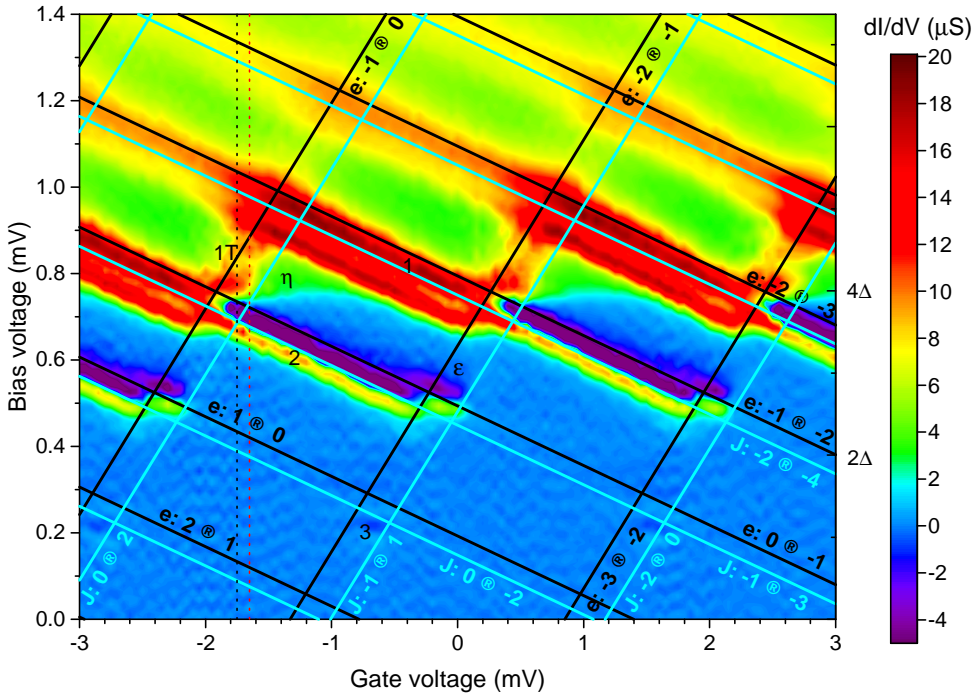


Figure 5.15: Presentation of the conductance as in Fig. 5.14 featuring the transport diagram using the Cooper pair (cyan) and the quasiparticle (black) lines. The diagram uses $\Delta = 192\mu\text{eV}$, $E_C = 116\mu\text{eV}$, $\delta C/C_\Sigma = -0.5484$, $C_G = 74.5\text{aF}$ and $Q_0/e = 0.527$. The JQP cycle (2) follows the Cooper pair line describing transport over the break junction (negative slope). The quasiparticle lines describe the quasiparticle onset rather well. We assume cotunneling to be the reason for the enhanced conductance (η) at $eV_B \geq 4\Delta$, since it is not modulated by the gate voltage. Additionally we observe a small $3e$ cycle (3) at the crossing of two Cooper pair lines.

The vertical lines mark the gate voltages of which we show the IV characteristics in Fig. 5.16.

other (1, 4). The quasiparticle onset over the tunnel barrier is broadened (1T).

Inside the superconducting gap $eV_B < 4\Delta$ we observe a peak like feature (2). Next to it an additional small peak is positioned (ϵ). At $eV_B = 4\Delta$ we observe an enhanced conductance (η). Deep inside the superconducting gap there is a small current contribution (3).

All cycles besides (ϵ) are covered by the Orthodox theory including Andreev reflections. We will use the transport diagram to identify them. For reasons of clarity we will not draw the stability diagram featuring the lines of all possible transport processes at the same time but rather take a step-by-step approach.

We start the analysis by adjusting the Cooper pair and the quasiparticles lines using the charging energy obtained in the normal conducting state ($E_C = 116\mu\text{eV}$). The Cooper pair lines need to match the JQP cycle (2), that starts at $eV_B = 2\Delta + E_C \approx 500\mu\text{eV}$. Here, the Cooper pairs tunnel over the break junction, while the quasiparticles are transported over the tunnel barrier. Figure 5.15 shows the measured conductance and the transport diagram of the Josephson and quasiparticle transport. We use $\Delta = 192\mu\text{eV}$, $E_C = 116\mu\text{eV}$, $\delta C/C_\Sigma = -0.5484$, $C_G = 74.5\text{aF}$ and $Q_0/e = 0.527$.

Since the resistance of the break junction is low, the JQP creates high currents overcoming the critical current of the break junction. This leads to a jump of the current and the voltage until

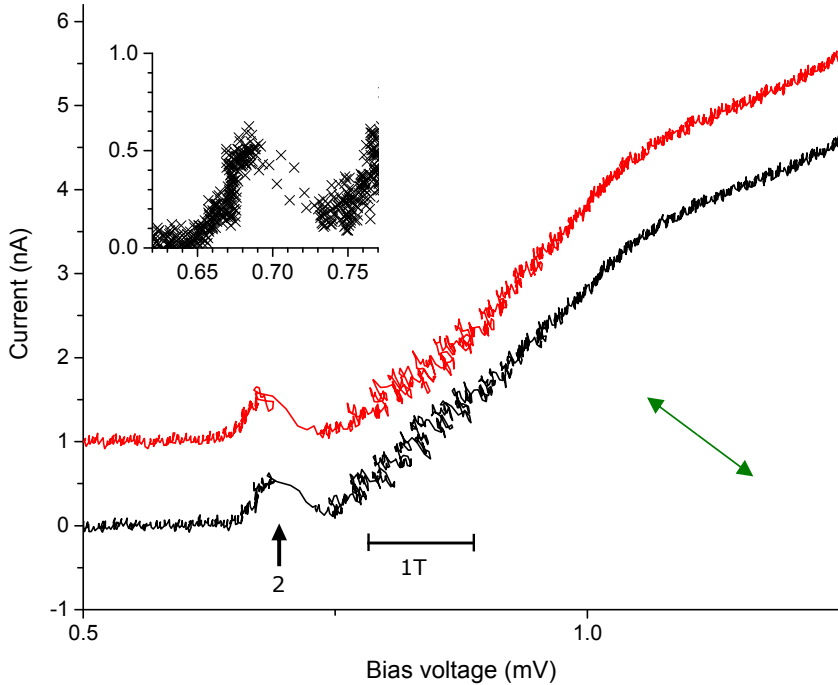


Figure 5.16: Raw data of the IV characteristics obtained for $V_G = -1.75$ mV (black) and $V_G = -1.65$ mV (red) (c.f. vertical lines in Fig. 5.15). For these gate voltages we observe the critical JQP (2) and the quasiparticle onset over the tunnel barrier (1T). Because of the high coupling through the break junction the JQP contributes a current that overcomes the critical current of the break junction. Thus, the current and the voltage change discontinuously which is illustrated in more detail in the inset (upper left). The jump contains only few data points. The inverse impedance of the bias ($Z_{\text{bias}} = 100$ k Ω) defines the direction of the jump in the plot and is represented by the green arrow. The quasiparticle onset over the tunnel barrier (1T) shows enhanced noise in the current and the voltage signals. Outside the onset mainly the current signal shows noise. The additional noise follows the inverse impedance as well.

Reprint from [Lor18].

the system is in a stable situation again (see Fig. 5.16). The direction and the slope of the jump is defined by the impedance of the bias line including the pre-resistors. The discontinuous behavior of $J - e$ processes is described in [Joy95]. We want to point out that we are not able to measure the critical current of the break junction independently. Additionally our measurement setup is not optimized to measure critical currents.

We assign the enhanced conductance at $eV_B = 4\Delta$ (η) to cotunneling effects, since it is not modulated by the gate voltage. For an SSET having the present resistances we did not expect to observe coherent tunneling effects. We assume that the mesoscopic character of the break junction leads to fewer conductance channels of higher transmission and therefore allows for cotunneling.

The small peak at the crossing of two Cooper pair lines (3) is the $3e$ cycle.

We should also take a closer look onto the quasiparticle onset. The positive slope of the quasiparticle onsets (1T) is broadened and looks fluffy (the differential conductance at the lines varies which is visible by the changes from red to yellow in the color-coded data). It describes transport over the tunnel barrier but its slope is defined by the capacitance of the

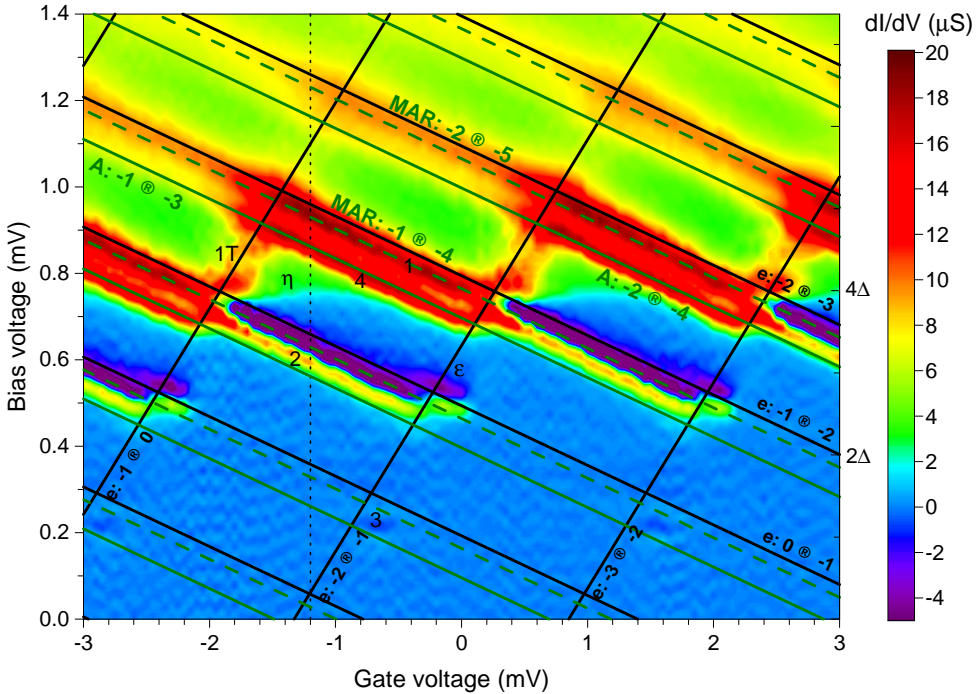


Figure 5.17: Presentation of the conductance as in Fig. 5.14 featuring the transport diagram using the Andreev ($m = 2$, solid dark green), the multiple Andreev ($m = 3$, dashed dark green) and the quasiparticle (black) lines. The diagram uses the same parameters as presented in Fig. 5.15, namely $\Delta = 192\mu\text{eV}$, $E_C = 116\mu\text{eV}$, $\delta C/C_\Sigma = -0.5484$, $C_G = 74.5\text{ aF}$ and $Q_0/e = 0.527$. We can identify the AQP cycle (4) as an onset starting at $eV_B = 2\Delta + 3E_C \approx 732\mu\text{eV}$ following the Andreev line. The MARQP is located close to the quasiparticle line. Thus, we cannot clearly identify whether a MARQP cycle contributes to the transport. The cycle labeled by ϵ remains unidentified.

break junction (c.f. Eq. (4.7)).

In Fig. 5.16 we display the raw data of the IV characteristics obtained for $V_G = -1.75\text{ mV}$ and $V_G = -1.65\text{ mV}$ (c.f. vertical lines in Fig. 5.15). Besides the critical JQP cycle at $V_B \approx 0.7\text{ mV}$ we observe the quasiparticle onset over the tunnel barrier for $0.75\text{ mV} \leq V_B \leq 0.9\text{ mV}$. This onset is indeed not step like but shows a slow rise of the current with increasing bias voltage. Additionally the current as well as the voltage signal show enhanced noise, while the noise outside the quasiparticle onset mainly affects the current signal. The additional noise is oriented according to the impedance, just as the jump of the JQP cycle. This is the reason for the “fluffiness” of the onset.

In [Lor18] two-level systems are discussed to be the reason for the behavior of the quasiparticle onset over the tunnel barrier. The author concludes that two-level systems may give rise to additional noise, but are not responsible for the broadening.

We argue that the broadening is related to the capacitance of the break junction and discuss this aspect in more detail in Section 5.4.3.

In Fig. 5.17 we use the parameters obtained earlier to draw the stability diagram for Andreev ($m = 2$, AR) and multiple Andreev reflection ($m = 3$, MAR) taking place over the break junction. This offers the possibility to identify further current cycles.

The AR line matches the onset close to the quasiparticle onset (4). This onset starts at $eV_B \approx$

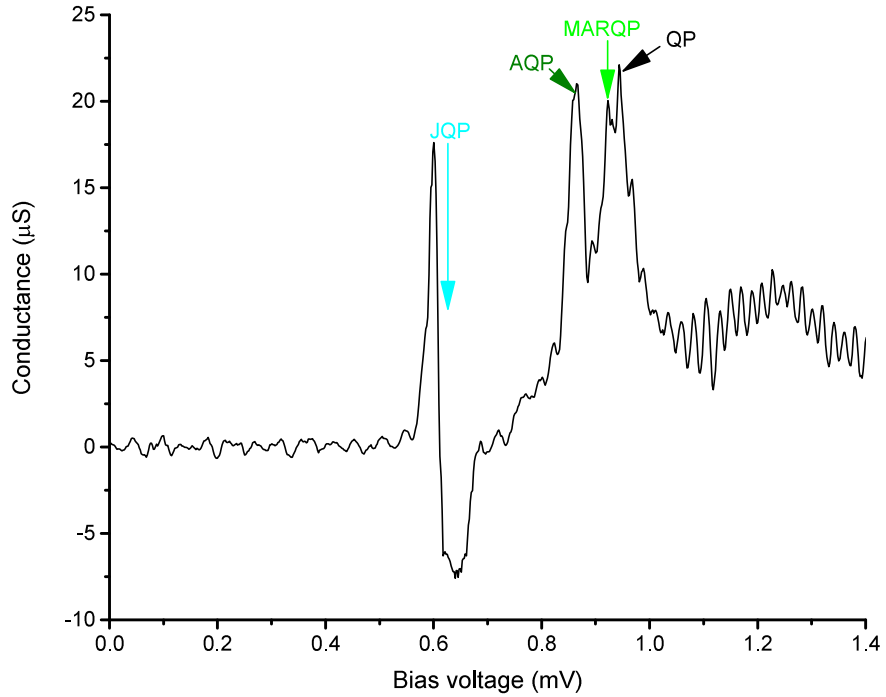


Figure 5.18: Conductance trace with respect to the bias voltage for $V_G = -1.2\text{ mV}$. The data presented here is filtered less in comparison to the representation in Fig. 5.17. We observe the signature of the JQP cycle at $V_B = 0\mu\text{eV}$. The conductance peak at $eV_B = 865\mu\text{eV}$ is caused by the AQP cycle. Next to the quasiparticle onset at $eV_B = 945\mu\text{eV}$ we observe a small peak at $eV_B = 925\mu\text{eV}$. This corresponds to the position of the MAR line in Fig. 5.17 and is caused by the MARQP cycle.

$732\mu\text{eV} \approx 2\Delta + 3E_C$ which is the starting point of the AQP cycle. Thus, we identify the onset as the AQP cycle.

The MAR line is of even higher interest since it is located very close to the quasiparticle line and is thus lying inside the aforementioned double onset. In the displayed representation (Fig. 5.17) it is hard to distinguish whether the multiple Andreev reflections contribute to the transport via the MARQP cycle or not. Therefore, we take a closer look in Fig. 5.18. Here, we present the differential conductance with respect to the bias voltage for $V_G = -1.2\text{ mV}$ (c.f. vertical line in Fig. 5.17). For this gate voltage the measurement covers the double onset across the break junction as well as the JQP cycle.

For the presented data we have used the statistical data binning to reduce the number of data point to 2000 points per measured IV characteristic instead of reducing to 100 points as done for the representation in Fig. 5.17. Then we calculate the numerical derivative using a polynomial function of 2nd order and 10 points. Calculating the derivative follows thereby the same procedure as for the data presented before.

Thus we average over less data points, which makes the obtained conductance trace noisier. On the other hand, it allows to detect a small peak at $eV_B \approx 925\mu\text{eV}$ in between the conductance peaks of the AQP onset (at $eV_B \approx 865\mu\text{eV}$) and the quasiparticle onset ($eV_B \approx 945\mu\text{eV}$). The position of the peak corresponds to the MAR-line at $V_G = -1.2\text{ mV}$. Thus, it is caused by the MARQP cycle.

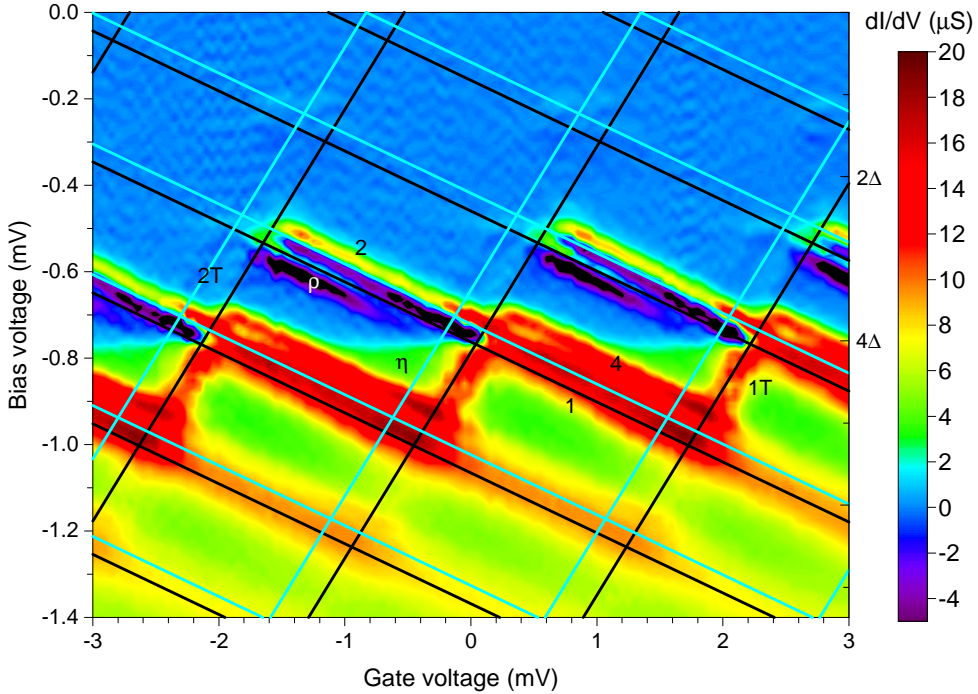


Figure 5.19: Superconducting conductance of the SET for $R_{TB} = 112\text{ k}\Omega$ and $R_{BJ} = 75\text{ k}\Omega$. We have added the transport diagram for Josephson and quasiparticle transport using the same parameters as for the positive bias polarity, namely $\Delta = 192\mu\text{eV}$, $E_C = 116\mu\text{eV}$, $\delta C/C_\Sigma = -0.5484$ and $C_G = 74.5\text{ aF}$ and a slightly changed offset charge $Q_0/e = 0.619$. Similar to Fig. 5.14 we observe the quasiparticle onset (1T, 1), the JQP cycle (2) and the AQP cycle (4). The MARQP cycle is hardly visible in this representation. Again, we observe cotunneling at $eV_B = 4\Delta$ (η). In contrast to the positive bias polarity, the cycle (ϵ) has vanished. Instead we observe an unidentified cycle (ρ) next to the JQP cycle.

Even though the Andreev and multiple Andreev lines enabled us to identify some of the mesoscopic current cycles, the origin of the cycle (ϵ) remains unclear.

5.3.3 Bias Asymmetries in the Mesoscopic SSET

Interestingly the behavior of the mesoscopic SSET depends on the bias polarity. In Fig. 5.19 we display the conductance of sample 1 for the same break junction configuration as in the section above but for negative bias voltages. We use the same parameters $\Delta = 192\mu\text{eV}$, $E_C = 116\mu\text{eV}$, $\delta C/C_\Sigma = 0.5484$ and $C_G = 74.5\text{ aF}$ as for the positive bias polarity to draw the stability diagram. We only varied Q_0/e slightly to obtain good visible matching. There is no argument for changing the offset charge Q_0/e related to the observed physical phenomena. We argue that the change is related to the bias circuit. A current depending offset of the common voltage of the symmetric bias voltage might act an additional gate voltage. Thus, we would observe a current dependent offset charge Q_0/e . Since we can verify whether this is the case in our measurement, we chose a varied offset charge as a convenient solution.

As expected we observe many similarities to the behavior for positive bias voltages. Again, the

quasiparticle onset across the tunnel barrier (1T) is broadened. The quasiparticle onset across the break junction (1) is accompanied by the AQP cycle (4) and the MARQP cycle (not visible in this representation). Cotunneling (η) leads to an enhanced conductance for $eV_B = 4\Delta$ and is not modulated by the gate voltage. The JQP cycle (2) is also visible and shows the same critical behavior as for the positive bias polarity. Additionally we observe a faint JQP cycle over the tunnel barrier (2T).

The unknown current cycle of the positive bias polarity (ϵ) has vanished. Instead we observe a new cycle (ρ) that seems to follow the same unknown line as (ϵ). Thus, we conclude that both cycles are of same nature. Both unknown processes occur as a peak in the current. Therefore, they must include Josephson transport. For (ϵ) it is also possible, that the cycle is located at the crossing of two lines.

5.4 The SSET beyond Orthodox Theory

Closing the break junction to resistances of $5\text{k}\Omega \leq R_{BJ} \leq 20\text{k}\Omega$ it forms an atomic contact. Additionally we enter the regime where the requirements of the Orthodox theory for low coupling $R_i \geq R_K$ are not fulfilled anymore. Thus the Orthodox theory is not sufficient for analyzing the data.

In the following section we present a measurement obtained on sample 1 for a break junction resistance of $R_{BJ} = 12\text{k}\Omega$. The resistance of the tunnel barrier stays constant, $R_{TB} = 112\text{k}\Omega$. In the normal conducting state the measurement looks similar to the one presented in Fig. 5.2b. The conductance inside the “diamonds” is not fully suppressed anymore. Additionally we do not observe a diamond structure. The region of suppressed conductance is rounded, so we are not able to obtain the stability diagram using the normal conducting data. Instead we observe an intensive Coulomb staircase defined by transport over the break junction (negative slope). We may use the periodicity along the gate axis to obtain the gate capacitance, which is $C_G \approx 75\text{aF}$. Using the method introduced in Section 5.1.1 we calculate the charging energy to be $E_C = 78\mu\text{eV}$. As discussed in Section 5.1.3 this is reduced in comparison to the charging energy observed for a fully opened break junction.

5.4.1 Simulation of the Mesoscopic SSET

We use the simulation method presented in Section 5.2.2 to clarify whether excited quasiparticles are the reason for the unknown current cycles. In Fig. 5.20a we present the simulated conductance using the parameters of the stability diagram, the resistances $R_{TB} = 112\text{k}\Omega$ and $R_{BJ} = 75\text{k}\Omega$, $T_{\text{sim}} = 0.5\text{K}$ and $k = 0$. Thus, we exclude the creation of excited quasiparticles by quasiparticle transport. We choose the Andreev conductance over the break junction to be $\tau_{\text{AR}} = 0.11$ and $\tau_{\text{MAR}} = 0.4$. As already explained, this parameters can be chosen freely to match the experimental data and do not correspond to the transmission probability $P \approx \tau^n$ as defined in Section 2.2.3. Andreev reflections over the tunnel barrier are not allowed.

The simulated conductance nicely reproduces the quasiparticle onset over the break junction

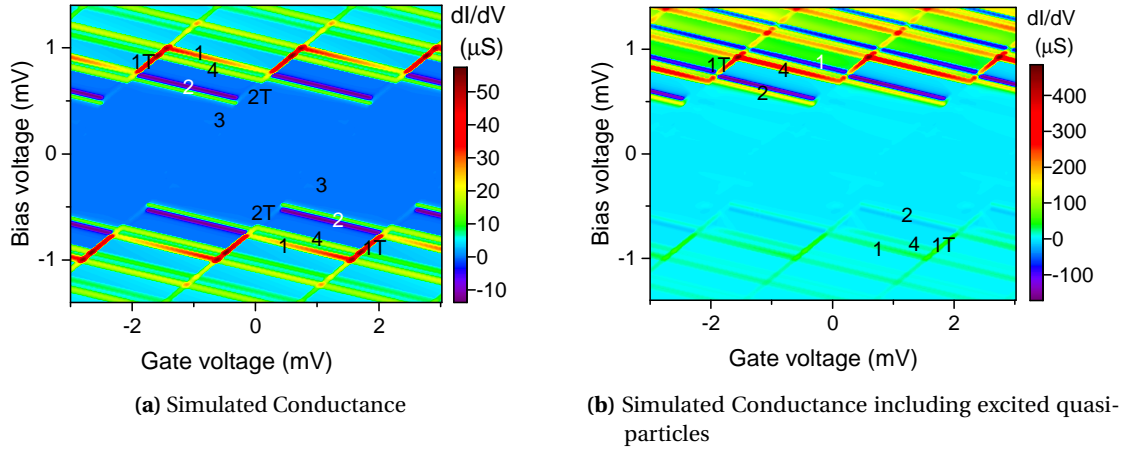


Figure 5.20: Simulation of the mesoscopic SET using the parameters of the stability diagram presented in Fig. 5.15. We use $T_{\text{sim}} = 0.5 \text{ K}$

(a) Simulation of the Orthodox theory including Andreev ($\tau_{\text{AR}} = 0.11$) and multiple Andreev reflections ($\tau_{\text{MAR}} = 0.04$) over the break junction. Andreev reflections over the tunnel barrier are excluded. The simulated conductance reproduces all identified current cycles. We observe the quasiparticle onset (1,1T), the JQP cycle (2,2T), the $3e$ cycle (3) and the AQP cycle (4). The MARQP cycle is overlaid by the quasiparticle tunneling. Neither does the simulation cover the observed cotunneling, nor the unidentified current cycles.

(b) Simulated conductance of the mesoscopic SSET including Andreev reflections as in (a) and excited quasiparticles ($k = 50$). We still only observe the already identified current cycles. The modified simulation does not yield any information about the unknown cycles.

(1). The onset over the tunnel barrier (1T) is rather sharp in the simulation and does not show the broadening observed in the experimental data. We observe the JQP cycle (2) as well as the AQP cycle (4). The MARQP is hardly visible as in the experimental data. If we set the transmission of the multiple Andreev reflection to zero, the quasiparticle onset becomes less prominent. Thus, we conclude that the MARQP contributes to the quasiparticle onset. The simulation shows contributions of Josephson transport over the tunnel barrier. We observe a JQP cycle (2T) and the $3e$ cycle (3). Since we have not included any cotunneling into our simulation, we do not observe the enhanced conductance as in the experiment (η). Additionally, none of the unidentified processes is present in the simulation.

In Fig. 5.20b we show the simulated conductance using the same parameter as in Fig. 5.20a and allowing for the creation of excited quasiparticles by setting $k = 50$. Most prominent is the bias asymmetry of the conductance of all current cycles. For negative bias voltages the pattern is only faint, whereas for positive bias voltages we observe rather high changes of the conductance as can be seen in the color coded data presented in Fig. 5.20b. For positive bias the complete spectrum of colors is observed indicating large changes of the conductance (approximatly $600 \mu\text{S}$), whereas the conductance for negative bias varies only by approximately $200 \mu\text{S}$. The reason for this asymmetry is the same as for the asymmetry described in Section 5.2.2, but applies to the Andreev reflection. If the Andreev reflection discharges the island two (three) quasiparticles need to charge the island to complete the AQP (MARQP) cycle respectively. Thus, several excited quasiparticles are created, giving rise to

additional current. If the Andreev reflection charges the island, the quasiparticles required to complete the cycle are transported off the island. Therefore, no additional current is observed. Since we only allow Andreev reflections over the break junction this creates asymmetric current contributions. Additionally the Andreev line marks a threshold. Thus, the enhanced AQP cycle for the positive bias polarity adds to the quasiparticle onset, creating a larger current for $eV_B \geq 4\Delta$ in comparison to Fig. 5.20a. The same mechanism applies to the enhanced JQP cycle for positive bias voltages.

Besides the asymmetry, we only observe already known current cycles (see description above). We conclude that the creation of excited quasiparticles on the island by quasiparticle tunneling is not the origin of the unknown current cycles.

This is also supported by the arguments presented in [Lor18]. There it is discussed which transport processes might contribute to the unknown current cycles. The author argues, that the asymmetry must be related to the multiple Andreev reflections. To support this argument he presents a measurement obtained on another sample, having a rather transparent tunnel barrier. The resistance was $R_{TB} = 30\text{k}\Omega$ and the measurement with an fully opened break junction $R_{TB} = 1.5\text{M}\Omega$ showed contributions of multiple Andreev reflections through the tunnel barrier. Again a bias asymmetry of the current cycles was observed even though they did not observe the same unknown current cycles as described in this section. The author asserts that bias asymmetric current cycles not covered by the Orthodox theory only occur, if multiple Andreev reflections are contributing to the transport. Thus he concludes a relation between the non-identified current cycles and multiple Andreev reflections.

5.4.2 The SSET in the Strong Coupling Regime

In Fig. 5.21 we display the conductance obtained in the superconducting case. Again the transport over the break junction following the negative slope dominates the observed pattern. Especially at higher bias values where quasiparticle tunneling dominates the transport, the Coulomb staircase is visible. We do not observe a diamond shaped quasiparticle onset, even though we can identify the quasiparticle lines following the negative slope (1). The weak onset at $eV_B = 4\Delta$ (1T) might be the quasiparticle onset over the tunnel barrier. Since all signatures of current cycle following the lines of positive slope are washed out or are even invisible, we cannot identify any of the lines of positive slope. All observed current cycles follow the lines of negative slope, which describes the transport over the break junction.

We observe a peak-like feature at $500\mu\text{eV} \lesssim eV_B \lesssim 750\mu\text{eV}$, that shows a discontinuous behavior. The jump of this cycle covers a rather broad area of the bias voltage. We identify this cycle as the JQP cycle. Already for $R_{BJ} = 75\text{k}\Omega$ the JQP cycle showed a discontinuous behavior.

For $650\mu\text{eV} \lesssim eV_B \lesssim 800\mu\text{eV}$ the experimental data shows a broadened onset (4). Since we expect Andreev reflections to contribute to the current for those break junction resistances, we assign this onset the AQP cycle.

The weak onset around $eV_B \approx 2\Delta$ does not clearly follow the Coulomb pattern. It can neither be assigned to the negative slope defined by the JQP cycle nor to a clearly distinguishably positive slope. Nonetheless it is modulated by the gate voltage and thus must be related to

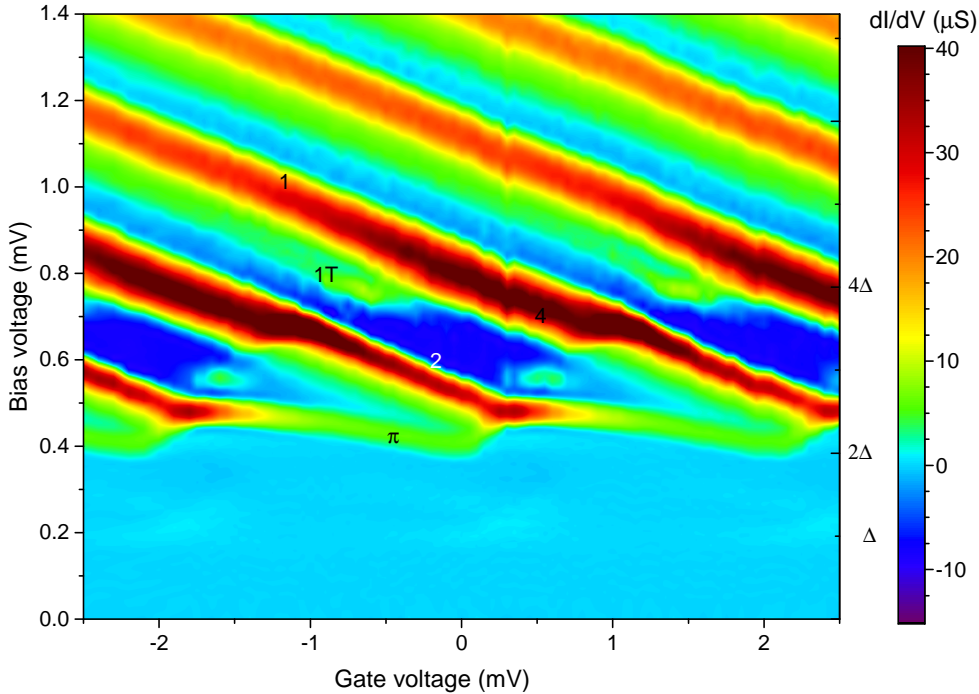


Figure 5.21: Superconducting conductance of the SET for $R_{BJ} = 12\text{ k}\Omega$ and $R_{TB} = 112\text{ k}\Omega$ with respect to bias and gate voltage. The pattern looks very different from the measurement presented before. We observe a Coulomb staircase for high bias voltages that is only defined by the transport over the break junction. The positive slope corresponding to the transport over the tunnel barrier is not visible. Thus, we do not observe a clearly diamond shaped quasiparticle onset at $eV_B \geq 4\Delta$, even though we can identify the onset along the negative slope (1). The small onset at $eV_B = 4\Delta$ (1T) might be the quasiparticle onset over the tunnel barrier. We identify the peak like feature (2) as the JQP cycle. The onset (4) following the negative slope and located next to the quasiparticle onset shows the characteristics of the AQP cycle.

Coulomb blockade effects.

Since we can not clearly identify both slopes, it is not possible to adjust the transport diagram as done before. Instead we will use the identified cycles all following the same slope and try to pinpoint the transport diagram this way.

Adjusting the Cooper pair, the Andreev and the quasiparticle line of negative slope we are able to pinpoint the complete stability diagram. We have already calculated C_G using the normal conducting data. We avoid using E_C for the stability diagram since we know that the exact value of the charging energy in the normal conducting state depends on the calculation method (c.f. Fig. 5.3). The superconducting gap $\Delta = 192\mu\text{eV}$ has been determined independently. Thus, the system is even overdetermined and allows to calculate all five parameters of the stability diagram, namely $\Delta = 192\mu\text{eV}$, $E_C = 58\mu\text{eV}$, $\delta C/C_\Sigma = 0.2574$, $C_G = 75\text{ aF}$ and $Q_0/e = 0.2103$. We show the complete stability diagram in Fig. 5.25a. Please note, that the obtained charging energy of the superconducting stability diagram is not in agreement with the value determined for the normal conducting case ($E_C = 80\mu\text{eV}$). It is not possible to match a transport diagram to the superconducting data using the normal conducting charging energy. We will discuss this aspect in more detail in Section 5.4.3.

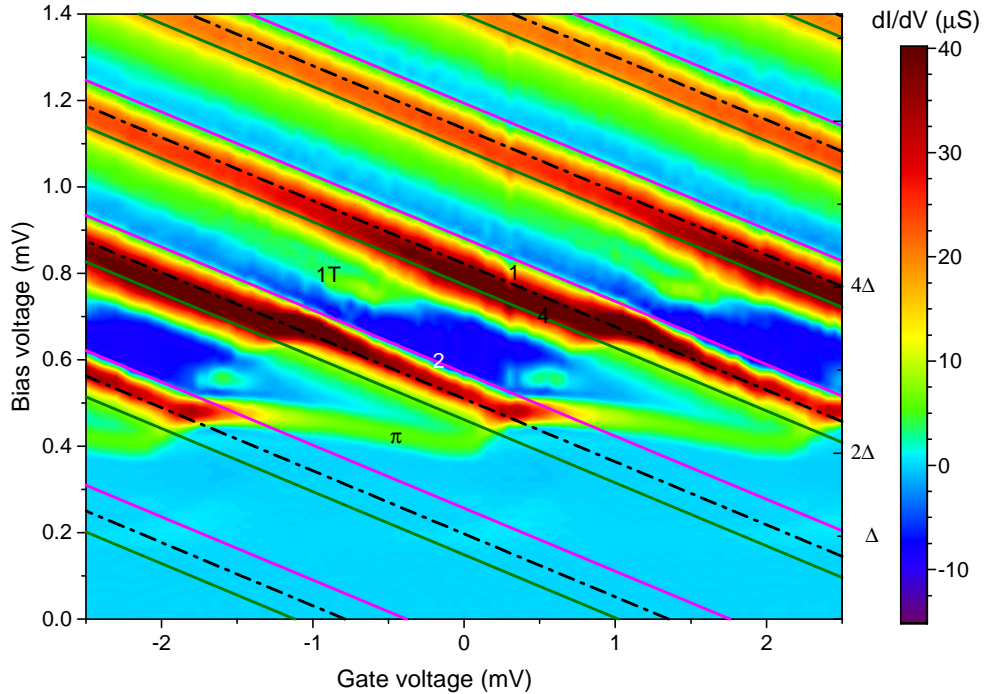


Figure 5.22: Conductance of the SSET for $R_{BJ} = 12\text{ k}\Omega$ and $R_{TB} = 112\text{ k}\Omega$. We have adjusted the Cooper par line (magenta) to fit the JQP cycle (2). The Andreev line (dark green) matches the AQP cycle (4). The quasiparticle line (dashed black) describes the Coulomb staircase for high bias voltages. Using those three lines, the gate capacitance calculated for the normal conducting state and the independently determined superconducting gap Δ we can pinpoint the complete stability diagram.

We use the calculated parameters to simulate the conductance, even though it is not allowed to apply the Orthodox theory anymore. Thus, we do not expect the simulation to reproduce all of the experimental observations. Additionally we already observed differences between simulation and experimental data for $R_{BJ} = 75\text{ k}\Omega$ (c.f. Section 5.4.1). There, the simulation did not reproduce the broadening of the quasiparticle onset over the tunnel barrier.

For the simulation we choose the Andreev conductance to be $\tau_{AR} = 0.1$ and $\tau_{MAR} = 0.04$. Since the MAR line is very close to the Andreev line we are not able to resolve the contribution of a possible MARQP cycle. The distance of the MAR and the Andreev line along the gate axis is approximately $16\mu\text{eV}$, whereas the distance of the Andreev and the quasiparticle line is much higher ($\approx 50\mu\text{eV}$). Since we do not observe two separated onsets for the AQP and the quasiparticle line, we are not expecting to resolve a possible MARQP cycle. Thus we have chosen the MAR conductance to be rather small.

In Fig. 5.23 we display the result of the simulation using $T_{\text{sim}} = 0.5\text{ K}$. As expected, the simulation shows notable differences in comparison with the experimental observations, but also shows some of the experimentally observed current cycles.

The simulated data show a distinct Coulomb Staircase dominated by transport over the break junction for higher bias voltages. We observe the quasiparticle onset over the break junction (1). The onset over the tunnel barrier (1T) is very distinct, even though we are not able to clearly see the onset in the experiment. Anyway, the simulation confirms that the weak onset at $eV_B \approx 4\Delta$ (c.f. Fig. 5.21) is indeed a signature of the quasiparticle onset over the tunnel

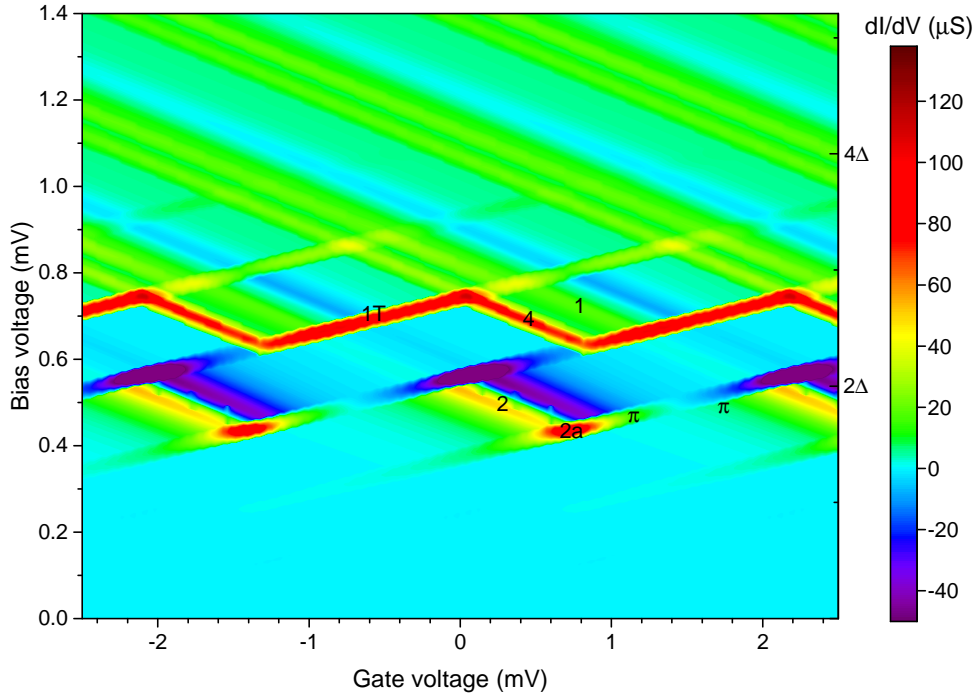


Figure 5.23: The Andreev conductance is set to $\tau_{\text{AR}} = 0.1$ and $\tau_{\text{MAR}} = 0.04$. The simulation reproduces the JQP cycle (2), the AQP cycle (4) and the quasiparticle onset over the break junction (1). The quasiparticle onset over the tunnel barrier (1T) is well discernible which is in contrast to our experimental observation. The simulated JQP cycle stops at $eV_B = 2\Delta + 3E_C$, whereas in the experiment we observe a elongation of the JQP cycle into the quasiparticle onset. At the starting point of the JQP (2a) the simulated data shows an increased conductance following the quasiparticle line over the break junction. We argue this feature to be the experimentally observed current cycle at $eV_B \approx 2\Delta$ being only slightly modulated by the gate voltage (π).

barrier.

The JQP cycle (2) is broadened in comparison to the simulation show for high break junction resistances. This is caused by the low break junction resistance [PFT00]. The JQP starts at $eV_B = 2\Delta + E_C \approx 442 \mu\text{eV}$ and ends at $eV_B = 2\Delta + 3E_C \approx 558 \mu\text{eV}$. In the experiment we observe a elongation of the JQP into the quasiparticle onset, which is not reproduced by the presented simulation. Furthermore, the simulated JQP cycle shows a local maximum in conductance at its starting point and a faint maximum in conductance following the quasiparticle lines of positive slope. This weak conductance onset in front of the JQP cycle following the quasiparticle line composes a ridge which we assign to the unknown current cycle (π) in the experimental data.

Starting at $eV_B = 2\Delta + 3E_C \approx 558 \mu\text{eV}$ we observe the AQP cycle (4) next to the quasiparticle onset. The AQP cycle is still observable for high bias voltages which is in contrast to the measurement. Here, the AQP fades away for $eV_B \gtrsim 750 \mu\text{eV}$.

Since the junction resistances are very asymmetric ($R_{\text{TB}} / R_{\text{BJ}} \approx 9.3$) we expect a elongation of the JQP when using higher temperatures in the simulation (c.f. Fig. 5.11b). Thus, we present the simulated conductance using $T_{\text{sim}} = 1 \text{ K}$ in Fig. 5.24a. Here, the JQP cycle (2) is prolonged into the quasiparticle onset (2*), since tunneling of excited quasiparticles over the break

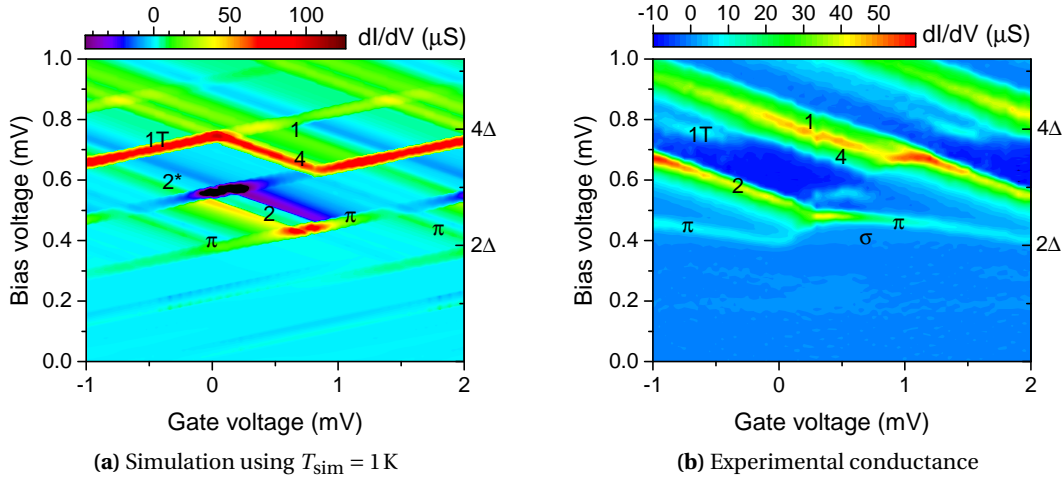


Figure 5.24: Effects of excited quasiparticles to the conductance of the SSET for $R_{\text{BJ}} = 12 \text{k}\Omega$ and $R_{\text{TB}} = 112 \text{k}\Omega$. (a) Simulated conductance using $T_{\text{sim}} = 1 \text{ K}$. The simulation shows the quasiparticle onset over the break junction (1) and the tunnel barrier (1T). The enhanced temperatures used in the simulation and the asymmetry of the resistances lead to a elongation of the JQP cycle (2*). Additionally, we observe an AQP cycle (4). The enhanced conductance at the starting point of the JQP cycle follows the quasiparticle line of positive slope and is much more pronounced as before. Thus, it forms a ridge (π) that we assign to the unknown current cycle observed in the experiment.

junction restores the initial charge state n of the JQP for $eV_B \geq 2\Delta + 3E_C$.

The excited quasiparticles also change the small onset at the starting point of the JQP cycle. For higher temperatures used in the simulation it is much more pronounced and now links two neighboring JQP cycles forming a gate modulated ridge. This strengthens our argument that this ridge is identical to the unknown current cycle (π) of the measurement. In the experiment this ridge does not completely follow the diamond structure but is more rounded. We assign this to the strong coupling through the break junction. Since the simulation includes no mechanism allowing for rounding but instead assumes perfectly sharp energy levels, we do not expect the experimental rounding to be present in the simulation. Additionally, the simulation does not account for the strong coupling but instead is designed to describe the SSET for weak coupling.

Nonetheless, the question about the origin of the excited quasiparticles remains. In this measurement we do not observe bias asymmetries of the JQP cycle, so the earlier mentioned slow relaxation of the excited quasiparticles (c.f. Fig. 5.12) is not the source and does not show up here.

Instead we argue that the break junction seems to be transparent for a fraction of quasiparticles. Thus they can be transported of or onto the island without following the Coulomb blockade. This assumption is supported by the observation of a weak conductance onset at $eV_B = 2\Delta$ (σ) presented in Fig. 5.24b. This onset is not modulated by the gate voltage and thus does not follow the Coulomb blockade. In our opinion the experimental data seems to be a superposition of the Coulomb pattern and the signatures of a single tunnel barrier.

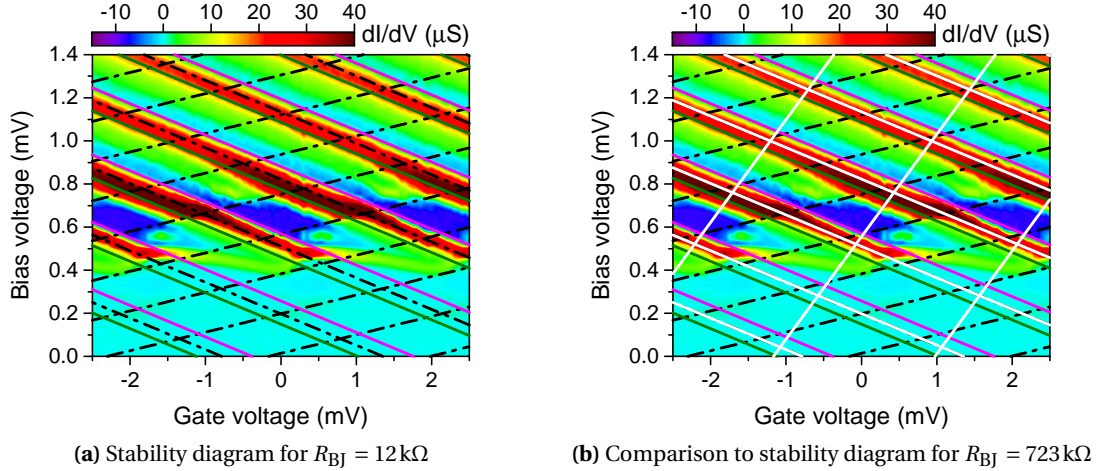


Figure 5.25: (a) We have matched the Cooper pair, the Andreev and the quasiparticle lines of negative slope to the identified current cycles. Thus, we are able to pinpoint the complete stability diagram, even though the positive slope is not identifiable in the measured conductance. (b) Comparison of the stability diagram obtained for two different configurations of the break junction of sample 1. The diagram for $R_{BJ} = 12 \text{ k}\Omega$ is painted in black, whereas the white lines represent the stability diagram for $R_{BJ} = 723 \text{ k}\Omega$. We have only drawn the quasiparticles lines. Interestingly, the lines representing transport over the break junction (negative slope) have the same slope. Only the positive slope has changed.

5.4.3 Renormalization of the Charging Energy in the Superconducting State

As already mentioned in the previous section, we observe a difference of the charging energies in the normal conducting and the superconducting state in sample 1 for $R_{BJ} = 12 \text{ k}\Omega$. To get an insight into the reason for this behavior, we will have a closer look into the stability diagram. Figure 5.25a shows the stability diagram calculated for sample 1 and $R_{BJ} = 12 \text{ k}\Omega$. We have used the procedure described in the previous section for pinpointing the diagram. Thus, we are able to determine the positive slope indirectly, even though it is not identifiable in the measurements.

In Fig. 5.25b we compare the stability diagram of Fig. 5.25a (drawn in black) to the stability diagram obtained for the same sample featuring a break junction resistance of $R_{BJ} = 723 \text{ k}\Omega$ (drawn in white). The measurement for the opened break junction has already been presented in Fig. 5.6. The negative slope of both diagrams is identical. Only the positive slope has changed.

The slopes only depend on the capacitances of the SET. The negative slope is defined by C_{TB} , C_G and C_{GND} . Since the slope does not change when closing the break junction, the capacitances do not change either. Thus, the change of the positive slope must be related to a change of the break junction's capacitance.

On the one hand this comes as no surprise, since we are geometrically changing the break junction when closing it. On the other hand we observe effects not explainable by only a change of the geometric capacitance. For an opened break junction the quasiparticle onset

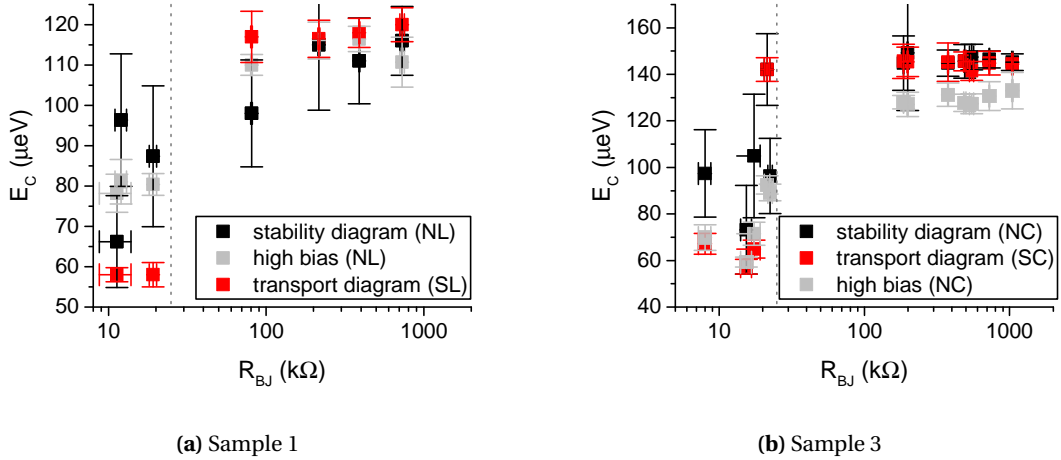


Figure 5.26: Comparison of the charging energies in the superconducting and the normal conducting state for sample 1 (a) and sample 3 (b). We display the charging energy calculated using the normal conducting stability diagram in black. The gray symbols represent the normal conducting charging energy obtained using the method described in Section 5.1.1. The superconducting charging energy (red) is determined by the transport diagram. We have added a vertical line at $R_{BJ} = 25 \text{ k}\Omega = R_K$ as guide to the eye. As soon as the break junction resistance is smaller, the superconducting charging energy is smaller than the normal conducting one.

of positive slope is clearly defined. When closing the junction to form a mesoscopic contact, the positive onset gets broadened and vanishes completely for an atomic contact. If the break junction would only change its capacitance, we would only observe a change of the slope, but not a broadening and a complete disappearance for low break junction resistances. This opens the question if the concept of a classically defined capacitance is still valid. We argue that the concept of quantum capacitance does not hold, since this would depend on the DOS of the system and thus change with the bias voltage. Our results do not show an energy dependence of the break junction capacitance. Instead it seems, that the increased coupling leads to a renormalization of the capacitance, similar to the renormalization observed for the charging energy. Here, we are clearly missing a theoretical concept able to explain the experimental observations.

The difference between the normal and the superconducting charging energies for small break junction resistances support this conclusion. In Fig. 5.26 we present the normal and the superconducting charging energies for various break junction configurations of sample 1 (Fig. 5.26a) and sample 3 (Fig. 5.26b). We display the normal conducting charging energy calculated in two ways. Black represents the charging energy extracted from the stability diagrams, whereas the charging energy represented in gray was calculated using the extension of the current at high bias voltages (c.f. Section 5.1.1). As already explained, the charging energy calculated by the latter method is always smaller in comparison to the value obtained from the stability diagram. The charging energy extracted from the superconducting transport diagram is displayed in red. We have added a dotted line at $R_{BJ} = R_K \approx 25 \text{ k}\Omega$ as guide to the eye.

For high break junction resistances $R_{BJ} > 25 \text{ k}\Omega$ the superconducting charging energy matches

to the normal conducting charging energy extracted from the stability diagram. As soon as the resistance drops below $25\text{ k}\Omega$, we observe differences between the charging energies, even though the energies of both states show the renormalization already reported in Section 5.1.3. For the normal conducting case we discussed the renormalization in terms of charge fluctuations. A renormalization in the superconducting state has neither been reported before, nor exist any theoretical predictions. Thus, we are not able to assign the renormalization in the superconducting state to a specific effect. Nonetheless, since the coupling of the island to the leads is different in the superconducting and the normal conducting state, we expect the charge fluctuations to influence the charging energy differently for both states. This interpretation is supported by the fact, that we only observe a change in the break junction capacitance, while the others stay constant. We only change the coupling through the break junction for various break junction configurations and leave all other couplings untouched.

Additionally we observe a difference of the superconducting and the normal conducting charging energy for $R_{\text{BJ}} \leq 25\text{ k}\Omega$. The superconducting charging energy is always lower than the normal conducting one. The only exception is observed for sample 3 for $R_{\text{BJ}} \approx 22\text{ k}\Omega$. For this specific measurement we argue, that the break junction rearranged after the normal conducting measurement. Since there is no possibility to calculate the resistance in the superconducting state, we are not able to proof whether this is the case or not.

Again the difference of the charging energies indicates, that the classical definition of a capacitance is not valid anymore for small enough break junction resistances, which also corresponds to the observed renormalization due to higher couplings. All of the reported observations indicate a correlation between the capacitance and the coupling of the break junction for high couplings. So far this relation is not covered theoretically.

Nonetheless, one should keep in mind, that the charging energy in the superconducting state has been calculated using Orthodox theory, even though the large coupling of the break junction breaks the requirements of the Orthodox theory. Here, an appropriate theoretical model is required to explain the experimental findings.

Chapter 6

Conclusion

In this thesis we present transport measurement of a single electron transistor (SET). A SET consists of a small metallic island that is connected to two leads via tunnel barriers. The small capacitance of the island leads to the observation of Coulomb blockade. The blockade is the result of the Coulomb repulsion of electrons and their quantized nature. Thus, a characteristic charging energy E_C is needed to add one additional electron to the island, otherwise the transport is blocked. Using a capacitively coupled gate electrode one can modulate the blockade. This leads to a transistor like behavior.

To observe the Coulomb blockade, the system needs to fulfill certain requirements. Thermal fluctuations or charge fluctuations due to high coupling of island and leads may destroy the Coulomb blockade. Thus, low temperatures $T < E_C / k_B$ and high junction resistances $R_i > R_K = h/e^2$ are essential. If these conditions are met, the charge states of the island are well-defined and the Orthodox theory describes the transport. The theory assumes sequential and non-coherent tunneling of single electrons through each junction of the SET.

In SETs made of superconducting materials the Coulomb blockade interacts with the superconductivity. Besides the charging energy, the superconducting gap Δ and the superconducting coupling defined by the Josephson energy E_J determine the behavior of the SET in the superconducting state. For $E_J \ll E_C < \Delta$ the coupling is low enough to justify the assumption of well-defined charge states and sequential tunneling. Additionally, the charging effects are not strong enough to break the superconductivity. Thus, all different kinds of superconducting transport possibilities may contribute to the electrical transport but still need to follow the Coulomb blockade. Especially the transport of Cooper pairs and multiple Andreev reflections are of interest. An extension of the Orthodox theory for the superconducting state allows to describe the transport through the SET qualitatively.

The SET presented in this thesis consists of a small island made of aluminum. One tunnel barrier is made of oxide, whereas the second one is realized by a mechanically controlled break junction. The resistance and thus the coupling of the break junction is tuned *in situ*. Therefore, it is possible to study the behavior of the Coulomb blockade for various couplings in the normal conducting as well as in the superconducting state. A break junction configuration featuring mesoscopic transport is especially interesting in the superconducting state since it allows for multiple Andreev reflections.

All measurements have been conducted at low temperatures in a dilution refrigerator. The measurement circuit consists of the sample being symmetrically surrounded by two reference

resistors of equal resistances. We use a symmetrical quasi-DC voltage as bias. The current through the SET is measured by the voltage drop over one of the reference resistors. This measurement scheme allows to resolve the superconducting properties as well as the Coulomb blockade in sufficient resolution for a broad range of resistances. This is necessary, since the break junction can be tuned from almost zero resistance to approximately $2\text{ M}\Omega$. Additionally, the IV curves are highly non linear featuring variable differential conductance.

The charging energy of the SET in the normal conducting state can be calculated using two methods.

By closing the break junction, the coupling of the island to one of the leads is increased. The observed renormalization is discussed in terms of charge fluctuations, which describes the behavior of low coupling but is not sufficient for strong couplings anymore. We assign this observation to the mesoscopic properties of the break junction. This work represents the first *in situ* study of the renormalization of the charging energy in metallic SETs.

The analysis of the measurements in the superconducting state is presented corresponding to the configuration of the break junction. For low couplings, the transport is described by the extension of the Orthodox theory to the superconducting state. For very low coupling through the break junction, the junction resistances are highly asymmetric. In this case, the transport shows signatures of non-equilibrium effects in the electronic system. These show up as new current cycles depending on the current direction. A new extension of the Orthodox theory is introduced, that describes the observed behavior qualitatively.

Adjusting the break junction to configuration allowing for mesoscopic transport, multiple Andreev reflections contribute to the transport through the SET. The Orthodox theory, extended to cover mesoscopic superconductivity, explains most of the observed current cycles. Nonetheless, one cycle dependent on the current direction cannot be explained. Arguments for a causal relationship of the observed asymmetry and the occurrence of multiple Andreev reflections are discussed.

If the break junction forms an atomic contact, the requirements for the Orthodox theory regarding the junction resistances are not met anymore. For this strong coupling regime, the system shows a superposition of Coulomb blockade effects and the characteristics of a single Josephson junction. A new evaluation method allows to pinpoint the superconducting transport diagram and thus to calculate the charging energy.

The reported renormalization of the charging energy is observed for the superconducting state as well. The charging energies of the super- and normal conducting states are equal for high break junction resistances. As soon as the break junction forms an atomic contact, the value obtained for the superconducting state deviates from the normal conducting state.

The sample design presented in this thesis is a model system suited to investigate the boundaries of the Orthodox theory. It allows to study the reaction of Orthodox theory to uncommon parameter sets like asymmetric resistances. The tuneability of the break junction enables us to go to the limits of Orthodox theory by increasing the coupling. The superconducting measurements are very useful to identify the contributions of mesoscopic transport. For atomic contacts formed in the break junction the superconducting measurements give a first insight on how the Coulomb blockade is altered by strong coupling.

Nevertheless, at present a theory describing the behavior in the strong coupling regime is

missing. A theory covering the strong coupling regime may also give insight into the observed renormalization of the charging energy in the superconducting and the normal conducting state. Additionally, a systematic study of the renormalization for metallic SETs in the normal conducting state will be helpful.

Bibliography

- [AA89] D. Averin and V. Y. Aleshkin. “Resonance Tunneling of Cooper Pairs in a System of Two Small Josephson Junctions”. *JETP Lett.* 50 (1989), 9–11.
- [AA90] V. Y. Aleshkini and D. V. Averin. “Resonant Tunneling of Cooper Pairs in a Double Josephson Junction System”. *Phys. B.* LT-19 165 (1990), 949–950.
- [AB63] V. Ambegaokar and A. Baratoff. “Tunneling Between Superconductors”. *Phys. Rev. Lett.* 10 (1963), 486–489.
- [AG98] I. L. Aleiner and L. I. Glazman. “Mesoscopic Charge Quantization”. *Phys. Rev. B* 57 (1998), 9608–9641.
- [AL91] D. V. Averin and K. K. Likharev. “Single Electronics: A Correlated Transfer of Single Electrons and Cooper Pairs in Systems of Small Tunnel Junctions”. *Mesoscopic Phenomena in Solids*. Ed. by B. Altshuler, P. Lee, and W. Richard Webb. 1st edition. Vol. 30. Modern Problems in Condensed Matter Sciences. Elsevier, 1991, p. 173.
- [ARV93] N. Agrait, J. G. Rodrigo, and S. Vieira. “Conductance Steps and Quantization in Atomic-Size Contacts”. *Phys. Rev. B* 47 (1993), 12345–12348.
- [Ave+97] D. V. Averin, A. N. Korotkov, A. J. Manninen, and J. P. Pekola. “Resonant Tunneling through a Macroscopic Charge State in a Superconducting Single Electron Transistor”. *Phys. Rev. Lett.* 78 (1997), 4821–4824.
- [AYvR03] N. Agrait, A. L. Yeyati, and J. M. van Ruitenbeek. “Quantum Properties of Atomic-Sized Conductors”. *Phys. Rep.* 377 (2003), 81–279.
- [BCS57] J. Bardeen, L. N. Cooper, and J. R. Schrieffer. “Theory of Superconductivity”. *Phys. Rev.* 108 (1957), 1175–1204.
- [Bri04] B. Briechle. “Entwicklung von Bruchkontaktelektroden mit separater ansteuerbarer Gatterelektrode”. Diplomarbeit. Universität Konstanz, 2004.
- [Cai+11a] N. Cai, G. Zhou, K. Müller, and D. E. Starr. “Effect of Oxygen Gas Pressure on the Kinetics of Alumina Film Growth during the Oxidation of Al(111) at Room Temperature”. *Phys. Rev. B* 84 (2011), 125445.
- [Cai+11b] N. Cai, G. Zhou, K. Müller, and D. E. Starr. “Tuning the Limiting Thickness of a Thin Oxide Layer on Al(111) with Oxygen Gas Pressure”. *Phys. Rev. Lett.* 107 (2011), 035502.
- [CB03] J. C. Cuevas and W. Belzig. “Full Counting Statistics of Multiple Andreev Reflections”. *Phys. Rev. Lett.* 91 (2003), 187001.

- [Cha+07] M. Chauvin, P. vom Stein, D. Esteve, C. Urbina, J. C. Cuevas, and A. L. Yeyati. “Crossover from Josephson to Multiple Andreev Reflection Currents in Atomic Contacts”. *Phys. Rev. Lett.* 99 (2007), 067008.
- [Cho+99] D. Chouvaev, L. S. Kuzmin, D. S. Golubev, and A. D. Zaikin. “Strong Tunneling and Coulomb Blockade in a Single-Electron Transistor”. *Phys. Rev. B* 59 (1999), 10599–10602.
- [Con16] T. Conzelmann. “Optimierung der Herstellung und elektrische Charakterisierung ultrakleiner Tunnelkontakte aus Aluminium und Aluminiumoxid”. Bachelor Thesis. Universität Konstanz, 2016.
- [Cou+08] N. A. Court, A. J. Ferguson, R. Lutchyn, and R. G. Clark. “Quantitative Study of Quasiparticle Traps Using the Single-Cooper-Pair Transistor”. *Phys. Rev. B* 77 (2008), 100501.
- [CW08] J. Clarke and F. K. Wilhelm. “Superconducting Quantum Bits”. *Nature* 453 (2008), 1031–1042.
- [EDM94] T. M. Eiles, M. H. Devoret, and J. M. Martinis. “Coulomb Blockade of Andreev Reflection in the NSN Single-Electron Transistor”. *Physica B: Condensed Matter* 194-196 (Part 1 1994), 1111–1112.
- [EMD93] T. M. Eiles, J. M. Martinis, and M. H. Devoret. “Even-Odd Asymmetry of a Superconductor Revealed by the Coulomb Blockade of Andreev Reflection”. *Phys. Rev. Lett.* 70 (1993), 1862–1865.
- [FD87] T. A. Fulton and G. J. Dolan. “Observation of Single-Electron Charging Effects in Small Tunnel Junctions”. *Phys. Rev. Lett.* 59 (1987), 109–112.
- [Fle93] K. Flensberg. “Capacitance and Conductance of Mesoscopic Systems Connected by Quantum Point Contacts”. *Phys. Rev. B* 48 (1993), 11156–11166.
- [FM95] A. Furusaki and K. A. Matveev. “Coulomb Blockade Oscillations of Conductance in the Regime of Strong Tunneling”. *Phys. Rev. Lett.* 75 (1995), 709–712.
- [FPT98] R. J. Fitzgerald, S. L. Pohlen, and M. Tinkham. “Observation of Andreev Reflection in All-Superconducting Single-Electron Transistors”. *Phys. Rev. B* 57 (1998), R11073–R11076.
- [FSZ95] G. Falci, G. Schön, and G. T. Zimanyi. “Unified Scaling Theory of the Electron Box for Arbitrary Tunneling Strength”. *Phys. Rev. Lett.* 74 (1995), 3257–3260.
- [Ful+89] T. A. Fulton, P. L. Gammel, D. J. Bishop, L. N. Dunkleberger, and G. J. Dolan. “Observation of Combined Josephson and Charging Effects in Small Tunnel Junction Circuits”. *Phys. Rev. Lett.* 63 (1989), 1307–1310.
- [GD92] H. Grabert and M. H. Devoret, eds. *Single Charge Tunneling*. Vol. 294. NATO ASI Series. Springer US, 1992.
- [GG00] G. Göppert and H. Grabert. “Single Electron Tunneling at Large Conductance: The Semiclassical Approach”. *Eur. Phys. J. B* 16 (2000), 687–704.
- [Göp00] G. Göppert. “Single Electron Tunneling at Large Conductance”. URN: urn:nbn:de:bsz:25-opus-1126. PhD Thesis. Albert Ludwigs Universität Freiburg i. Br., 2000.

- [Gra+12] G. J. Grabovskij, T. Peichl, J. Lisenfeld, G. Weiss, and A. V. Ustinov. “Strain Tuning of Individual Atomic Tunneling Systems Detected by a Superconducting Qubit”. *Science* 338 (2012), 232–234.
- [Gra+91] H. Grabert, G.-L. Ingold, M. H. Devoret, D. Estève, H. Pothier, and C. Urbina. “Single Electron Tunneling Rates in Multijunction Circuits”. *Z. Physik B - Condensed Matter* 84 (1991), 143–155.
- [Gre+11] T. Greibe, M. P. V. Stenberg, C. M. Wilson, T. Bauch, V. S. Shumeiko, and P. Delsing. “Are “Pinholes” the Cause of Excess Current in Superconducting Tunnel Junctions? A Study of Andreev Current in Highly Resistive Junctions”. *Phys. Rev. Lett.* 106 (2011), 097001.
- [Had+98] P. Hadley, E. Delvigne, E. H. Visscher, S. Lähteenmäki, and J. E. Mooij. “ $3e$ Tunneling Processes in a Superconducting Single-Electron Tunneling Transistor”. *Phys. Rev. B* 58 (1998), 15317–15320.
- [Hai18] P. Haiber. *Improving reliability of nanoscale Al-AlOx-Al contacts*. student project. Universität Konstanz, 2018.
- [Her95] J. M. Hergenrother. “Parity Effects and Charge Transport in the Single-Electron Transistor”. PhD Thesis. Harvard University, 1995.
- [HMP08] T. Holmqvist, M. Meschke, and J. P. Pekola. “Double Oxidation Scheme for Tunnel Junction Fabrication”. *Journal of Vacuum Science & Technology B: Microelectronics and Nanometer Structures Processing, Measurement, and Phenomena* 26 (2008), 28–31.
- [HTT94] J. M. Hergenrother, M. T. Tuominen, and M. Tinkham. “Charge Transport by Andreev Reflection through a Mesoscopic Superconducting Island”. *Phys. Rev. Lett.* 72 (1994), 1742–1745.
- [IN92] G.-L. Ingold and Y. V. Nazarov. “Charge Tunneling Rates in Ultrasmall Junctions”. *Single Charge Tunneling*. Ed. by H. Grabert and M. H. Devoret. NATO ASI Series. Springer, Boston, MA, 1992, p. 21.
- [JED98] P. Joyez, D. Esteve, and M. H. Devoret. “How Is the Coulomb Blockade Suppressed in High-Conductance Tunnel Junctions?” *Phys. Rev. Lett.* 80 (1998), 1956–1959.
- [Jez+16] S. Jezouin, Z. Iftikhar, A. Anthore, F. D. Parmentier, U. Gennser, et al. “Controlling Charge Quantization with Quantum Fluctuations”. *Nature* 536 (2016), 58–62.
- [Joy+97] P. Joyez, V. Bouchiat, D. Esteve, C. Urbina, and M. H. Devoret. “Strong Tunneling in the Single-Electron Transistor”. *Phys. Rev. Lett.* 79 (1997), 1349–1352.
- [Joy95] P. Joyez. “The Single Cooper Pair Transistor: A Macroscopic Quantum System”. PhD Thesis. Université Pierre et Marie Curie-Paris VI, 1995.
- [Kam11a] H. Kamerlingh Onnes. “Further Experiments with Liquid Helium. C. On the Change of Electric Resistance of Pure Metals at Very Low Temperatures, Etc. IV. The Resistance of Pure Mercury at Helium Temperatures.” *Comm. Phys. Lab. Univ. Leiden* 120b (1911).

- [Kam11b] H. Kamerlingh Onnes. “Further Experiments with Liquid Helium. D. On the Change of Electric Resistance of Pure Metals at Very Low Temperatures, Etc. V. The Disappearance of the Resistance of Mercury.” *Comm. Phys. Lab. Univ. Leiden* 122b (1911).
- [Kam11c] H. Kamerlingh Onnes. “Further Experiments with Liquid Helium. G. On the Electrical Resistance of Pure Metals, Etc. VI. On the Sudden Change in the Rate at Which the Resistance of Mercury Disappears.” *Comm. Phys. Lab. Univ. Leiden* 124c (1911).
- [KBT82] T. M. Klapwijk, G. E. Blonder, and M. Tinkham. “Explanation of Subharmonic Energy Gap Structure in Superconducting Contacts”. *Phys. B* 109 (1982), 1657–1664.
- [KMP12] H. S. Knowles, V. F. Maisi, and J. P. Pekola. “Probing Quasiparticle Excitations in a Hybrid Single Electron Transistor”. *Appl. Phys. Lett.* 100 (2012), 262601.
- [Kra+95] J. M. Krans, J. M. van Ruitenbeek, V. V. Fisun, I. K. Yanson, and L. J. de Jongh. “The Signature of Conductance Quantization in Metallic Point Contacts”. *Nature* 375 (1995), 767.
- [KSS97] J. König, H. Schoeller, and G. Schön. “Cotunneling at Resonance for the Single-Electron Transistor”. *Phys. Rev. Lett.* 78 (1997), 4482–4485.
- [Lan57] R. Landauer. “Spatial Variation of Currents and Fields Due to Localized Scatterers in Metallic Conduction”. *IBM J. Res. Dev.* 1 (1957), 223–231.
- [LH65] L. D. Landau and D. ter Haar. *Collected Papers of L.D. Landau*. OCLC: 30344484. Pergamon Press, 1965.
- [LHT98] J. G. Lu, J. M. Hergenrother, and M. Tinkham. “Effect of Island Length on the Coulomb Modulation in Single-Electron Transistors”. *Phys. Rev. B* 57 (1998), 4591–4598.
- [Lik87] K. Likharev. “Single-Electron Transistors: Electrostatic Analogs of the DC SQUIDS”. *IEEE Trans. Magn.* 23 (1987), 1142–1145.
- [Lim98] B. Limbach. “Untersuchung von Einzelelektronentransistoren auf der Basis von nanostrukturiertem Aluminium”. Diplomarbeit. Universität Karlsruhe, 1998.
- [Lis+15] J. Lisenfeld, G. J. Grabovskij, C. Müller, J. H. Cole, G. Weiss, and A. V. Ustinov. “Observation of Directly Interacting Coherent Two-Level Systems in an Amorphous Material”. *Nature Communications* 6 (2015), 6182.
- [Lor18] T. Lorenz. “Wechselspiel von Vielteilchen-Transport und Ladungseffekten in supraleitenden Einzelelektronentransistoren”. PhD Thesis. Universität Konstanz, 2018.
- [LSS18] T. Lorenz, S. Sprenger, and E. Scheer. “Coulomb Blockade and Multiple Andreev Reflection in a Superconducting Single-Electron Transistor”. *J Low Temp Phys* 191 (2018), 301–315.

- [McC68] D. E. McCumber. “Effect of Ac Impedance on Dc Voltage-Current Characteristics of Superconductor Weak-Link Junctions”. *Journal of Applied Physics* 39 (1968), 3113–3118.
- [ML97] K. A. Matveev and A. I. Larkin. “Parity Effect in Ground State Energies of Ultrasmall Superconducting Grains”. *Phys. Rev. Lett.* 78 (1997), 3749–3752.
- [Möl+98] S. Möller, H. Buhmann, S. F. Godijn, and L. W. Molenkamp. “Charging Energy of a Chaotic Quantum Dot”. *Phys. Rev. Lett.* 81 (1998), 5197–5200.
- [MvRdJ92] C. J. Muller, J. M. van Ruitenbeek, and L. J. de Jongh. “Experimental Observation of the Transition from Weak Link to Tunnel Junction”. *Phys. C* 191 (1992), 485–504.
- [NCT96] Y. Nakamura, C. D. Chen, and J. S. Tsai. “Quantitative Analysis of Josephson-Quasiparticle Current in Superconducting Single-Electron Transistors”. *Phys. Rev. B* 53 (1996), 8234–8237.
- [NST95] Y. Nakamura, T. Sakamoto, and J.-S. Tsai. “Study of Josephson-Quasiparticle Cycles in Superconducting Single-Electron Transistors”. *Jpn. J. Appl. Phys.* 34 (8S 1995), 4562.
- [Ole+94] L. Olesen, E. Laegsgaard, I. Stensgaard, F. Besenbacher, J. Schio/tz, P. Stoltze, K. W. Jacobsen, and J. K. No/rskov. “Quantized Conductance in an Atom-Sized Point Contact”. *Phys. Rev. Lett.* 72 (1994), 2251–2254.
- [Pas+93a] J. I. Pascual, J. Méndez, J. Gómez-Herrero, A. M. Baró, N. García, and V. T. Binh. “Quantum Contact in Gold Nanostructures by Scanning Tunneling Microscopy”. *Phys. Rev. Lett.* 71 (1993), 1852–1855.
- [Pas+93b] C. Pasquier, U. Meirav, F. I. B. Williams, D. C. Glattli, Y. Jin, and B. Etienne. “Quantum Limitation on Coulomb Blockade Observed in a 2D Electron System”. *Phys. Rev. Lett.* 70 (1993), 69–72.
- [Pek+08] J. P. Pekola, J. J. Virtainen, M. Möttönen, O.-P. Saira, M. Meschke, and D. V. Averin. “Hybrid Single-Electron Transistor as a Source of Quantized Electric Current”. *Nature Phys* 4 (2008), 120–124.
- [PFT00] S. L. Pohlen, R. J. Fitzgerald, and M. Tinkham. “The Josephson–Quasiparticle (JQP) Current Cycle in the Superconducting Single-Electron Transistor”. *Phys. B* 284 (2000), 1812–1813.
- [Pie15] W. W. Piegorsch. *Statistical Data Analytics: Foundations for Data Mining, Informatics, and Knowledge Discovery*. Wiley, 2015.
- [Pob07] F. Pobell. *Matter and Methods at Low Temperatures*. OCLC: 863876156. Springer Berlin Heidelberg, 2007.
- [Poh99] S. L. Pohlen. “The Superconducting Single-Electron Transistor”. PhD Thesis. Harvard University, 1999.

- [Pop+12] I. M. Pop, T. Fournier, T. Crozes, F. Lecocq, I. Matei, B. Pannetier, O. Buisson, and W. Guichard. "Fabrication of Stable and Reproducible Submicron Tunnel Junctions". *Journal of Vacuum Science & Technology B, Nanotechnology and Microelectronics: Materials, Processing, Measurement, and Phenomena* 30 (2012), 010607.
- [Pou+14] A. Pourkabirian, M. V. Gustafsson, G. Johansson, J. Clarke, and P. Delsing. "Nonequilibrium Probing of Two-Level Charge Fluctuators Using the Step Response of a Single-Electron Transistor". *Phys. Rev. Lett.* 113 (2014), 256801.
- [Raj+08] S. Rajauria, P. Gandit, T. Fournier, F. W. J. Hekking, B. Pannetier, and H. Courtois. "Andreev Current-Induced Dissipation in a Hybrid Superconducting Tunnel Junction". *Phys. Rev. Lett.* 100 (2008), 207002.
- [Sch+97] E. Scheer, P. Joyez, D. Esteve, C. Urbina, and M. H. Devoret. "Conduction Channel Transmissions of Atomic-Size Aluminum Contacts". *Phys. Rev. Lett.* 78 (1997), 3535–3538.
- [Sch+98a] E. Scheer, N. Agraït, J. C. Cuevas, A. L. Yeyati, B. Ludoph, A. Martín-Rodero, G. R. Bollinger, J. M. van Ruitenbeek, and C. Urbina. "The Signature of Chemical Valence in the Electrical Conduction through a Single-Atom Contact". *Nature* 394 (1998), 154.
- [Sch+98b] R. J. Schoelkopf, P. Wahlgren, A. A. Kozhevnikov, P. Delsing, and D. E. Prober. "The Radio-Frequency Single-Electron Transistor (RF-SET): A Fast and Ultrasensitive Electrometer". *Science* 280 (1998), 1238–1242.
- [Sch09] C. Schirm. "Einfluss hoher Ströme auf atomare Kontakte". Dissertation. Universität Konstanz, 2009.
- [Sch10a] O. Schecker. "Von Punktkontakten zu Nano-Elektro-Mechanischen Systemen - NEMS - Herstellung und Charakterisierung von Ein-Atom-Kontakten". OCLC: 724608630. Universität Konstanz, 2010.
- [Sch10b] E. Scheer. *Molecular Electronics: An Introduction to Theory and Experiment*. World Scientific, 2010. 724 pp.
- [Sch98] G. Schön. "Single-Electron Tunneling". *Quantum Transport and Dissipation*. Ed. by T. Dittrich. 1st edition. Wiley-VCH, 1998, p. 149.
- [Sen+18] J. Senkpiel, S. Dambach, M. Etzkorn, R. Drost, C. Padurariu, et al. "Single Channel Josephson Effect in a High Transmission Atomic Contact" (2018).
- [Ser+18] K. Serniak, M. Hays, G. de Lange, S. Diamond, S. Shankar, L. D. Burkhardt, L. Frunzio, M. Houzet, and M. H. Devoret. "Hot Nonequilibrium Quasiparticles in Transmon Qubits". *Phys. Rev. Lett.* 121 (2018), 157701.
- [Sie99] J. Siewert. "Two-Quasiparticle Tunneling in All-Superconducting Single-Electron Transistors". *Europhys. Lett.* 46 (1999), 768–774.
- [Spr16] S. Sprenger. "Herstellung und Charakterisierung von supraleitenden Einzelelektronentransistoren". Master Thesis. Universität Konstanz, 2016.
- [SS96] J. Siewert and G. Schön. "Charge Transport in Voltage-Biased Superconducting Single-Electron Transistors". *Phys. Rev. B* 54 (1996), 7421–7424.

- [Ste68] W. C. Stewart. “Current-voltage Characteristics of Josephson Junctions”. *Appl. Phys. Lett.* 12 (1968), 277–280.
- [SZ94] G. Schön and A. D. Zaikin. “Parity Effects on Electron Tunnelling Through Small Superconducting Islands”. *EPL* 26 (1994), 695–700.
- [Tha+17] M. Thalmann, H.-F Pernau, C. Strunk, E. Scheer, and T. Pietsch. “Comparison of Cryogenic Low-Pass Filters”. *Rev. Sci. Instrum.* 88 (2017), 114703.
- [THL95] M. Tinkham, J. M. Hergenrother, and J. G. Lu. “Temperature Dependence of Even-Odd Electron-Number Effects in the Single-Electron Transistor with a Superconducting Island”. *Phys. Rev. B* 51 (1995), 12649–12652.
- [Tin04] M. Tinkham. *Introduction to Superconductivity*. 2. ed. Dover Books on Physics. OCLC: 728146785. Dover Publ, 2004. 454 pp.
- [Tuo+92] M. T. Tuominen, J. M. Hergenrother, T. S. Tighe, and M. Tinkham. “Experimental Evidence for Parity-Based 2e Periodicity in a Superconducting Single-Electron Tunneling Transistor”. *Phys. Rev. Lett.* 69 (1992), 1997–2000.
- [Tuo+93] M. T. Tuominen, J. M. Hergenrother, T. S. Tighe, and M. Tinkham. “Single-Electron Tunneling Transistors Incorporating Cooper Pair Processes”. *IEEE Transactions on Applied Superconductivity* 3 (1993), 1972–1975.
- [vdBri+91] A. M. van den Brink, A. A. Odintsov, P. A. Bobbert, and G. Schön. “Coherent Cooper Pair Tunneling in Systems of Josephson Junctions: Effects of Quasiparticle Tunneling and of the Electromagnetic Environment”. *Z. Phys. B* 85 (1991), 459–467.
- [vdBSG91] A. M. van den Brink, G. Schön, and L. J. Geerligs. “Combined Single-Electron and Coherent-Cooper-Pair Tunneling in Voltage-Biased Josephson Junctions”. *Phys. Rev. Lett.* 67 (1991), 3030–3033.
- [Vio+96] D. Vion, M. Götz, P. Joyez, D. Esteve, and M. H. Devoret. “Thermal Activation above a Dissipation Barrier: Switching of a Small Josephson Junction”. *Physical review letters* 77 (1996), 3435–3438.
- [vWee+88] B. J. van Wees, H. van Houten, C. W. J. Beenakker, J. G. Williamson, L. P. Kouwenhoven, D. van der Marel, and C. T. Foxon. “Quantized Conductance of Point Contacts in a Two-Dimensional Electron Gas”. *Phys. Rev. Lett.* 60 (1988), 848–850.
- [Wal+02] C. Wallisser, B. Limbach, P. vom Stein, and R. Schäfer. “Single-Electron Transistors in the Regime of High Conductance”. *International Workshop on Superconducting Nano-Electronics Devices*. Ed. by J. Pekola, B. Ruggiero, and P. Silvestrini. Springer, Boston, MA, 2002, p. 123.
- [Wal02] C. Wallisser. “Einzelelektronentransistoren Im Regime Kleiner Widerstände”. Dissertation. Forschungszentrum Karlsruhe, 2002.
- [WG96] X. Wang and H. Grabert. “Coulomb Charging at Large Conduction”. *Phys. Rev. B* 53 (1996), 12621–12624.

BIBLIOGRAPHY

- [Yan+08] I. K. Yanson, O. I. Shklyarevskii, J. M. van Ruitenbeek, and S. Speller. “Aluminum Nanowires: Influence of Work Hardening on Conductance Histograms”. *Phys. Rev. B* 77 (2008), 033411.

Appendix

No.	Name	Sc Gap Δ	R_{TB}	E_C	C_G
1	TL5-II-8	192 μeV	112 $\text{k}\Omega$	129 μeV	75 aF
2	TL5-II-16	190 μeV	30 $\text{k}\Omega$	67 μeV	54 aF
3	TL10-II-8	175 μeV	195 $\text{k}\Omega$	113 μeV	31 aF

Table 1: List of all samples presented. We display typical parameters. The superconducting gap is determined for the unbroken sample. E_C refers the average of the charging energies obtained for a fully opened break junction $R_{\text{BJ}} \geq 400 \text{ k}\Omega$.